2018

IMPROVED METHODS FOR MEASURING CHARACTERISTIC FUNCTIONS OF UNDERWATER TRANSDUCERS

Bin Gao
University of Rhode Island, gaobinouc@gmail.com

IMPROVED METHODS FOR MEASURING CHARACTERISTIC FUNCTIONS OF UNDERWATER TRANSDUCERS

BY

BIN GAO

A DISSERTATION SUBMITTED IN PARTIAL FULFILLMENT OF THE REQUIREMENTS FOR THE DEGREE OF

DOCTOR OF PHILOSOPHY

IN

OCEAN ENGINEERING

UNIVERSITY OF RHODE ISLAND

2017

DOCTOR OF PHILOSOPHY DISSERTATION

OF

BIN GAO

APPROVED:

Dissertation Committee:

Major Professor Harold Vincent

Sau-Lon James Hu

Hongyan Yuan

Nasser H. Zawia

DEAN OF THE GRADUATE SCHOOL

UNIVERSITY OF RHODE ISLAND

2017

ABSTRACT

The overall objective of this dissertation is to effectively and efficiently obtain some important characteristic functions of acoustic transducers, such as electrical impedance function, transmitting voltage response (TVR) and beam pattern (BP). Oftentimes, one makes measurements on these functions through traditional ways, e.g., stepped harmonic analysis method and Fourier-based analysis method. To improve the accuracy and efficiency of computing these characteristics, new approaches by pole-residue operations are developed and verified in this dissertation.

In this new approach, the poles and residues associated with the input and output signals are extracted with the multi-signal Prony-SS method, which is an extension and improvement of the classical Prony's method. The system functions can be computed by the operations of those poles and residues from input and output signals. Compared with traditional methods, the new one not only turns out effective and computationally efficient but also overcomes the leakage and the frequency resolution problems, by getting a continuous function in the frequency domain without periodic assumption. In addition, many significant characteristics, such as modal frequencies and modal damping, can be precisely calculated from the system poles other than reading them from the plotting of system functions in traditional ways.

When a periodic loading excites the linear system, the calculation of transient response is discussed in manuscript 1. Compared with time-domain methods, frequency-domain methods are more computationally efficient when computing the responses of linear dynamic systems. However, frequency-domain methods can only compute the steady-state response instead of the total response. To the author's best knowledge, the transient response of a dynamic system to arbitrary periodic loading can not be solved analytically. In the first manuscript, a

closed-form solution for the transient responses of linear multi-degree-of-freedom (MDOF) systems to arbitrary periodic excitations is derived. By taking advantage of the fast Fourier transform (FFT) algorithm, a very efficient numerical method is developed to compute the transient and total responses of MDOF systems, suitable for both damped and undamped systems. In the newly developed method, the computational time required for obtaining the transient response is much less than that for the steady state response. Three numerical examples are provided in this manuscript to verify the correctness, and demonstrate the effectiveness as well, of the newly developed method.

Discussed in the second manuscript is the impedance function, which is very essential for a transducer. The impedance function contains many important characteristics, such as the resonant frequencies, anti-resonant frequencies, and maximum/minimum impedance values. In addition, the modal damping can also be calculated through impedance function. It is usually measured first under air loading and then under water loading. When the transducer is operated in water, some characteristics, such as resonant and anti-resonant frequencies, are changed because the acoustic medium becomes denser in water, and the added radiation mass in water is much greater than that in air. This new method by pole-residue operations is applied to estimate impedance functions of acoustic transducers. With this new method, the poles of the impedance function can be used to precisely compute some characteristics of the transducer, such as modal frequencies and modal damping. Four numerical examples show the procedures to calculate impedance functions of the transducer under air and water loadings through both finite element model and experiments. Together with their comparisons, the influence of water to the transducer, the radiating mass, has been quantified.

Transmitting voltage response (TVR) and beam pattern (BP) are two of the

most important measures of a transducer's ability to perform the functions of radiating sound. Traditionally, there are two kinds of methods for measuring TVR and BP, namely, single-frequency harmonic analysis method and Fourier-based analysis method. But, both methods have drawbacks. The former one is too time-consuming while the latter one suffers from the leakage and frequency resolution problems. Additionally, both of them are usually influenced by the reflecting waves from boundaries, such as water surface and acoustic tank walls. In manuscript 3, a new approach by pole-residue operations is developed to estimate TVR and BP, which overcomes the above drawbacks. Unlike the traditional methods, continuous characteristic functions in the frequency domain can be obtained by one-time measurement with the new method. Since very short signal is needed in this approach, the calculation of characteristic functions can be finished before the sound waves travel back from the boundaries. Two numerical examples are provided to show the procedures to compute TVR and BP of an underwater transducer. The effectiveness is verified by the harmonic analysis method. The accuracy and the efficiency are also demonstrated by the comparisons with traditional methods.

ACKNOWLEDGMENTS

Firstly, I would like to express my sincere gratitude to my advisor Dr. Harold Vincent and my committee member Dr. Sau-Lon James Hu for their continuous support of my Ph.D study and related research in the past years. Their patient guidance and immense knowledge have greatly helped me to write this dissertation and grow as a scientist. I could not have finished my Ph.D study and this dissertation without their support and encourages.

Besides, I would like to thank my committee member Dr. Hongyan Yuan for his useful advices on finite element modeling and insightful comments on my dissertation. My sincere thanks also goes to Dr. David Taggart, who kindly agrees to serve as the chair of my dissertation defense. I would also like to acknowledge Dr. Liang Su for his great help about model updating processes.

I thank all the help of my colleagues and my friends, Dr. Fushun Liu, Dr. Wenlong Yang, Dr. Zhongben Zhu and Dr. Haocai Huang, as well as the help and support from the ocean engineering department faculty and staff.

Last but not the least, I would like to thank my family for supporting me throughout my Ph.D study and my life.

DEDICATION

To my wife, Qianqian, for all her love and support.

PREFACE

This dissertation follows the University of Rhode Island Graduate School guidelines for the preparation of a dissertation in manuscript format. The material presented in this thesis is divided into six chapters.

- Chapter 1 provides an introduction to the studies within this dissertation, as well as a review of the relevant research in obtaining characteristic functions of a transducer.

- Chapter 2 is an introduction to methodology used throughout the dissertation. It begins with a brief overview of traditional methods to calculate the characteristic functions of a system. A recent pole-residue method is used to develop how to compute the TVR and BP of acoustic transducers. This approach is to calculate the system transfer functions based on pole-residue operations.

- Chapter 3 is a manuscript to derive a closed-form solution for the transient and total responses of SDOF/MDOF systems to arbitrary periodic excitations. It showed that the transient response could be obtained in a similar fashion as the steady-state response, but the roles of the system and excitation were reversed. Additionally, computational time needed for getting the transient response could be much less than that for the steady state response. This manuscript has been published by *Journal of Engineering Mechanics* in 2018.

- Chapter 4 shows a manuscript to discuss the influence of water to the characteristics of a transducer by comparing impedance functions when it's operated with air and water loadings. In this chapter, finite element models are developed both in air and in water to compute the reactive nodal charges

(output) due to the input voltage (input) applied on the transducer. In order for verification, experiments are designed to measure the voltage across the transducer (input) and electrical current in the circuit (output). The poles and residues are obtained by processing those input and output signals from FEM and experiments, which are used for the calculation of impedance functions and their comparisons. The resonant frequencies and damping ratios can be accurately obtained from the system poles instead of observing impedance function in the traditional way. The influence of water to the characteristics of underwater transducers is also quantified in this manuscript. This manuscript will be submitted to *IEEE Transactions on sonics and ultrasonics*.

- In Chapter 5, a manuscript presents how to calculate TVR and BP of an underwater transducer from finite element model by pole-residue operations. This new method can be applied to effectively compute the characteristic functions. Compared with traditional ways, in addition to the common leakage and frequency resolution problems, the proposed method also overcomes the contamination problem of reflected acoustic waves from boundaries by using very short signal. Furthermore, the efficiency of this method is demonstrated by giving a continuous function for all frequency components with one single input at a time when calculating TVR and beam pattern. This manuscript will be submitted to *The Journal of the Acoustical Society of America*.

- Conclusions and plans for future work are given in Chapter 6.

Appendix A is an introduction to the fundamentals of underwater transducers, such as piezoelectric material, acoustic medium, free flooded ring transducers and

Helmholtz frequency. Appendix B presents how to set up the finite element models in air and in water, and lists the details of key techniques of FE models. In appendix C, the author demonstrates the procedures to update material properties of the transducer used in this study.

TABLE OF CONTENTS

Page

Page

Page

Page

LIST OF FIGURES

Figure **Page**

Figure **Page**

Figure **Page**

LIST OF TABLES

Table **Page**

CHAPTER 1

Introduction

1.1 Problem statement

The study of electroacoustics began more than 200 years ago and the development expanded rapidly during the last decades. Currently, it has been grown to a large field with many significant applications, which involve mechanics, electricity, magnetism and acoustics.

A transducer is usually referred to a device that converts energy from one form to another. So, the electroacoustic transducer converts electrical energy to acoustical energy or vice versa, which is a multi-physics device and can be divided into three parts, mechanical as a moving body controlled by forces, electrical as a current controlled by voltage, and acoustical as an interaction between its moving surface and the ambient acoustic medium. Important characteristics of a transducer, such as resonant frequency, mechanical damping, electrical impedance function, electromechanical coupling coefficient, TVR and BP, are always the focuses for the design and practical applications of acoustic transducers (Sherman and Butler, 2007).

Electrical impedance function, TVR and BP will be studied in this dissertation. Electrical impedance function is a complex function in the frequency domain that describes the opposition of a current in a circuit to the applied voltage. As the complex ratio of the voltage to the current in an alternating current circuit, impedance possesses both magnitude and phase angle. The magnitude presents the resistance in the circuit and phase angle stands for the offset of the phase between the current and the applied voltage (Wikipedia Electrical Impedance, 2018).

The transmitting voltage response of a projector is defined as the pressure referenced to 1 meter and a pressure of $p_0 = 1$ μPa in underwater applications,

which is often represented on dB scale. It is one of the most important measurements for the acoustic performance of a transducer. Oftentimes TVR is measured in the direction of the maximum response axis at a radial distance in the far field (Sherman and Butler, 2007). However, the TVR in this study is extended to a function in the frequency domain in any direction other than only in the direction of maximum response axis, which can be interpreted as the transfer function from input voltage to output pressure referenced to 1 meter and 1 μPa.

Radiation usually refers to the emission or reception of wave front. In any case, a sketch drawn to show the radiation of a device is its radiation pattern, also called beam pattern. Beam pattern of a transducer is the variation of sound pressure level in the far field, which is a function of the direction away from the transducer. Since it is a relative quantity and only the power radiation pattern is concerned, the beam pattern is often scaled and plotted on logarithmic or dB scale (Wikipedia Radiation Pattern, 2018; Sherman and Butler, 2007).

Measurements of these functions are usually carried out at one single frequency, or over a range of frequencies of interest in the frequency domain. Generally, there are two types of traditional methods for measuring the above characteristic functions, i.e., stepped harmonic analysis method and Fourier-based analysis method. The stepped harmonic analysis is to repeatedly apply a harmonic input signal to get the corresponding steady state response of the given frequency, and is generally considered to be an accurate way to obtain frequency response function (FRF). The Fourier method computes the system function through the application of FFT of both input and output signals, and is considered to be an efficient way on estimating FRF. Both methods have drawbacks though. The stepped harmonic analysis method is time costly especially when very high time/frequency resolution is required, while the Fourier-based analysis method is always affected by the

periodic assumption and sampling rate for signals and consequently suffers from the leakage problem and frequency resolution issue.

In this study, a recently developed method in the Laplace domain, called pole-residue method, will be applied to estimate those characteristic functions. The application of the new method is to obtain the poles and residues of input and output signals processed by the Prony-SS method. Next, the system functions can be computed by manipulating those poles and residues, which will be shown in Chapter 2. Compared with traditional ones, the new method by pole-residue operations is more effective and more efficient to calculate the characteristic functions, and its accuracy in theory is higher than that of any time-domain approaches. Furthermore, it overcomes the leakage and the frequency resolution problems by getting a continuous function in the frequency domain without any assumption. In addition, many significant characteristics, such as modal frequencies and modal damping, can be precisely calculated from the system poles other than reading them from the plotting of system functions in traditional ways.

1.2 Organization of the text

This dissertation on characteristic functions has been written in the following five chapters.

Chapter 2 is an introduction to methodology used throughout the dissertation. It begins with a brief overview of traditional methods to calculate the characteristic functions of a system. A recent pole-residue method is used to develop how to compute the TVR and BP of acoustic transducers. This approach is to calculate the system transfer functions based on pole-residue operations.

Chapter 3 is a manuscript to derive a closed-form solution for the transient and total responses of SDOF/MDOF systems to arbitrary periodic excitations. It showed that the transient response could be obtained in a similar fashion as the

steady-state response, but the roles of the system and excitation were reversed. Additionally, computational time needed for getting the transient response could be much less than that for the steady state response.

Chapter 4 shows a manuscript to discuss the influence of water to the characteristics of a transducer by comparing impedance functions when it's operated with air and water loadings. In this chapter, finite element models are developed both in air and in water to compute the reactive nodal charges (output) due to the input voltage (input) applied on the transducer. In order for verification, experiments are designed to measure the voltage across the transducer (input) and electrical current in the circuit (output). The poles and residues are obtained by processing those input and output signals from FEM and experiments, which are used for the calculation of impedance functions and their comparisons. The resonant frequencies and damping ratios can be accurately obtained from the system poles instead of observing impedance function in the traditional way. The influence of water to the characteristics of underwater transducers is also quantified in this manuscript.

In Chapter 5, a manuscript presents how to calculate TVR and BP of an underwater transducer from finite element model by pole-residue operations. This new method can be applied to effectively compute the characteristic functions. Compared with traditional ways, in addition to the common leakage and frequency resolution problems, the proposed method also overcomes the contamination problem of reflected acoustic waves from boundaries by using very short signal. Furthermore, the efficiency of this method is demonstrated by giving a continuous function for all frequency components with one single input at a time when calculating TVR and beam pattern.

Finally, Chapter 6 concludes all the findings and contributions of this dissertation.

CHAPTER 2

Theoretical Development of System Functions

Characteristic functions of a transducer generally fall into the category of system functions. In engineering, a system function usually refers to a mathematical expression of the system characteristics, which demonstrates the relationship between the response (output) and the excitation (input) in some specific domain, oftentimes time-, frequency- or Laplace- domain. System functions provide the information that describes the behavior of a system, for example a transducer. Therefore, they are very essential for the studies of underwater transducers with respect to electrical and acoustical performance. The methods and the procedures to calculate system functions will be discussed in this chapter.

2.1 Introduction and literature review

System functions are commonly used in the analysis of systems which are linear time-invariant or having behavior that is close enough to linear. For convenience, this section will focus on the system functions of linear single-degree-of-freedom (SDOF) systems.

Traditional methods for obtaining system functions have been carried out in three distinct domains: *time*, *frequency* and *Laplace* domains, which are unit Impulse Response Function (IRF), Frequency Response Function (FRF) and Transfer Function (TF), respectively.

Throughout this dissertation, three types of specific notations are used to denote different variables in the three domains, i.e., lower-case letters for functions depending on time t, the same letters with a tilde for their Laplace transforms on s, and the same capital letters for their Fourier transforms on frequency ω. For example, $x(t)$, $\tilde{x}(s)$ and $X(\omega)$ represent a function in time domain, its Laplace

transform and its Fourier transform, respectively.

Following are the preliminaries and some discussion of above three methods.

2.1.1 IRF

The *unit impulse function*, $\delta(t)$, also referred to as the *Dirac delta function*, is defined as (Wikipedia Delta Function, 2018)

$$\delta(t) = \begin{cases} +\infty, & t = 0 \\ 0, & t \neq 0 \end{cases} \tag{2.1}$$

and is also constrained by the following feature

$$\int_{-\infty}^{+\infty} \delta(t) \mathrm{d}t = 1 \tag{2.2}$$

Consider a damped SDOF system subject to an excitation of unit impulse. Let the system initially be at rest. One can write the equation of motion as

$$m\ddot{u} + c\dot{u} + ku = \delta(t) \tag{2.3}$$

and initial conditions as

$$u(0) = 0, \qquad \dot{u}(0) = 0 \tag{2.4}$$

In physics, the unit impulse excitation only yields a sudden change of momentum between at and right after the time $t = 0$. Since momentum is the product of mass and velocity, together with the fact that mass is a constant value in this time-invariant system, the change of momentum can be expressed as change of velocity multiplied by the mass. In other words, the unit impulse external force is equivalent to giving the mass an initial velocity of $1/m$. Therefore, the dynamic problem becomes

$$m\ddot{u} + c\dot{u} + ku = 0 \tag{2.5}$$

$$u(0) = 0, \qquad \dot{u}(0) = 1/m \tag{2.6}$$

which is a free vibration with equivalent initial velocity $1/m$.

One can easily solve the unit *impulse response function*, denoted $h(t)$, as

$$h(t) = \frac{1}{m\omega_d} e^{-\xi\omega_n t} \sin(\omega_d t) \tag{2.7}$$

in which, the natural frequency

$$\omega_n = \sqrt{\frac{k}{m}} \tag{2.8}$$

the damped frequency

$$\omega_d = \sqrt{1-\xi^2}\omega_n \tag{2.9}$$

and the damping ratio

$$\xi = \frac{c}{2\sqrt{mk}} \tag{2.10}$$

2.1.2 FRF

Consider again the SDOF system in Eq. 2.3 for the complex frequency response function (Craig and Kurdila, 2006). Instead of δ-function, let the external force be $p(t) = p_0 \cos \Omega t$, where p_0 and Ω are the amplitude and the frequency of this periodic excitation, respectively. Therefore, the equation of motion for the damped SDOF system becomes

$$m\ddot{u}_R + c\dot{u}_R + ku_R = p_0 \cos \Omega t \tag{2.11}$$

Similarly, when the external force is changed to $p_0 \sin \Omega t$, the equation of motion will be

$$m\ddot{u}_I + c\dot{u}_I + ku_I = p_0 \sin \Omega t \tag{2.12}$$

Multiplying Eq. 2.12 by imaginary unit $i = \sqrt{-1}$ and adding it to Eq. 2.11, together with Euler's formula, one can have the complex equation of motion as

$$m\ddot{u} + c\dot{u} + ku = p_0 e^{i\Omega t} \tag{2.13}$$

in which u represents the complex response as $u = u_R + iu_I$. One can easily obtain the steady state solution of Eq. 2.13, denoted $u_s(t)$, as

$$u_s(t) = Ue^{i\Omega t} \tag{2.14}$$

in which the complex amplitude U has the expression of

$$U = \frac{p_0}{(k - m\Omega^2) + ic\Omega} \tag{2.15}$$

or

$$U = \frac{p_0/k}{(1 - r^2) + i(2\xi r)} \tag{2.16}$$

where $r = \Omega/\omega_n$ is the frequency ratio.

Therefore, the complex *frequency response function*, denoted $H(\Omega)$ or $H(r)$, can be obtained

$$H(\Omega) = H(r) \equiv \frac{U}{p_0} = \frac{1}{(k - m\Omega^2) + ic\Omega} = \frac{1/k}{(1 - r^2) + i(2\xi r)} \tag{2.17}$$

Eq. 2.17 can also be written in the form of amplitude and phase angle as

$$H(r) = Ae^{\alpha} \tag{2.18}$$

in which the amplitude of complex FRF is

$$A = |H(r)| = \frac{1/k}{\sqrt{(1 - r^2)^2 + (2\xi r)^2}} \tag{2.19}$$

and the phase angle is

$$\alpha = \tan^{-1}(-\frac{2\xi r}{1 - r^2}) \tag{2.20}$$

2.1.3 TF

Transfer function is used to calculate the system response by the Laplace transform (LT) method. The one-sided Laplace transform of an arbitrary function $f(t)$ in the time domain can be written as (Craig and Kurdila, 2006)

$$\tilde{f}(s) \equiv \mathcal{L}[f(t)] = \int_0^\infty e^{-st} f(t)\, dt \tag{2.21}$$

where $\tilde{f}(s)$ represents the signal in the Laplace domain and s is the Laplace variable.

Consider the SDOF system with given external force $p(t)$. Let the initial conditions be the displacement $u_0 = u(0)$ and the velocity $v_0 = \dot{u}(0)$. The equation of motion can be written as

$$m\ddot{u} + c\dot{u} + ku = p(t) \tag{2.22}$$

By definition of Laplace transform in Eq. 2.21, one can get the Laplace transform of $\dot{u}$ and $\ddot{u}$ as

$$\mathcal{L}[\dot{u}(t)] = s\int_0^\infty e^{-st}u(t)dt + e^{-st}u(t)\Big|_0^\infty = s\tilde{u}(s) - u_0 \tag{2.23}$$

and

$$\mathcal{L}[\ddot{u}(t)] = s^2\tilde{u}(s) - su_0 - v_0 \tag{2.24}$$

respectively.

Applying Laplace transform to both sides of Eq. 2.22, the equation of motion in the Laplace domain is obtained

$$(ms^2 + cs + k)\tilde{u}(s) = \tilde{p}(s) + mv_0 + (ms + c)u_0 \tag{2.25}$$

The last two terms of right-hand side in Eq. 2.25 are the initial condition problems and they have been theoretically solved in many textbooks. To focus on the transfer function, the system will be considered initially at rest. Therefore, Eq. 2.25 becomes

$$(ms^2 + cs + k)\tilde{u}(s) = \tilde{p}(s) \tag{2.26}$$

The response in Laplace domain can be written as

$$\tilde{u}(s) = \tilde{h}(s)\tilde{p}(s) \tag{2.27}$$

where $\tilde{h}(s)$ is the *transfer function* of the system

$$\tilde{h}(s) = \frac{1}{ms^2 + cs + k} = \frac{1}{m(s^2 + 2\xi\omega_n s + \omega_n^2)} \tag{2.28}$$

The transfer function $\tilde{h}(s)$ is a complex function of s and is displayed as a surface in Laplace domain. Consider the characteristic equation of the denominator in Eq. 2.28. For this damped system, the two roots s_1 and s_2 of the characteristic equation can be written as

$$s_{1,2} = -\xi\omega_n \pm i\omega_d \tag{2.29}$$

where s_1 and s_2 are complex conjugate, denoted μ and μ^* in the following presentation. The transfer function becomes

$$\tilde{h}(s) = \frac{1}{m(s-\mu)(s-\mu^*)} \tag{2.30}$$

where μ and μ^* are the so-called poles of the transfer function, which are related to the resonant frequencies and damping of the system. Through partial fraction expansion, Eq. 2.30 can be expressed as

$$\tilde{h}(s) = \frac{1}{m(s-\mu)(s-\mu^*)} = \frac{\beta}{(s-\mu)} + \frac{\beta^*}{(s-\mu^*)} \tag{2.31}$$

in which the complex conjugates β and β^* are called the residues of the transfer function, which are related to the amplitude of the response. The residues can be easily derived as

$$\beta = \frac{1}{i(2m\omega_d)} \tag{2.32}$$

2.1.4 Discussion

When solving dynamic problems, the three methods discussed in this section have their respective advantages and disadvantages/limitations, especially when systems become multi-degree-of-freedom (MDOF).

Time-domain method involves the convolution process and step-by-step numerical integration with the required time-step resolution. Although this method is

usually considered accurate, it is computationally expensive to carry out, especially when calculating a lengthy response with small time steps and a large number of DOF (Clough and Penzien, 2003; Craig and Kurdila, 2006; Hu et al., 2016).

To implement frequency-domain method, one firstly needs to decompose the input signal into some discrete harmonic components by Fourier transform. Multiplying the Fourier transform of input by the FRF of the system, one can calculate the response in the frequency domain. Finally, the time-domain response can be obtained by applying the inverse Fourier transform to the frequency-domain response. Due to the application of fast Fourier transform algorithm, frequency-domain method is usually more computationally efficient than time-domain method. However, the frequency-domain method can only deal with problems aiming at the steady-state response because it never includes any initial conditions. Furthermore, due to the periodic assumption, this method always suffers the leakage problem and frequency resolution issue (Clough and Penzien, 2003; Hu et al., 2016).

To solve a dynamic problem by the Laplace transform method, one needs to (1) obtain the transformed input signal in Laplace domain and the transfer function of the system, (2) multiply the Laplace-domain input by the transfer function, and (3) transform the results from Step 2 back to the time domain. The above procedures only consider the system with zero initial conditions because non-zero conditions can be easily solved separately. The Laplace transform method is pretty useful when the forward and inverse transforms can be found in the table of Laplace transforms. Therefore, traditional Laplace methods can only be applied under some particular conditions (Polking et al., 2006; Hu et al., 2016).

2.2 Pole-Residue Method

A recently developed pole-residue method used in this article falls into the category of Laplace-domain method. Compared with traditional methods that are

only limited to analytical forms, the new method are applicable to arbitrary input functions. The key development of the new method is to calculate the poles and residues of the response function. By the partial fraction forms of a function with the poles and residues, one can directly write the function in both time and Laplace domains. This section introduces how to obtain the poles and residues of all three components in a dynamic problem, i.e., input/excitation, system function, and output/response.

2.2.1 Poles and residues of an excitation

Consider a general complex function

$$f(t) = \alpha \exp(\lambda t) \tag{2.33}$$

in which α and λ are complex constant parameters.

By the definition of Laplace transform in Eq. 2.21, one can get its Laplace transform as

$$\tilde{f}(s) \equiv \mathcal{L}[f(t)] = \frac{\alpha}{s - \lambda} \tag{2.34}$$

Therefore, $\alpha \exp(\lambda t)$ and $\alpha/(s - \lambda)$ are a Laplace transform pair.

Mathematically, an arbitrary external force $p(t)$ can always be decomposed into a finite number of components (Hu et al., 2016)

$$p(t) = \sum_{\ell=1}^{L} \alpha_\ell \exp(\lambda_\ell t), \qquad 0 \leqslant t < T \tag{2.35}$$

By Eqs. 2.33 and 2.34, one can have the Laplace-domain excitation as

$$\tilde{p}(s) = \sum_{\ell=1}^{L} \frac{\alpha_\ell}{s - \lambda_\ell} \tag{2.36}$$

This expression is often called *partial fraction* form, or *pole-residue* form, in which λ_ℓ are the poles and α_ℓ are the corresponding residues.

Particularly, when substituting s by $i\omega$, Eq. 2.36 becomes

$$P(\omega) \equiv \tilde{p}(s = i\omega) = \sum_{\ell=1}^{L} \frac{\alpha_\ell}{i\omega - \lambda_\ell} \tag{2.37}$$

which can be interpreted as the Fourier transform of $p(t)$ with continuous frequency domain.

2.2.2 Poles and residues of a system

The equation of motion for an N-DOF system can be expressed by the following form (Craig and Kurdila, 2006; Hu et al., 2016)

$$\mathbf{M}\ddot{\mathbf{u}}(t) + \mathbf{C}\dot{\mathbf{u}}(t) + \mathbf{K}\mathbf{u}(t) = \mathbf{p}(t) \tag{2.38}$$

where $\mathbf{M}, \mathbf{C}, \mathbf{K}$ are $N \times N$ matrices of mass, damping and stiffness, respectively, $\mathbf{u}(t)$ is a $N \times 1$ vector of the displacement, and $\mathbf{p}(t)$ is a $N \times 1$ vector of the external force.

Consider the system initially at rest. Similar with the derivation of SDOF in section 2.1.3, one can get the Laplace transform of Eq. 2.38 as

$$(\mathbf{M}s^2 + \mathbf{C}s + \mathbf{K})\tilde{\mathbf{u}}(s) = \tilde{\mathbf{p}}(s) \tag{2.39}$$

The *transfer function matrix* is defined from input $\tilde{\mathbf{p}}(s)$ to output $\tilde{\mathbf{u}}(s)$, denoted by an $N \times N$ matrix $\tilde{\mathbf{h}}(s)$. Thus, one obtains

$$\tilde{\mathbf{u}}(s) = \tilde{\mathbf{h}}(s)\tilde{\mathbf{p}}(s) \tag{2.40}$$

Combining Eqs. 2.39 and 2.40, one can get

$$\tilde{\mathbf{h}}(s) = (\mathbf{M}s^2 + \mathbf{C}s + \mathbf{K})^{-1} \tag{2.41}$$

Each entry of $\tilde{\mathbf{h}}(s)$, denoted by $\tilde{h}_{jk}(s)$, is a transfer function, which relates the output at coordinate j to its input at coordinate k in this N-DOF system. Therefore, one can obtain all the poles and residues of this system once each transfer function $\tilde{h}_{jk}$ can be expressed in pole-residue form.

Now consider the state space model. Let the state vector be defined as a $2N$ vector

$$\mathbf{z}(t) = \left\{ \begin{array}{c} \mathbf{u}(t) \\ \dot{\mathbf{u}}(t) \end{array} \right\} \tag{2.42}$$

Thus, Eq. 2.38 can be rewritten in generalized state-space form

$$\mathbf{A}\dot{\mathbf{z}}(t) + \mathbf{B}\mathbf{z}(t) = \mathbf{q}(t) \tag{2.43}$$

where

$$\mathbf{A} = \begin{bmatrix} \mathbf{C} & \mathbf{M} \\ \mathbf{M} & \mathbf{0} \end{bmatrix}, \quad \mathbf{B} = \begin{bmatrix} \mathbf{K} & \mathbf{0} \\ \mathbf{0} & -\mathbf{M} \end{bmatrix} \quad \text{and} \quad \mathbf{q}(t) = \begin{Bmatrix} \mathbf{p}(t) \\ \mathbf{0} \end{Bmatrix}.$$

are the $2N \times 2N$ coefficients matrices and $2N \times 1$ state forcing vector. In physics, matrices $\mathbf{M}$, $\mathbf{C}$, and $\mathbf{K}$ are usually symmetric. Therefore, the coefficient matrices $\mathbf{A}$ and $\mathbf{B}$ in Eq. 2.43 are still symmetric.

The solution for this set of ordinary differential equations with constant coefficients has the form

$$\mathbf{z}(t) = \begin{Bmatrix} \mathbf{u}(t) \\ \dot{\mathbf{u}}(t) \end{Bmatrix} = \boldsymbol{\theta} e^{\mu t} = \begin{Bmatrix} \boldsymbol{\phi} \\ \mu\boldsymbol{\phi} \end{Bmatrix} e^{\mu t} \tag{2.44}$$

where μ is a scalar, $\boldsymbol{\theta}$ a $2N \times 1$ vector, and $\boldsymbol{\phi}$ an $N \times 1$ vector corresponding to the displacement vector $\mathbf{u}(t)$.

Combining Eqs. 2.43 and 2.44, one can obtain the generalized eigenvalue equation

$$[\mu\mathbf{A} + \mathbf{B}]\,\boldsymbol{\theta} = \mathbf{0} \tag{2.45}$$

By solving the characteristic equation

$$\det(\mu\mathbf{A} + \mathbf{B}) = 0 \tag{2.46}$$

one can get the solution of Eq. 2.45 with $2N$ eigenvalues μ_n and $2N$ corresponding eigenvectors $\boldsymbol{\theta}_n$, where $n = 1, 2, \cdots, 2N$. Note that the $2N$ eigenvalues μ_n must either be real or occur in complex conjugate pairs. Likewise, the eigenvectors $\boldsymbol{\theta}_n$ will correspondingly be real or complex conjugate pairs.

According to the orthogonality equations for complex modes, together with the symmetry of $\mathbf{A}$ and $\mathbf{B}$, one has

$$\boldsymbol{\theta}_r^t \mathbf{A} \boldsymbol{\theta}_s = 0, \quad \boldsymbol{\theta}_r^t \mathbf{B} \boldsymbol{\theta}_s = 0, \text{ for } \mu_r \neq \mu_s, \qquad r, s = 1, 2, \cdots, 2N \tag{2.47}$$

Defining the complex modal matrix

$$\mathbf{\Theta} = [\boldsymbol{\theta}_1 \ \boldsymbol{\theta}_2 \ \cdots \ \boldsymbol{\theta}_{2N}] \tag{2.48}$$

and the physical-modal coordinate transformation relationship

$$\mathbf{z} = \mathbf{\Theta}\mathbf{y} \tag{2.49}$$

one can decouple Eq. 2.43 into $2N$ modal first-order equations of motion

$$a_n\dot{y}_n + b_n y_n = q_n, \qquad n = 1, \cdots, 2N \tag{2.50}$$

where y_n is the 'state-space' solution of nth mode, $a_n = \boldsymbol{\theta}_n^t \mathbf{A}\boldsymbol{\theta}_n$, $b_n = \boldsymbol{\theta}_n^t \mathbf{B}\boldsymbol{\theta}_n$, and $q_n = \boldsymbol{\theta}_n^t \mathbf{q}$. Then, from Eq. 2.50, the transfer function of nth modal equation of motion can be easily derived as

$$\tilde{h}_n(s) = \frac{1}{a_n s + b_n} = \frac{1}{a_n(s - \mu_n)}, \qquad n = 1, \cdots, 2N \tag{2.51}$$

where poles $\mu_n = -b_n/a_n$. According to the principle of mode superposition, the transfer function $\tilde{h}_{jk}(s)$ can be written in the pole-residue form

$$\tilde{h}_{jk}(s) = \sum_{n=1}^{2N} \frac{\beta_{jk,n}}{s - \mu_n} \tag{2.52}$$

where residues

$$\beta_{jk,n} = \frac{\phi_{k,n}\phi_{j,n}}{a_n} \tag{2.53}$$

in which $\phi_{k,n}$ and $\phi_{j,n}$ are the k-th (input) and j-th (output) coordinates of $\boldsymbol{\phi}_n$.

discussion

The eigenvalue μ_n can be expressed in terms of the natural frequency ω_n and damping factor ξ_n:

$$\mu_n = -\xi_n\omega_n + i\omega_n\sqrt{1 - \xi_n^2} \tag{2.54}$$

In other words, the system natural frequencies and damping ratio can be calculated from the poles μ_n as

$$\omega_n = |\mu_n|, \quad \xi_n = \frac{-\mathrm{Re}(\mu_n)}{|\mu_n|} \tag{2.55}$$

In addition, once obtaining the transfer function $h_{jk}(s)$ in *pole-residue* form, one can write impulse response function $h_{jk}(t)$ immediately

$$h_{jk}(t) = \sum_{n=1}^{2N} \beta_{jk,n} e^{\mu_n t} \tag{2.56}$$

2.2.3 Poles and residues of the response

The total response at coordinate j due to all components of the excitation vector $\mathbf{p}(t)$ for the N-DOF system in Eq. 2.38 can be written as (Hu et al., 2016)

$$u_j(t) = \sum_{k=1}^{N} u_{jk}(t) \tag{2.57}$$

in which $u_{jk}(t)$ is the displacement response at coordinate j to the external force at k expressed by the convolution integral

$$u_{jk}(t) = \int_0^t h_{jk}(t-\tau)\, p_k(\tau)\, d\tau \tag{2.58}$$

Therefore, to obtain the total response, one just needs to calculate each $u_{jk}(t)$. Applying Laplace transform to Eq. 2.58, one can get the displacement response in the Laplace-domain

$$\tilde{u}_{jk}(s) = \tilde{h}_{jk}(s)\tilde{p}_k(s) \tag{2.59}$$

where the system is considered initially at rest. The key to obtaining the response $\tilde{u}_{jk}(s)$ is to compute its poles and residues.

From Eqs. 2.36 and 2.52, the external force $\tilde{p}_k(s)$ and the transfer function $\tilde{h}_{jk}(s)$ are written as

$$\tilde{p}_k(s) = \sum_{\ell=1}^{L} \frac{\alpha_\ell}{s - \lambda_\ell} \tag{2.60}$$

and

$$\tilde{h}_{jk}(s) = \sum_{n=1}^{2N} \frac{\beta_n}{s - \mu_n} \tag{2.61}$$

where the subscripts j and k of the residues of $\tilde{p}_k(s)$ and $\tilde{h}_{jk}(s)$ are omitted for the simplification of notations.

Substituting Eqs. 2.60 and 2.61 into Eq. 2.59, it yields

$$\tilde{u}_{jk}(s) = \left(\sum_{n=1}^{2N} \frac{\beta_n}{s - \mu_n} \right) \left(\sum_{\ell=1}^{L} \frac{\alpha_\ell}{s - \lambda_\ell} \right) \tag{2.62}$$

Eq. 2.62 can be rewritten in the pole-residue form

$$\tilde{u}_{jk}(s) = \sum_{m=1}^{L+2N} \frac{\gamma_m}{s - \nu_m} \tag{2.63}$$

Comparing Eq. 2.62 and Eq. 2.63, one can notice that the total $L + 2N$ response poles ν_m are originally from the L excitation poles and $2N$ system poles. Arrange the first L poles as the excitation poles, i.e., $\nu_m = \lambda_m$, $m = 1, \cdots, L$, and the last $2N$ poles as the system poles, i.e., $\nu_{m+L} = \mu_m$, $m = 1, \cdots, 2N$. For each response pole ν_m, the corresponding residue can be computed by (Hu et al., 2016)

$$\gamma_m = \lim_{s \to \nu_m} (s - \nu_m) \tilde{u}_{jk}(s) = \lim_{s \to \nu_m} (s - \nu_m) \tilde{p}_k(s) \tilde{h}_{jk}(s) \tag{2.64}$$

Thus, from Eq. 2.64, the residues corresponding to the first L response poles (at the excitation poles) are

$$\gamma_m = \lim_{s \to \nu_m} (s - \nu_m) \left(\sum_{l=1}^{L} \frac{\alpha_\ell}{s - \lambda_\ell} \right) \tilde{h}_{jk}(s) = \alpha_m \, \tilde{h}_{jk}(\lambda_m), \qquad m = 1, \cdots, L \tag{2.65}$$

and the residues corresponding to the last $2N$ response poles (at the system poles) are

$$\gamma_{m+L} = \lim_{s \to \nu_{m+L}} (s - \nu_{m+L}) \, \tilde{p}_k(s) \left(\sum_{n=1}^{2N} \frac{\beta_n}{s - \mu_n} \right) = \beta_m \, \tilde{p}_k(\mu_m), \qquad m = 1, \cdots, 2N \tag{2.66}$$

Eqs. 2.65 and 2.66 indicate that all residues of the response can be easily obtained from simple operations of the poles and residues of the excitation and system transfer function.

2.3 Pole-Residue Operations

Summarized in Table 2.1 are the poles, residues, and their operations of the three elements in a dynamic problem, i.e., *input*, *system*, and *output*. Based on any two, the other one can be obtained by the pole-residue operations. Since the *input* is always known, two scenarios commonly arise in many engineering fields, i.e., forward and inverse problems.

Table 2.1. Summary of operations for calculating the poles and residues of response $\tilde{u}_{jk}(s)$

Input $\tilde{p}_k(s)$		Transfer Function $\tilde{h}_{jk}(s)$		Output $\tilde{u}_{jk}(s)$	
poles (1)	residues (2)	poles (3)	residues (4)	poles (5)	residues (6)
λ_m $m = 1, \cdots, L$	α_m $m = 1, \cdots, L$	_	_	$\nu_m = \lambda_m$ $m = 1, \cdots, L$	$\gamma_m = \alpha_m \tilde{h}_{jk}(\lambda_m)$ $m = 1, \cdots, L$
_	_	μ_m $m = 1, \cdots, 2N$	β_m $m = 1, \cdots, 2N$	$\nu_{m+L} = \mu_m$ $m = 1, \cdots, 2N$	$\gamma_{m+L} = \beta_m \tilde{p}_k(\mu_m)$ $m = 1, \cdots, 2N$

When the input and the system are given, it is called a *forward problem*. To calculate the response, one first needs to prepare the poles and residues of input signal and the system, shown in columns $1 - 4$ of Table 2.1, by decomposing the input signal with Prony-SS method and performing modal analysis based on mass, stiffness and damping matrices of the system. The poles and residues can be calculated by the formulas shown in columns 5 and 6 of Table 2.1. Applying inverse Laplace transform by Eqs. 2.33 and 2.34, the response in time domain will be immediately obtained. Manuscript 1 is basically to solve a forward dynamic problem when the excitation is periodic, which improves the transient solution of

frequency-domain method.

While the input and output are known, it is called an *inverse problem*. To calculate the system characteristics, one needs to prepare the poles and residues of the excitation and the output, shown in columns 1, 2, 5 and 6 in Table 2.1, by simultaneously processing input and output signals using Prony-SS method (Hu et al., 2016; Hu and Gao, 2018). By applying this multi-signal method, Prony-SS method, to process the input and output signals simultaneously, it numerically guarantees that the poles of the input signals will always be included in those of the output signals, which are called *global poles*. The outcomes of the Prony-SS method consist of the global poles, input residues, and output residues. The system function can be calculated by the operations of these poles and residues from input and output. Manuscripts 2 and 3 are associated with the inverse problems on calculating the system functions of underwater transducers, i.e., electrical impedance function, transmitting voltage response function, and beam pattern.

Calculating system functions by pole-residue operations

Shown in Table 2.2 are the decomposition outcomes of input and output signals by multi-signal Prony-SS method. One can distinguish the input poles and system poles by observing the columns 1 and 2 in Table 2.2. In column 2, the input residues can be divided two groups, nonzero ones α_ℓ and zero or negligibly small ones. In column 1, the global poles are correspondingly divided into two groups, ν_ℓ and ν_{n+L}. The input poles are the ones ν_ℓ in the group of nonzero input residues while the system poles μ_n are the remaining ones ν_{n+L} in the group of zero or negligibly small input residues (Cao et al., 2017), which can also be interpreted that the system poles are simply the output poles ν minus the input poles λ in Table 2.1. From Eq. 2.55, together with the system poles, one can accurately

calculate the modal frequencies and modal damping of the system, which will be frequently used in this dissertation.

Eq. 2.59 shows the relationship among input, system and output in the Laplace domain for a system initially at rest. Thus, one can simply calculate the transfer function by

$$\tilde{h}_{jk}(s) = \frac{\tilde{u}_{jk}(s)}{\tilde{p}_k(s)} \tag{2.67}$$

From Eqs. 2.60 and 2.63, one obtains

$$\tilde{p}_k(s) = \sum_{\ell=1}^{L} \frac{\alpha_\ell}{s - \nu_\ell} \tag{2.68}$$

$$\tilde{u}_{jk}(s) = \sum_{m=1}^{2N+L} \frac{\gamma_m}{s - \nu_m} = \sum_{\ell=1}^{L} \frac{\gamma_\ell}{s - \nu_\ell} + \sum_{n=1}^{2N} \frac{\gamma_{n+L}}{s - \nu_{n+L}} \tag{2.69}$$

Notice that $\tilde{p}_k(s)$ and $\tilde{u}_{jk}(s)$ can be expressed by the global poles ν, input residues α and output residues γ.

Combining Eqs. 2.67 to 2.69, it yields the transfer function

$$\tilde{h}_{jk}(s) = \frac{\sum_{m=1}^{2N+L} \frac{\gamma_m}{s-\nu_m}}{\sum_{\ell=1}^{L} \frac{\alpha_\ell}{s-\nu_\ell}} \tag{2.70}$$

By substituting s with $i\omega$, Eq. 2.70 becomes complex FRF

$$H_{jk}(\omega) \equiv \tilde{h}_{jk}(s = i\omega) = \frac{\sum_{m=1}^{2N+L} \frac{\gamma_m}{i\omega-\nu_m}}{\sum_{\ell=1}^{L} \frac{\alpha_\ell}{i\omega-\nu_\ell}} \tag{2.71}$$

Table 2.2. Summary of operations for calculating the system functions $\tilde{h}_{jk}(s)$

global poles	input residues	output residues	system poles	system residues
ν_ℓ $\ell = 1, \cdots, L$	α_ℓ $\ell = 1, \cdots, L$	γ_ℓ $\ell = 1, \cdots, L$	–	–
ν_{n+L} $n = 1, \cdots, 2N$	0	γ_{n+L} $n = 1, \cdots, 2N$	$\mu_n = \nu_{n+L}$ $n = 1, \cdots, 2N$	$\beta_n = \gamma_{n+L}/\tilde{p}_k(\mu_n)$ $n = 1, \cdots, 2N$

Furthermore, the transfer function $\tilde{h}_{jk}(s)$ can also be calculated through the system identification procedures. After obtaining the system poles $\mu_n = \nu_{L+n}$, the remaining work is to compute the residues β_n in Eq. 2.61. According to column 5 in Table 2.2, the system residue β_n is equal to the output residue γ_{n+L} (at the system pole μ_n) divided by the value of input function at system pole location $\tilde{p}_k(\mu_m)$ as

$$\beta_n = \frac{\gamma_{n+L}}{\sum_{\ell=1}^{L} \frac{\alpha_\ell}{\mu_n - \nu_\ell}} \tag{2.72}$$

With the system poles μ_n and the residues β_n, one can numerically compute the transfer function

$$\tilde{h}_{jk}(s) = \sum_{n=1}^{2N} \frac{\beta_n}{s - \mu_n} \tag{2.73}$$

and complex FRF

$$H_{jk}(\omega) \equiv \tilde{h}_{jk}(s = i\omega) = \sum_{n=1}^{2N} \frac{\beta_n}{i\omega - \mu_n} \tag{2.74}$$

discussion

Both Eq. 2.71 and 2.74 can be applied to calculate the system functions by the pole-residue operations of input and output signals. Eq. 2.71 is applicable for general problems while applying Eq. 2.74 requires that the global poles of input

and output signals can be easily differentiated as shown in column 1 and 2 of Table 2.2. If none of the input residues is negligibly small, one can't distinguish input poles and system poles. In that case, only the general method (Eq. 2.71) is applicable.

In manuscript 2 and 3, it frequently happens that none of the input residues is zero or negligibly small for FE models and experiments. One reason is that the decomposition of input signals can be influenced by the components of some strong system poles when applying multi-signal Prony-SS method. Details will be shown in the manuscripts. Therefore, the method by pole-residue operations in Eq. 2.71 will be applied to calculate the characteristic functions of the transducers, i.e., electrical impedance function, transmitting voltage response and beam pattern. Compared with traditional methods, a continuous function in the frequency domain is obtained without any assumption and it overcomes the leakage and frequency resolution problems.In addition, many significant characteristics, such as modal frequencies and modal damping, can be precisely calculated by the system poles other than reading them from the plotting of system functions in traditional ways.

Chapter 3

"Computing Transient Response of Dynamic Systems in the Frequency Domain"

by

Sau-Lon James Hu[1] and Bin Gao[2]

has been published in *Journal of Engineering Mechanics*

---

[1] Professor, Department of Ocean Engineering, University of Rhode Island, Narragansett, RI 02882. E-mail:jameshu@uri.edu

[2] PhD Candidate, Department of Ocean Engineering, University of Rhode Island, Narragansett, RI 02882. E-mail:gaobinouc@gmail.com

CHAPTER 3

Manuscript 1: Computing Transient Response of Dynamic Systems in the Frequency Domain

3.1 Abstract

Frequency-domain methods are usually more efficient computationally than time-domain methods to compute the responses of linear dynamic systems. However, a common drawback of frequency-domain methods is that computed responses are merely the steady-state response, not the total response. It appears that no analytical solution has been derived for the transient response of a multiple-degree-of-freedom (MDOF) dynamic system to arbitrary periodic loading. An analytical contribution of this article is deriving a closed-form solution for the transient responses of linear MDOF systems to arbitrary periodic excitations. Together with the fast Fourier transform (FFT) algorithm, a very efficient numerical method is developed to compute the transient and total responses of MDOF systems, suitable for both damped and undamped systems. In the newly developed method, the computational time required for obtaining the transient response is much less than that for the steady state response. Three numerical examples are provided in this paper to verify the correctness, and demonstrate the effectiveness as well, of the newly developed method.

3.2 Introduction

Computing the dynamic response of a linear multiple-degree-of-freedom (MDOF) system to periodic loading, operated in the frequency domain, is considered in this paper. Analytically, the total dynamic response is the sum of two parts: (1) the steady-state response, which mathematically is the particular solution to the periodic input function, and (2) the transient response which is the homoge-

neous solution that satisfies the given initial conditions (Craig and Kurdila, 2006; Clough and Penzien, 2003; Kreyszig, 2011). The transient response has been so named because the damping effect would cause the free-vibration term to vanish eventually. For an undamped system, however, this term would not damp out but continue indefinitely. To the best knowledge of the authors, there is no analytical close-form solution available in the existing literature for computing the transient response of dynamic system to arbitrary periodic loading. The novelty of this paper is to analytically and numerically compute the transient response in the frequency domain of MDOF systems to arbitrary periodic loading.

In the calculation for the total response of a dynamic system, one often employs a time domain approach. Implementing a time domain approach is costly in computational time, especially evaluating a lengthy response with small time steps for systems with a large number of degrees-of-freedom. In contrast, conducting a frequency-domain method is computationally efficient when the fast Fourier transform (FFT) algorithm is employed in the procedure. However, a common drawback of frequency-domain methods is that the computed response is only the steady-state response.

All frequency-domain methods, in computing the dynamic response of a linear system, require the loading be resolved into its discrete harmonic components by Fourier transformation. When a discrete Fourier transform or Fourier series of a signal is invoked, the signal is intrinsically assumed to be periodic. For a single-degree-of-freedom (SDOF) system to periodic loading, traditional frequency-domain methods multiply the harmonic loading components by the frequency response function (FRF) of the system to obtain the corresponding harmonic response components; and finally the response of the system is obtained by implementing the inverse Fourier transform (Clough and Penzien, 2003;

Craig and Kurdila, 2006). Apparently, this obtained response is the steady-state response associated with the periodic loading. As no analytical method was available to compute the transient response, a numerical technique to compute the total response has been employed by padding the input signal with sufficient zeros so that the free vibration response during the intervals of zero excitation would damp out completely (Clough and Penzien, 2003). Even for a simple SDOF system, this technique does not work if the system is undamped or lightly damped.

A new frequency domain method is to be developed in this paper to compute not only the steady state response but also the transient response of MDOF linear systems to arbitrary periodic loading. It will be shown that the transient response can be obtained in a similar fashion as the steady-state response. In brief, the newly developed method includes the following five sequential steps while computing both the steady-state and transient response components: (1) conducting the Fourier analysis of the periodic excitation to obtain its Fourier coefficients; (2) obtaining the poles and residues associated with the system transfer functions, and then the corresponding frequency response functions; (3) following a classical way to calculate the steady-state response using the knowledge of (1) and (2); (4) computing the transient response using the knowledge of (1) and (2), which is to be newly derived in this article; and (5) combining (3) and (4) to get the total response.

Three numerical examples will be provided in this paper to verify the correctness of the newly developed method. For illustrating the detailed operations of the proposed method, the first numerical example considers a SDOF system to a square wave periodic loading. For demonstrating the effectiveness of the proposed method in practical engineering application, the second example computes the response of a lightly damped SDOF system to a recorded El Centro earthquake

loading. The purpose of the third example is to demonstrate the applicability of the developed method to a MDOF system.

3.3 Preliminaries

This section reviews the background material related to complex exponential functions, complex Fourier series and linear MDOF systems that is essential to this article; it also intends to acquaint the reader with the notation convention to be used. Throughout this paper, functions depending on time t are in lower cases; their Laplace transforms on s denoted by the same letters with a tilde, and their Fourier transforms on ω denoted by the same capital letters. For example, $\tilde{y}(s)$ and $Y(\omega)$ denote the Laplace transform and Fourier transform of $y(t)$, respectively.

3.3.1 Complex exponential functions

It is easy to show that $\alpha \exp(\lambda t)$ and $\frac{\alpha}{s-\lambda}$ form a Laplace transform pair (Kreyszig, 2011). In turn, for the complex exponent function

$$y(t) = \sum_{\ell=1}^{L} \alpha_\ell \, \exp(\lambda_\ell t) \tag{3.1}$$

one shows

$$\tilde{y}(s) = \sum_{\ell=1}^{L} \frac{\alpha_\ell}{s - \lambda_\ell} \tag{3.2}$$

Eq. 3.2 in the Laplace domain is often called a *partial fraction* form, or *pole-residue* form, with poles λ_ℓ and the corresponding residues α_ℓ. When the real part of the complex variable s is set equal to zero, that is, substitutes s by $i\omega$ in Eq. 3.2, it yields the corresponding Fourier transform function:

$$Y(\omega) \equiv \tilde{y}(s = i\omega) = \sum_{\ell=1}^{L} \frac{\alpha_\ell}{i\omega - \lambda_\ell} \tag{3.3}$$

which is essentially the frequency domain representation of $y(t)$.

3.3.2 Periodic excitation

Forces acting on structures are frequently periodic, or can be approximated closely by periodic forces. A periodic function with period T_1, that is $p(t+T_1) = p(t)$, can be decomposed into its harmonic components by means of a Fourier series. The complex Fourier series of $p(t)$ may be written as

$$p(t) = \sum_{m=-\infty}^{\infty} C_m \exp\left(i\Omega_m t\right) \tag{3.4}$$

where $\Omega_m = m\Omega_1$, $\Omega_1 = 2\pi/T_1$ is the fundamental frequency (in rad/s), and C_m is the mth complex Fourier coefficient of the periodic function:

$$C_m = \frac{1}{T_1}\int_0^{T_1} p(t)e^{-i\Omega_m t}dt \tag{3.5}$$

Because $C_{-m} = C_m^*$, where "$*$" denotes the complex conjugate operator, one can also write

$$p(t) = C_0 + \sum_{m=1}^{\infty}\left[C_m \exp\left(i\Omega_m t\right) + C_m^* \exp\left(-i\Omega_m t\right)\right] \tag{3.6}$$

Theoretically, a Fourier series representation of $p(t)$ may contain an infinite number of terms, however, in actual practice $p(t)$ can generally be approximated with sufficient accuracy by a relatively small number of terms. The Laplace transform of this periodic function $p(t)$ in Eq. 3.4 yields

$$\tilde{p}(s) = \sum_{m=-\infty}^{\infty} \frac{C_m}{s - i\Omega_m} \tag{3.7}$$

In this partial fraction form (a pole-residue form), $i\Omega_m$ represent equally spaced poles in the imaginary axis and C_m are the corresponding residues. Furthermore, substituting s by $i\omega$ in Eq. 3.7 leads to the corresponding frequency representation:

$$P(\omega) = \sum_{m=-\infty}^{\infty} \frac{C_m}{i\omega - i\Omega_m} \tag{3.8}$$

3.3.3 MDOF systems

The mathematical model of an N-DOF system is often written in the following second-order matrix differential equation form (Clough and Penzien, 2003; Craig and Kurdila, 2006):

$$\mathbf{M}\ddot{\mathbf{x}}(t) + \mathbf{C}\dot{\mathbf{x}}(t) + \mathbf{K}\mathbf{x}(t) = \mathbf{p}(t) \tag{3.9}$$

where $\mathbf{M}, \mathbf{C}, \mathbf{K} \in \mathbb{R}^{N\times N}$ are the mass, damping and stiffness matrices, respectively; $\mathbf{x}(t) \in \mathbb{R}^{N\times 1}$ is the displacement vector and $\mathbf{p}(t) \in \mathbb{R}^{N\times 1}$ is the load vector. Under the assumption that the system is initially at rest, that is, $\dot{\mathbf{x}}(0) = \mathbf{0}$ and $\mathbf{x}(0) = \mathbf{0}$, taking the Laplace transform of both sides of Eq. 3.9 yields

$$(\mathbf{M}s^2 + \mathbf{C}s + \mathbf{K})\tilde{\mathbf{x}}(s) = \tilde{\mathbf{p}}(s) \tag{3.10}$$

Let the *transfer matrix function* from input $\tilde{\mathbf{p}}(s)$ to output $\tilde{\mathbf{x}}(s)$ of this dynamic system be denoted by $\tilde{\mathbf{h}}(s) \in \mathbb{R}^{N\times N}$, that is,

$$\tilde{\mathbf{x}}(s) = \tilde{\mathbf{h}}(s)\tilde{\mathbf{p}}(s) \tag{3.11}$$

A general form of the *transfer function* (TF) for the displacement response at coordinate j to the loading at k is expressed as (Craig and Kurdila, 2006; Hu et al., 2016):

$$\tilde{h}_{jk}(s) = \sum_{n=1}^{N} \left(\frac{\beta_n}{s - \mu_n} + \frac{\beta_n^*}{s - \mu_n^*} \right) \tag{3.12}$$

where poles μ_n are related to the eigen values of the system and are global system parameters, independent of the coordinates j and k, but residues β_n are related to the eigen vectors of the system which are jk-dependent local system parameters.

Furthermore, the corresponding complex *frequency response function* (FRF) and unit impulse response function (IRF) are

$$H_{jk}(\omega) = \sum_{n=1}^{N} \left(\frac{\beta_n}{i\omega - \mu_n} + \frac{\beta_n^*}{i\omega - \mu_n^*} \right) \tag{3.13}$$

and

$$h_{jk}(t) = \sum_{n=1}^{N} \left[\beta_n \exp\left(\mu_n t\right) + \beta_n^* \exp\left(\mu_n^* t\right)\right] \tag{3.14}$$

respectively.

3.4 Total Response to Periodic Loading

In the time domain, the generalized expression for the displacement response $x_{jk}(t)$ at coordinate j to the load $p_k(t)$ at k is the convolution integral, as follows:

$$x_{jk}(t) = \int_0^t h_{jk}(t-\tau)\, p_k(\tau)\, d\tau \tag{3.15}$$

The total response $x_j(t)$ at coordinate j produced by a general loading involving all components of the load vector $\mathbf{p}(t)$ is obtained by summing the contributions from all load components:

$$x_j(t) = \sum_{k=1}^{N} x_{jk}(t) \tag{3.16}$$

The Laplace-domain analysis is similar to the time-domain procedure in that it involves superposition of the effects at coordinate j to the load applied at coordinate k; however, in this case both the load and the response are in the Laplace-domain. Corresponding to Eq. 3.15, the resulting displacement at the jth coordinate in the Laplace-domain $\tilde{x}_{jk}(s)$ is expressed in terms of the transfer function $\tilde{h}_{jk}(s)$

$$\tilde{x}_{jk}(s) = \tilde{h}_{jk}(s)\tilde{p}_k(s) \tag{3.17}$$

and the total response at coordinate j in the Laplace-domain $\tilde{x}_j(s)$ produced by a general loading involving all components of the load vector $\mathbf{p}(t)$ could be obtained by

$$\tilde{x}_j(s) = \sum_{k=1}^{N} \tilde{x}_{jk}(s) \tag{3.18}$$

The above equation constitutes general solutions for the equation of motion shown in Eq. 3.9 under the assumption of zero initial conditions.

3.4.1 Computing $x_{jk}(t)$ through the frequency domain

As implementing the principle of superposition in Eq. 3.16 or Eq. 3.18 is straightforward, the following derivation will focus on computing $x_{jk}(t)$ only. When the loading $p_k(t)$ is periodic with the form of Eq. 3.4, an efficient frequency domain approach for computing $x_{jk}(t)$ is developed in this section.

In Eq. 3.17, substituting $\tilde{p}_k(s)$ by Eq. 3.7 and $\tilde{h}_{jk}(s)$ by Eq. 3.12, respectively, yields

$$\tilde{x}_{jk}(s) = \sum_{n=1}^{N} \left(\frac{\beta_n}{s - \mu_n} + \frac{\beta_n^*}{s - \mu_n^*} \right) \sum_{m=-\infty}^{\infty} \frac{C_m}{s - i\Omega_m} \tag{3.19}$$

Because the common denominator in Eq. 3.19 is the product of $(s - \mu_n)$, $(s - \mu_n^*)$ and $(s - i\Omega_m)$ for all n and m terms, mathematically Eq. 3.19 can be rewritten in a partial fraction form

$$\tilde{x}_{jk}(s) = \sum_{n=1}^{N} \left(\frac{V_n}{s - \mu_n} + \frac{V_n^*}{s - \mu_n^*} \right) + \sum_{m=-\infty}^{\infty} \frac{U_m}{s - i\Omega_m} \tag{3.20}$$

From Eq. 3.20, it is evident that V_n can be obtained by the following operation (Kreyszig, 2011)

$$V_n = \lim_{s \to \mu_n} (s - \mu_n) \tilde{x}_{jk}(s) \tag{3.21}$$

Using Eq. 3.19 for $\tilde{x}_{jk}(s)$ in Eq. 3.21, one obtains

$$V_n = \beta_n \, \tilde{p}_k(\mu_n) \tag{3.22}$$

where

$$\tilde{p}_k(\mu_n) = \sum_{m=-\infty}^{\infty} \frac{C_m}{\mu_n - i\Omega_m} \tag{3.23}$$

Similarly, U_m can be obtained by

$$U_m = \lim_{s \to i\Omega_m} (s - i\Omega_m) \tilde{x}_{jk}(s) \tag{3.24}$$

and then

$$U_m = C_m \, \tilde{h}_{jk}(i\Omega_m) \tag{3.25}$$

or

$$U_m = C_m \, H_{jk}(\Omega_m) \tag{3.26}$$

Once V_n and U_m are computed, by taking the inverse Laplace transform of Eq. 3.20, one has

$$x_{jk}(t) = \sum_{n=1}^{N} \left[V_n \exp\left(\mu_n t\right) + V_n^* \exp\left(\mu_n^* t\right) \right] + \sum_{m=-\infty}^{\infty} U_m \exp(i\Omega_m t) \tag{3.27}$$

Clearly, the second summation term of the right hand side in Eq. 3.27, denoted by $u_{jk}(t)$, is the familiar steady-state response operated in the frequency domain:

$$u_{jk}(t) = \sum_{m=-\infty}^{\infty} U_m \exp(i\Omega_m t) \tag{3.28}$$

which is related to the excitation frequencies Ω_m. The first summation term of the right hand side in Eq. 3.27, denoted by $v_{jk}(t)$, is the transient response related to the system poles (complex frequencies) of the N-degrees-of-freedom system:

$$v_{jk}(t) = \sum_{n=1}^{N} \left[V_n \exp\left(\mu_n t\right) + V_n^* \exp\left(\mu_n^* t\right) \right] \tag{3.29}$$

or

$$v_{jk}(t) = \sum_{n=1}^{N} \exp\left(-\xi_n \omega_n t\right) \left[A_n \cos(\hat{\omega}_n t) + B_n \sin(\hat{\omega}_n t) \right] \tag{3.30}$$

where $A_n = 2\,\mathrm{Re}(V_n)$, $B_n = -2\,\mathrm{Im}(V_n)$, $\omega_n = |\mu_n|$, $\hat{\omega}_n = \mathrm{Im}(\mu_n) = \sqrt{1-\xi_n^2}\,\omega_n$ and $\xi_n = -\mathrm{Re}(\mu_n)/|\mu_n|$, in which $\mathrm{Re}(\cdot)$ and $\mathrm{Im}(\cdot)$ represent the real part and imaginary part, respectively.

If the initial conditions are not at rest, a free vibration response must be added to the forced-vibration response given by Eq. 3.27. Analytical solutions to compute the free vibration response of SDOF and MDOF systems have been well described in textbooks (Clough and Penzien, 2003; Craig and Kurdila, 2006).

3.4.2 Numerical implementation in the frequency domain

For getting the total response that includes the effect of the zero initial conditions by using a frequency domain approach, one has often relied on using the

technique of padding zeros. This technique is adding sufficient zeros at the end of the original excitation. Essentially, zeros are padded into the end of every period of the original excitation. So during the zero excitation interval, the free vibration damps out completely, satisfying zero initial conditions at the start of the next period (Clough and Penzien, 2003). If it does not add enough zeros, then the assumed zero initial conditions at the start of the excitation will not be sufficiently satisfied. Two points are worthy of mention: (1) the padding zero technique is not an analytically improved method to solve the transient response, and this technique works numerically only for systems possessing relatively large damping ratios; and (2) theoretically, the obtained total response is merely a steady-state response to a modified periodic loading which differs from the original periodic loading. In contrast, the newly derived method analytically solves the transient response without altering the given periodic loading, and it works for both undamped and damped systems.

3.4.3 Undamped systems

Consider an undamped N-degrees-of-freedom system subjected to a periodic loading which is zero-mean with M number of harmonic components:

$$p_k(t) = \sum_{m=1}^{M} \left[C_m \exp\left(i\Omega_m t\right) + C_m^* \exp\left(-i\Omega_m t\right) \right] \tag{3.31}$$

Because the poles μ_n of an undamped MDOF system are reduced to pure imaginary quantities $i\omega_n$, Eq. 3.27 becomes

$$x_{jk}(t) = \sum_{n=1}^{N} \left[V_n \exp\left(i\omega_n t\right) + V_n^* \exp\left(-i\omega_n t\right) \right] + \sum_{m=1}^{M} \left[U_m \exp(i\Omega_m t) + U_m^* \exp(-i\Omega_m t) \right] \tag{3.32}$$

In Eq. 3.32, one notices the similarity in computation for the transient response and steady-state response. Both response calculations are carried out in the frequency domain. While the steady state part has the coefficient U_m being computed by

$U_m = C_m\, H_{jk}(\Omega_m)$, the coefficient V_n associated with the transient response can be obtained from Eq. 3.22 in the frequency domain as

$$V_n = \beta_n\, P_k(\omega_n) \tag{3.33}$$

where

$$P_k(\omega_n) = \sum_{m=1}^{M} \left(\frac{C_m}{i\omega_n - i\Omega_m} + \frac{C_m^*}{i\omega_n + i\Omega_m} \right) \tag{3.34}$$

3.5 Numerical Examples

Three numerical examples are presented below. For illustrating the detailed operations of the proposed method, a SDOF system to a square wave loading is considered in the first example. The correctness of the numerical results will be verified by those from a time domain method. To demonstrate the effectiveness of the proposed method in practical engineering application, the second example considers a lightly damped SDOF system to a recorded El Centro earthquake loading. The third example expands the demonstration to a MDOF dynamic system. Specifically, a 6-DOF system which models a linear two-dimensional one-half of a railway structure will be studied. Throughout the numerical examples of this paper, the system of units is the MKS (meter-kilogram-second) system based on measuring lengths in meters, mass in kilograms and time in seconds. For briefness, explicit units for quantities are omitted in the following presentation.

3.5.1 Example 1: SDOF to square wave

Although the method developed in this paper is aimed at computing the response of any linear MDOF dynamic system to an arbitrary periodic loading, it is instructive to begin the numerical example with a SDOF system to a square wave excitation (see Fig. 3.1). As the equation of motion for a SDOF system is given by

$$m\ddot{x} + c\dot{x} + kx = p(t) \tag{3.35}$$

the unit *impulse response function* (IRF) of this system is written (Clough and Penzien, 2003; Craig and Kurdila, 2006)

$$h(t) = \frac{1}{m\omega_d}\, e^{-\xi\omega_1 t} \sin \omega_d t \tag{3.36}$$

where the natural frequency $\omega_1 = \sqrt{k/m}$, damping ratio $\xi = c/2\sqrt{mk}$ and damped frequency $\omega_d = \sqrt{1-\xi^2}\omega_1$. The corresponding transfer function (TF) is the Laplace transform of Eq. 3.36:

$$\tilde{h}(s) = \frac{\beta}{s-\mu} + \frac{\beta^*}{s-\mu^*} \tag{3.37}$$

where the pole $\mu = -\xi\omega_1 + i\omega_d$ and residue $\beta = -i/(2m\omega_d)$. Substituting s by $i\omega$ into Eq. 3.37 leads to the complex frequency response function (FRF):

$$H(\omega) = \frac{\beta}{i\omega-\mu} + \frac{\beta^*}{i\omega-\mu^*} \tag{3.38}$$

In the numerical study, consider $m = 1$, $k = 12$ and $c = 0$, which is an undamped system that could not be handled by using the padding-zero technique. Another reason to choose an undamped system is to demonstrate that the operation of computing the transient response is analogous to that of the steady state response (see Eq. 3.32). For this undamped system, its two system poles are pure imaginary numbers $\mu, \mu^* = \pm 3.4641i$, and the corresponding residues $\beta, \beta^* = \mp 0.1443i$. One obtains the natural frequency $\omega_1 = 3.4641$ rad/s, i.e., $f_1 = 0.5513$ Hz.

Let the system be initially at rest, and the excitation $p(t)$ be a periodic square wave function (see Fig. 3.1) with period $T = 10$ s:

$$p(t) = \begin{cases} 1 & \text{for } 0 < t < 5 \\ -1 & \text{for } 5 < t < 10 \end{cases} \tag{3.39}$$

For this square wave excitation, the complex Fourier coefficients associated with $\Omega_m = m\pi/5$ are obtained to be

$$C_m = \begin{cases} -\left(\frac{2}{m\pi}\right) i & m = 1, 3, 5, \cdots \\ 0 & m = 0, 2, 4, \cdots \end{cases} \tag{3.40}$$

Once C_m and Ω_m are determined, the corresponding $\tilde{p}(s)$ and $P(\omega)$ can be obtained from Eq. 3.7 and Eq. 3.8, respectively.

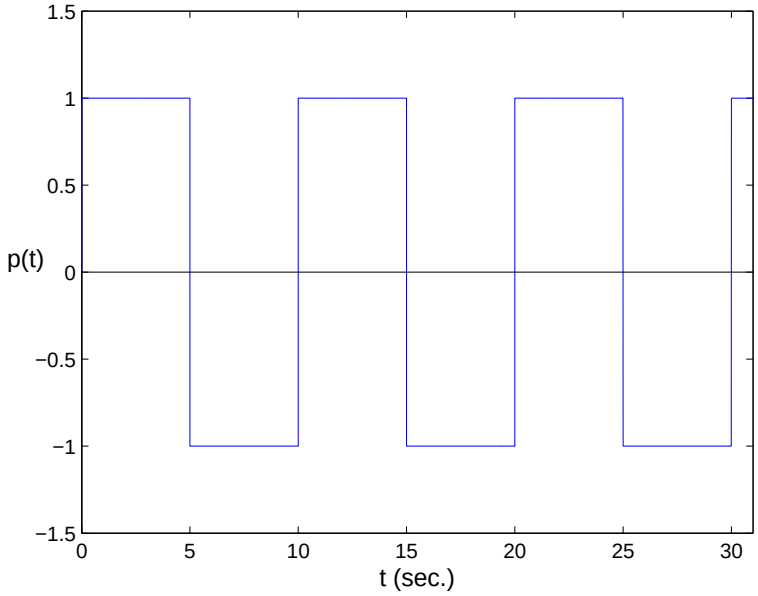

Figure 3.1. Periodic square wave excitation with period $T = 10\ s$

It is informative to use graphics to show the operations of computing the steady state response and transient response. To compute the steady state response, one follows Eq. 3.28. A graphical explanation of the steady state response operated in the frequency domain is shown in Fig. 3.2. Since quantities at the negative frequency are the complex conjugate of those at the corresponding positive frequency, only data at the positive frequency part are shown. Fig. 3.2(a) and Fig. 3.2(b) are the complex Fourier coefficients of the excitation C_m, and the frequency response function of the undamped SDOF system $H(\omega)$, respectively. Fig. 3.2(c) is obtained from multiplying Fig. 3.2(a) with Fig. 3.2(b), resulting in the complex Fourier coefficients $U_m = C_m H(\Omega_m)$ of the steady state response. The numerical quantities of U_m, $m = 0, \cdots, 10$, together with those of C_m and $H(\Omega_m)$, are listed in Table 3.1. For $m > 10$, U_m become negligibly small. Dropping all

Table 3.1. Numerical values of the components of a square wave

m	Ω_m	C_m	$H(\Omega_m)$	U_m
0	0	0	0.0833	0
1	$\frac{\pi}{5}$	$-0.6366i$	0.0862	$-0.0549i$
2	$\frac{2\pi}{5}$	0	0.0960	0
3	$\frac{3\pi}{5}$	$-0.2122i$	0.1184	$-0.0251i$
4	$\frac{4\pi}{5}$	0	0.1759	0
5	π	$-0.1273i$	0.4694	$-0.0598i$
6	$\frac{6\pi}{5}$	0	-0.4520	0
7	$\frac{7\pi}{5}$	$-0.0909i$	-0.1362	$0.0124i$
8	$\frac{8\pi}{5}$	0	-0.0754	0
9	$\frac{9\pi}{5}$	$-0.0707i$	-0.0501	$0.0035i$
10	2π	0	-0.0364	0

terms for $m > 10$, one obtains the numerical steady state response in the time domain

$$u(t) = \sum_{m=-10}^{10} U_m e^{i\Omega_m t} \tag{3.41}$$

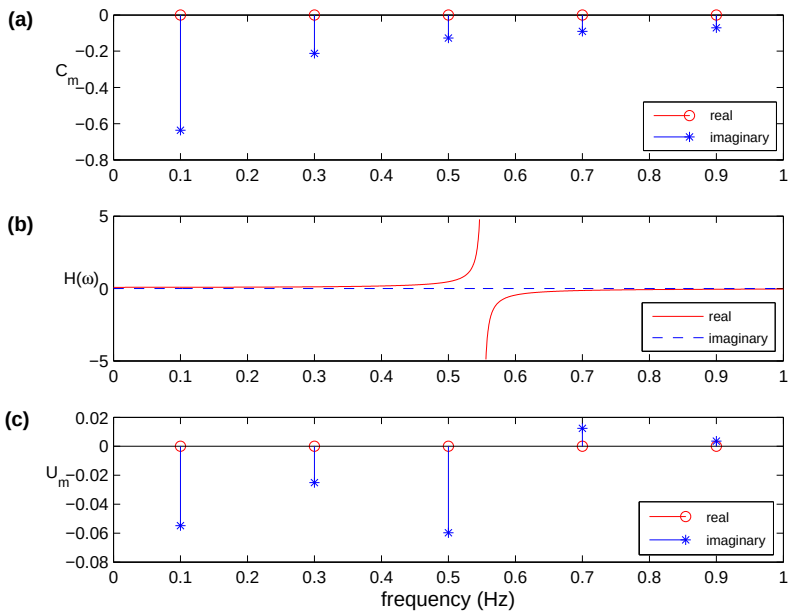

Figure 3.2. Computing the steady state response in the frequency domain: (a) complex Fourier coefficients of the excitation (b) complex frequency response function of the system (c) complex Fourier coefficients of the steady state response

The transient response of this SDOF system is expressed as

$$v(t) = Ve^{\mu t} + V^* e^{\mu^* t} \tag{3.42}$$

One follows Eq. 3.33 to get $V = \beta P(\omega_1)$, and obtains $V = 0.0000 + 0.0563i$ at $\omega_1 = 3.4641$ rad/s. Shown in Fig. 3.3 is a graphical explanation of computing transient response associated with an undamped system. In the calculation for the transient response, the operation is analogous to that for the steady state response, but the roles of the excitation and the SDOF undamped system are exchanged. Fig. 3.3(a) shows the excitation function in frequency $P(\omega)$ based on the complex Fourier coefficients of the excitation (see Eq. 3.8). Fig. 3.3(b) presents the residue β of the SDOF system at the pole μ (a pure imaginary value for an undamped system) in frequency. Fig. 3.3(c) is obtained from multiplying Fig. 3.3(a) with Fig. 3.3(b), resulting in the residue V of the response at the system pole location.

The steady state response $u(t)$ at Eq. 3.41 and the transient response $v(t)$ at Eq. 3.42 are plotted in Fig. 3.4*a* and Fig. 3.4*b*, respectively. Shown in Fig. 3.5 is the total response $x(t)$, which is the sum of $u(t)$ and $v(t)$. The correctness of $x(t)$ has been verified by the response calculated by a time domain method. One notices that the slope of total response at time $t = 0$ is zero, showing that the initial velocity of the transient response is just sufficient to cancel the initial velocity of the steady-state response for satisfying the specified initial condition $\dot{x}(0) = 0$.

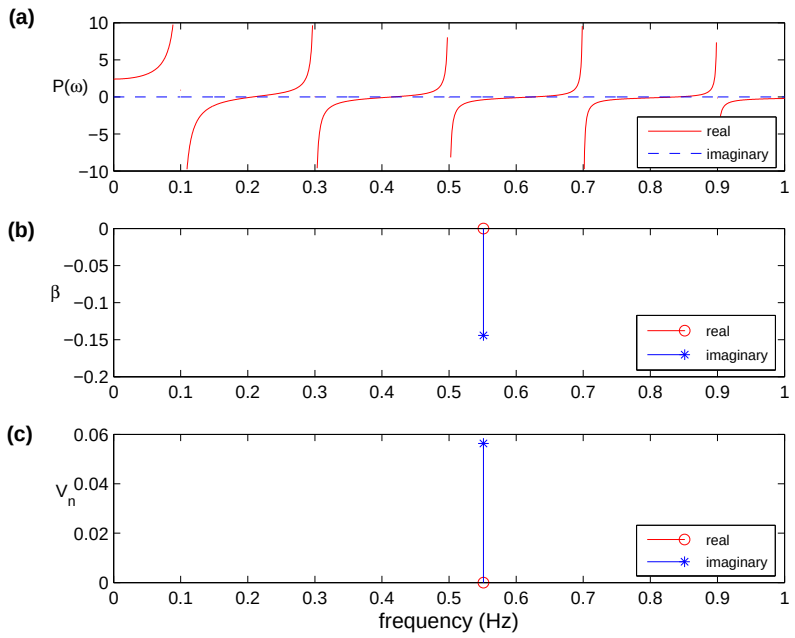

Figure 3.3. Computing the transient response of an undamped system in the frequency domain: (a) $P(\omega)$ from the complex Fourier coefficients of the excitation (b) residue β of the undamped system (c) complex Fourier coefficients of the transient response

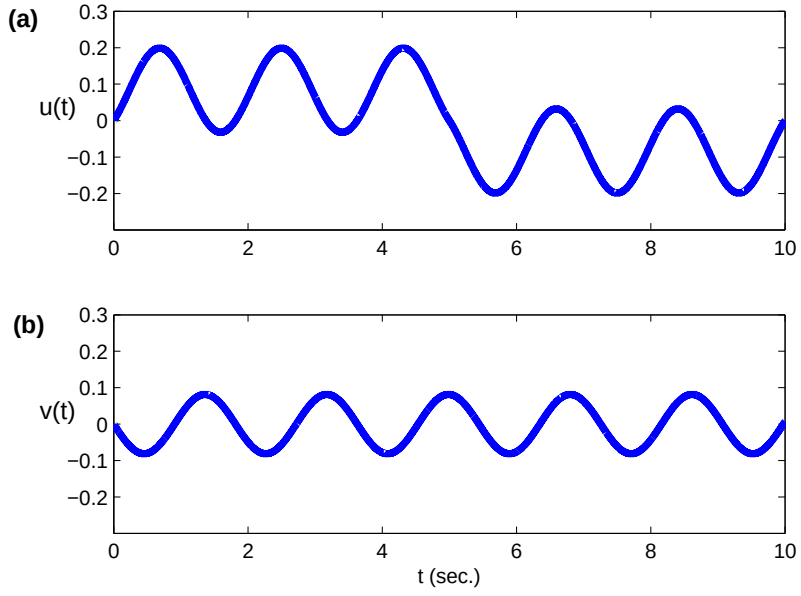

Figure 3.4. Response components for the undamped SDOF system of Example 1: (a) steady-state response, (b) transient response

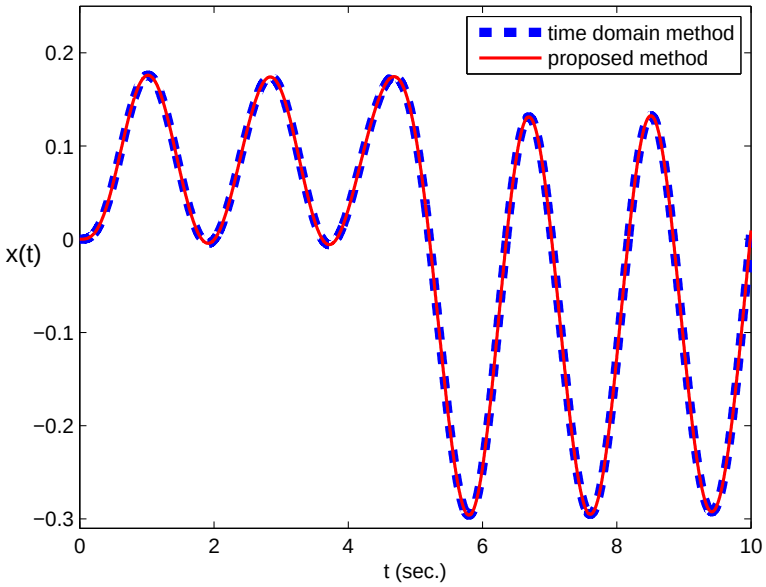

Figure 3.5. Comparison between the proposed method and a time domain method for the total response of the undamped SDOF system in Example 1

For a damped system with $m = 1$, $k = 12$ and $c = 0.3464$ (i.e., damping ratio $\xi = 5\%$), the system poles and residues are $\mu = -0.1732 \pm 3.4598$ and $\beta = 0.0000 \mp 0.1445$, respectively. The numerical operations for computing the transient response of a damped system remain the same as that of an undamped system. Because the poles of a damped system are complex numbers, one must compute the transient solution in the s-domain (see Eq. 3.29). From the operation $V = \beta\tilde{p}(\mu)$, one obtains $V = 0.0300 \pm 0.0443i$. Shown in Fig. 3.6 is the total response of this damped system computed by the proposed method, which is in excellent agreement with that by a time domain method.

3.5.2 Example 2: SDOF to earthquake loading

In designing structures to perform satisfactorily under earthquake conditions, the response of a simple oscillator, such as the SDOF frame has proved to be invaluable (Clough and Penzien, 2003). To demonstrate the applicability of the

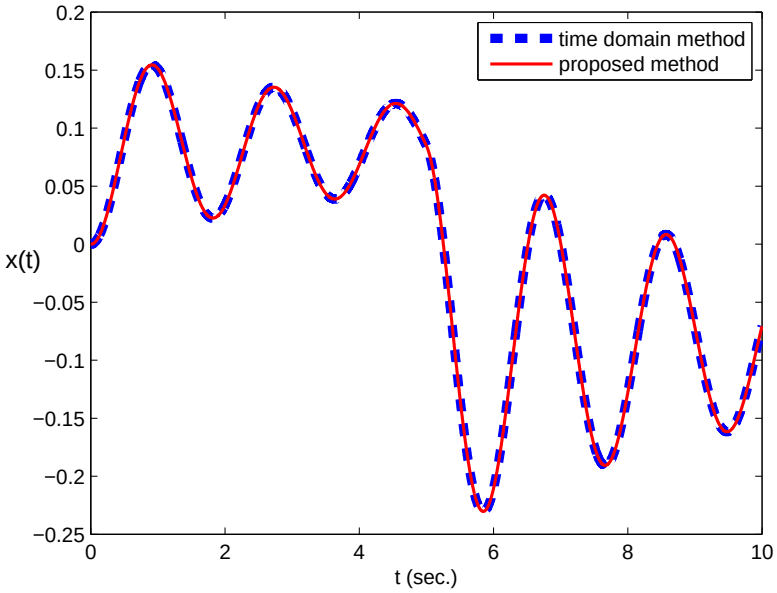

Figure 3.6. Comparison between the proposed method and a time domain method for the total displacement response of the damped SDOF system in Example 1

proposed method to an engineering problem, a lightly damped SDOF system to a measured El Centro earthquake signal is chosen in the second numerical example. The equation of motion is written

$$m\ddot{w} + c\dot{w} + kw = -m\ddot{z} \tag{3.43}$$

where z is the ground motion, w is the relative displacement between the movement of the SDOF mass and the moving base, and $-m\ddot{z}$ is the effective force.

Considering $m = 10$, $k = 40$, and $c = 0.4$, one obtains the natural frequency $\omega = 2$ rad/s, damping ratio $\xi = 0.01$, two system poles $\mu, \mu^* = -0.0200 \pm 1.9999i$, and the corresponding residues $\beta, \beta^* = 0 \mp 0.0250i$. In the computation of the effective force $p(t) = -m\ddot{z}$, a recorded El Centro earthquake acceleration signal in the East-West direction is utilized for $\ddot{z}$. This earthquake acceleration signal contains $N_s = 2048$ steps, with the sampling interval $\Delta t = 0.02$ s. Plotted in Fig 3.7 is the corresponding effective force $p(t) = -m\ddot{z}$. Conducting the FFT

for this effective force yields 1023 pairs of complex Fourier coefficients C_m, $m = 1, \cdots, 1023$, at the corresponding frequencies $\Omega_m = (2\pi m)/40.96$, together with two real Fourier coefficients at zero and Nyquist frequencies, respectively. Shown in Fig 3.8 are the absolute values of the complex Fourier coefficients C_m at the corresponding positive frequency in Hz, $f_m = \Omega_m/2\pi$. Afterwards, using Eq. 3.7 and Eq. 3.8, one can obtain the corresponding $\tilde{p}(s)$ and $P(\omega)$, respectively, based on the computed C_m and Ω_m.

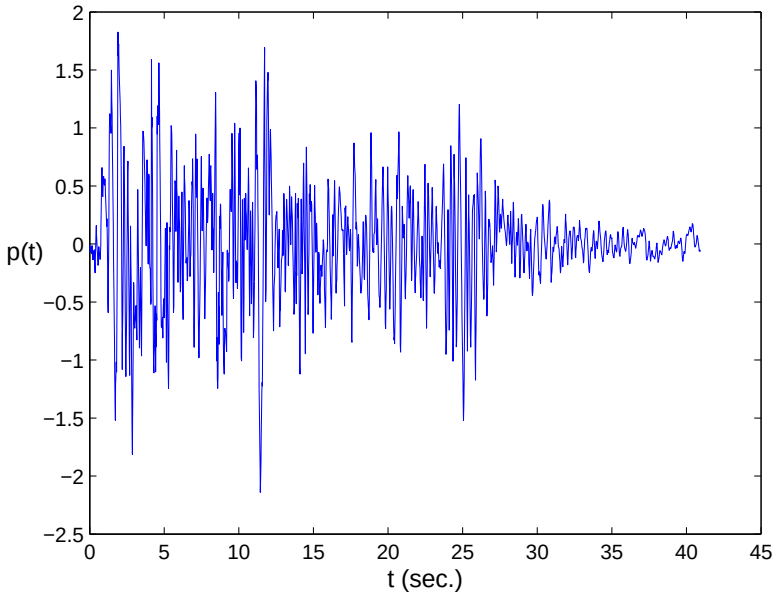

Figure 3.7. Effective force based on a recorded El Centro earthquake acceleration signal

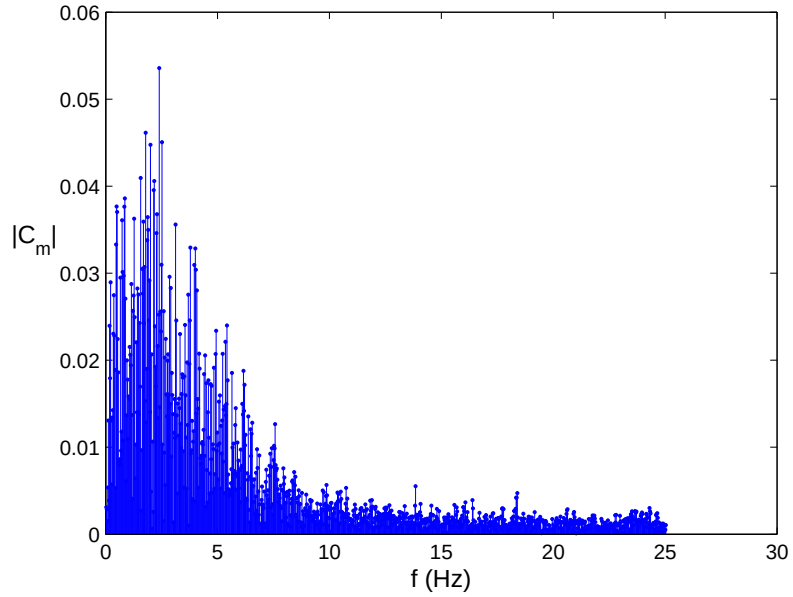

Figure 3.8. $|C_m|$ of the earthquake loading shown in Fig 3.7

Carrying out the same procedure employed in Example 1, one computes the steady-state response and the transient response, respectively. As illustrated in Example 1, only a small range of excitation frequencies that are close to the natural frequency of the SDOF system will contribute to the steady-state response (see Fig. 3.9a). The transient response (see Fig. 3.9b) does not die out quickly for a lightly damped system. Compared in Fig. 3.10 is the total response calculated by the proposed frequency domain method with that by a time domain method. Clearly, they are in excellent agreement.

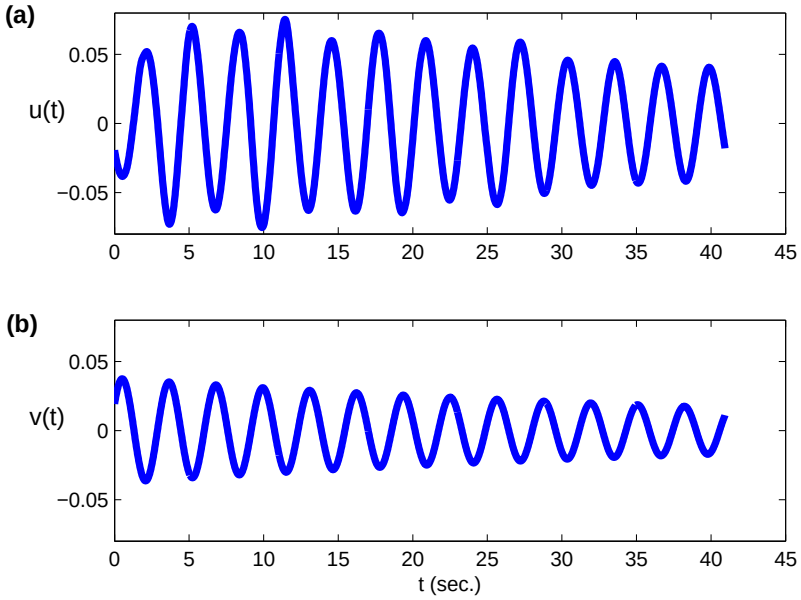

Figure 3.9. Response components of Example 2: (a) steady-state response, (b) transient response

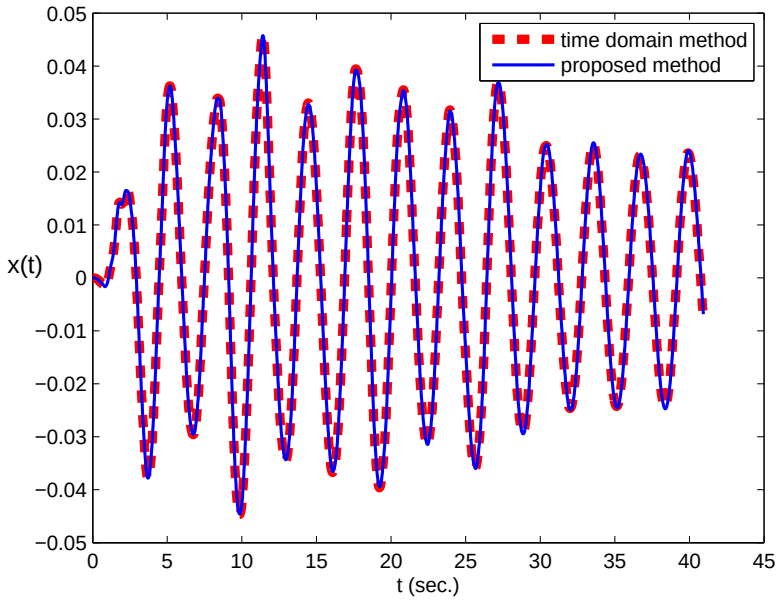

Figure 3.10. Comparison between the proposed method and a time domain method for the total response of the system in Example 2

3.5.3 Example 3: MDOF to arbitrary loading

The purpose of the third example is to demonstrate the effectiveness of the proposed method for MDOF systems to periodic loadings. Herein, the emphasis is not on the physical interpretation, but on the mathematical capability to solve the transient response of a MDOF system in the frequency domain. A linear two-dimensional one-half of a railway structure is modeled as a 6-DOF system shown in Fig. 3.11, with coordinates x_1 to x_6 specified (Hu et al., 2014). Let this 6-DOF dynamic system be initially at rest. The system is subjected to a periodic loading $p(t)$ at coordinate 2 and the displacement at coordinate 6 is sought.

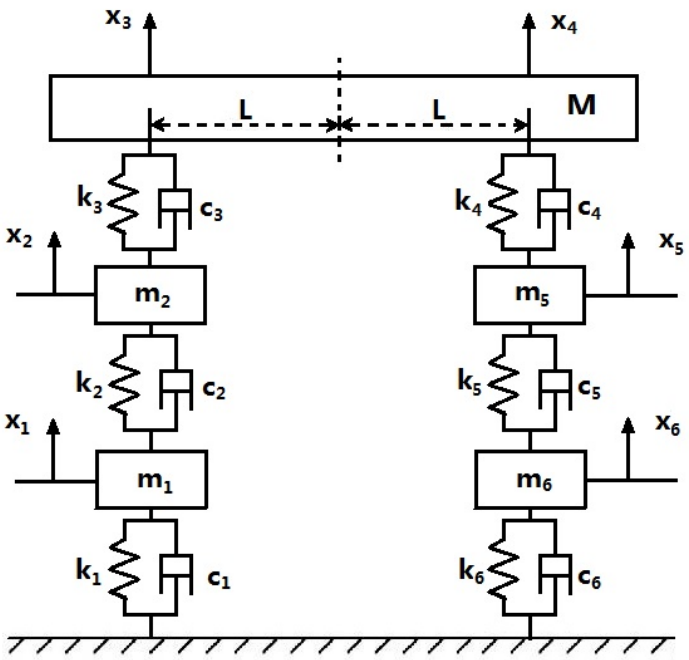

Figure 3.11. Sketch of the 6-DOF system in Example 3

Referring to Fig. 3.11, the mass and stiffness matrices of this 6-DOF system

are formulated by

$$\mathbf{M} = \begin{bmatrix} m_1 & 0 & 0 & 0 & 0 & 0 \\ 0 & m_2 & 0 & 0 & 0 & 0 \\ 0 & 0 & M/3 & M/6 & 0 & 0 \\ 0 & 0 & M/6 & M/3 & 0 & 0 \\ 0 & 0 & 0 & 0 & m_5 & 0 \\ 0 & 0 & 0 & 0 & 0 & m_6 \end{bmatrix} \tag{3.44}$$

and

$$\mathbf{K} = \begin{bmatrix} k_1 + k_2 & -k_2 & 0 & 0 & 0 & 0 \\ -k_2 & k_2 + k_3 & -k_3 & 0 & 0 & 0 \\ 0 & -k_3 & k_3 & 0 & 0 & 0 \\ 0 & 0 & 0 & k_4 & -k_4 & 0 \\ 0 & 0 & 0 & -k_4 & k_4 + k_5 & -k_5 \\ 0 & 0 & 0 & 0 & -k_5 & k_5 + k_6 \end{bmatrix} \tag{3.45}$$

respectively. The damping matrix $\mathbf{C}$ of this system has the same form as its stiffness matrix $\mathbf{K}$.

In the following numerical exercise, let $[m_1, m_2, M, m_5, m_6] = [1200, 850, 4125, 850, 1220]$; $c_1 = c_6 = 0$, $c_2 = c_5 = 3 \times 10^3$, $c_3 = c_4 = 9 \times 10^3$; $k_1 = k_6 = 3 \times 10^7$, $k_2 = k_5 = 1 \times 10^6$, and $k_3 = k_4 = 6 \times 10^6$. The transfer function $\tilde{h}_{62}(s)$ of the system can be written in the pole-residue form (Craig and Kurdila, 2006; Hu et al., 2016):

$$\tilde{h}_{62}(s) = \sum_{n=1}^{6} \left(\frac{\beta_n}{s - \mu_n} + \frac{\beta_n^*}{s - \mu_n^*} \right) \tag{3.46}$$

One can follow a state-space approach to compute μ_n and β_n (Craig and Kurdila, 2006). Shown in Table 3.2 are the numerical results for μ_n and β_n and the corresponding modal frequencies f_n and damping ratios ξ_n. Notice that poles μ_n are global parameters— independent of the input and output coordinates, but the residues β_n are specifically for the system function $\tilde{h}_{62}(s)$.

n	poles ($\times 10^2$) μ_n	residues ($\times 10^{-6}$) β_n	modal frequency (Hz.) f_n	damping ratios ξ_n
1	$-0.0043 + 0.1750i$	$0.0064 - 0.1359i$	2.7868	0.0244
2	$-0.0087 + 0.2466i$	$-0.0144 + 0.2032i$	3.9265	0.0352
3	$-0.0862 + 1.0350i$	$0.0488 - 0.1102i$	16.5298	0.0830
4	$-0.1251 + 1.2707i$	$-0.0606 + 0.0752i$	20.3221	0.0979
5	$-0.0144 + 1.5951i$	$0.0179 - 0.0056i$	25.3875	0.0090
6	$-0.0146 + 1.6083i$	$0.0019 + 0.0027i$	25.5977	0.0091

Table 3.2. System poles and residues of $\tilde{h}_{62}(s)$, and corresponding modal frequencies and damping ratios

On evaluating the proposed method, for simplicity but without losing generality, the loading at coordinate 2 is considered to be the same square wave used in Example 1. The complex Fourier coefficients C_m of this square wave excitation has been presented in Eq. 3.40, but for treating the proposed approach to be a general numerical method, FFT would be invoked to get the Fourier coefficients C_m in the following stead-state and transient response calculation.

As the values of μ_n and β_n have been obtained, the transfer function $\tilde{h}_{62}(s)$ and the complex frequency response function $H_{62}(\omega)$ of the system are readily known. Denote the steady-state response at coordinate 6 to the periodic square wave excitation at coordinate 2 as $u_{62}(t)$ which could be obtained by a traditional frequency domain approach. For brevity, the procedure to compute $u_{62}(t)$, shown in Fig. 3.12, is omitted.

On computing the corresponding transient response $v_{62}(t)$, one follows Eq. 3.29 with $N = 6$:

$$v_{62}(t) = \sum_{n=1}^{6} \left[V_n \exp\left(\mu_n t\right) + V_n^* \exp\left(\mu_n^* t\right) \right] \tag{3.47}$$

where the values of V_n are computed from $V_n = \beta_n \, \tilde{p}(\mu_n)$, noting that the function $\tilde{p}(s)$ would follow Eq. 3.7 with a finite number of C_m and Ω_m. The numerical values for V_n and $\tilde{p}(\mu_n)$ are listed in Table 3.3, and the computed $v_{62}(t)$ shown in Fig. 3.12b. One notices that the computed $v_{62}(t)$ would diminish eventually due

to damping terms of all 6 modes. The total response $x_{62}(t) = u_{62}(t) + v_{62}(t)$ is plotted in Fig. 3.13, together with a time-domain solution for verification purpose. Clearly, the computed result from the proposed frequency domain method is in excellent agreement with that of the time domain method.

n	$\tilde{p}(\mu_n)$	$V_n \times 10^{-8}$
1	$-0.0271 + 0.0499i$	$0.6611 + 0.4004i$
2	$0.0058 + 0.0427i$	$-0.8750 + 0.0559i$
3	$0.0001 + 0.0096i$	$0.1063 + 0.0454i$
4	$0.0001 + 0.0078i$	$-0.0591 - 0.0465i$
5	$-0.0008 + 0.0062i$	$0.0021 + 0.0116i$
6	$-0.0006 + 0.0063i$	$-0.0018 + 0.0011i$

Table 3.3. Values of V_n and $\tilde{p}(\mu_n)$ for $v_{62}(t)$

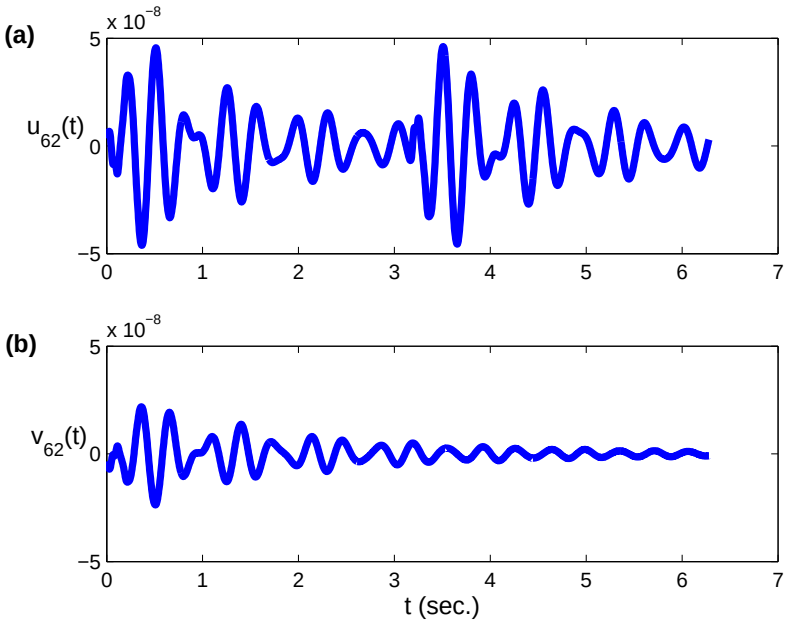

Figure 3.12. Response components of Example 3 to a square wave loading: (a) steady-state response $u_{62}(t)$, (b) transient response $v_{62}(t)$

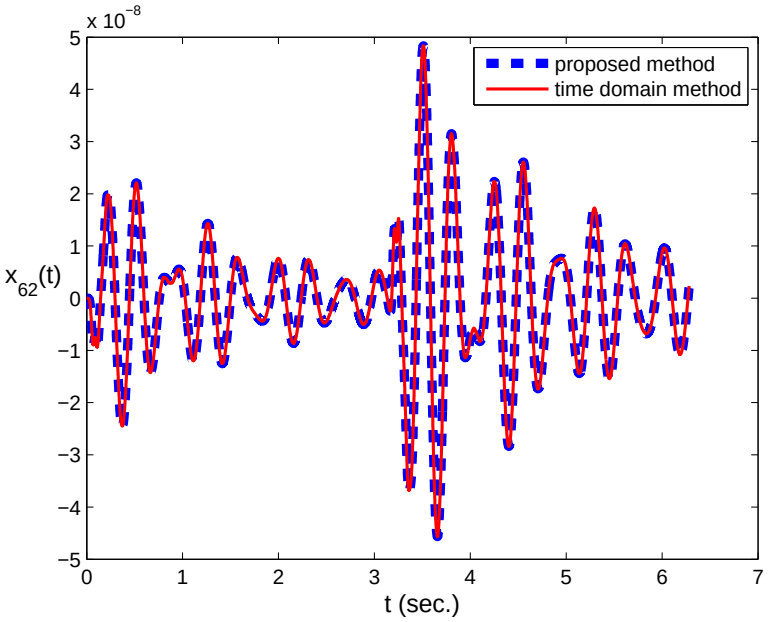

Figure 3.13. Comparison between the proposed method and a time domain method for the total response $x_{62}(t)$ of the system in Example 3 to a square wave loading

Furthermore, to demonstrate the effectiveness of the proposed method to a more complex loading, the square wave excitation is replaced by the earthquake loading that has been utilized in Example 2. With the Fourier coefficients C_m identical to those in Example 2, carrying out the proposed method yields the steady-state response $u_{62}(t)$ and the transient response $v_{62}(t)$ shown in Fig. 3.14. The total response $x_{62}(t)$ from the proposed method is plotted in Fig. 3.15(a), and the difference of $x_{62}(t)$ between the proposed method and a time domain method is shown in Fig. 3.15(b). Notice that the difference $\Delta x_{62}(t)$ is in the order of 10^{-7}, very small relative to the magnitude of $x_{62}(t)$ which is in the order of 10^{-5}.

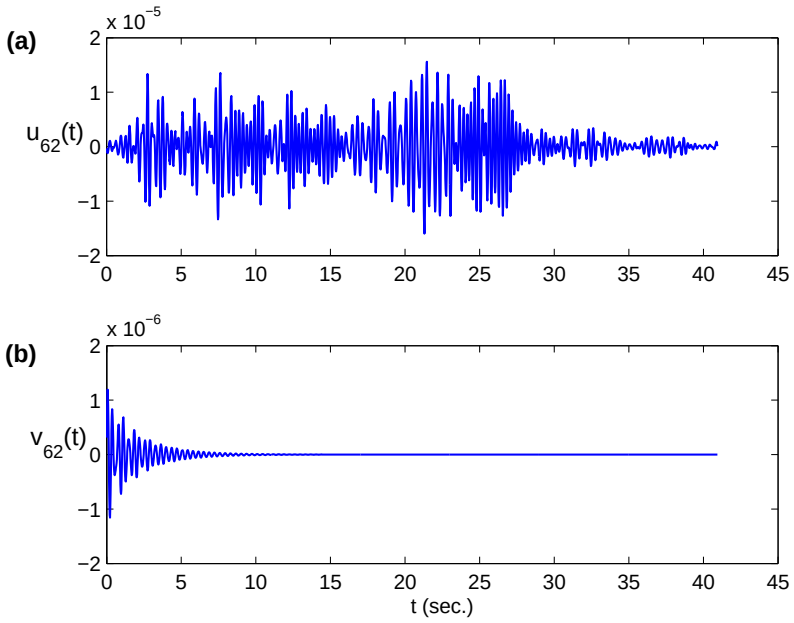

Figure 3.14. Response components of Example 3 to an earthquake loading: (a) steady-state response $u_{62}(t)$, (b) transient response $v_{62}(t)$

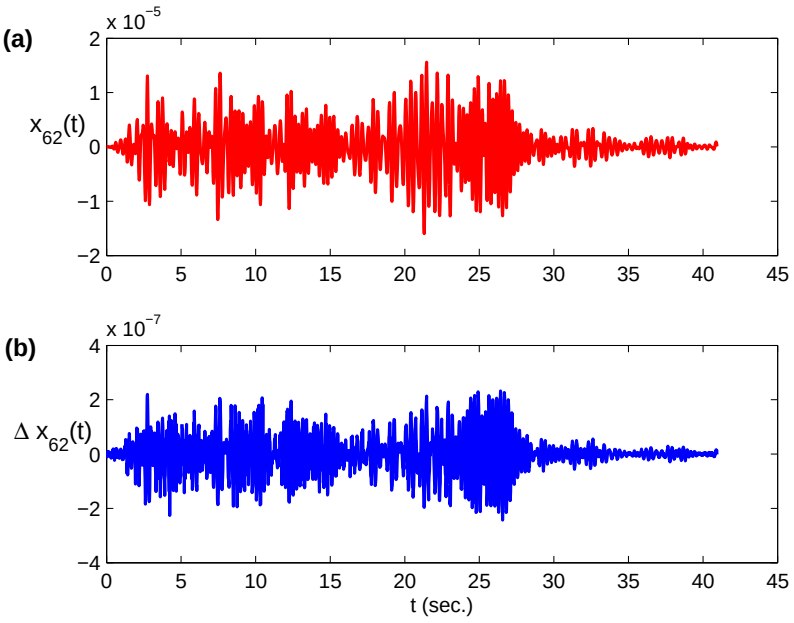

Figure 3.15. Response of Example 3 to an earthquake loading: (a) the total response $x_{62}(t)$ computed by the proposed method, (b) the difference of $x_{62}(t)$ between the proposed method and a time domain method

computation efficiency

The computational time required in the proposed method can be divided into 2 parts: (1) T_{ss}: the computational time needed to compute the steady state response, and (2) T_{tr}: the additional computational time needed to compute the transient solution. Regarding the complexity of the solution algorithms, the steady-state response for each vibration mode obtained by using FFT and inverse FFT has been well documented to be in the order $N_s \log_2 N_s$ in which N_s is the number of time steps of the excitation. In contrast, the transient response for each vibration mode, as suggested from Eq. 3.47, can be computed by a straightforward procedure in the order N_s .

By varying the number of time steps N_s from 2^7 to 2^{15}, the corresponding computation times needed by a laptop to obtain T_{ss} and T_{tr} in Example 3 are tabulated in Table 3.4. The ratio T_{tr}/T_{ss} is always less than 1, indicating that the computation time for the transient response is just a fraction of that for the steady state response. As anticipated, the ratio T_{tr}/T_{ss} becomes smaller when N_s is getting larger.

$\log_2 N_s$	T_{ss}(sec.)	T_{tr}(sec.)	T_{tr}/T_{ss}
7	0.0097	0.0060	0.6186
8	0.0119	0.0060	0.5042
9	0.0169	0.0062	0.3669
10	0.0264	0.0071	0.2689
11	0.0430	0.0081	0.1884
12	0.0943	0.0087	0.0923
13	0.2059	0.0116	0.0563
14	0.5509	0.0146	0.0265
15	1.7218	0.0238	0.0138

Table 3.4. Computational time required for the steady state solution T_{ss} and the transient solution T_{tr} against the number of time steps N_s

3.6 Concluding Remarks

Deriving a closed-form solution for the transient and total responses of SDOF/MDOF systems to arbitrary periodic excitations was an analytical contribution of this article. It showed that the transient response could be obtained in a similar fashion as the steady-state response, but the roles of the system and excitation were reversed. Together with the FFT algorithm, a very efficient numerical method has been developed to compute the total response for MDOF systems, suitable for both damped and undamped systems. The paper demonstrated that the computational time needed for getting the transient response could be much less than that for the steady state response. The correctness of the proposed method has been verified through three numerical examples by comparing the total responses obtained from the proposed method to those obtained from using a time domain method.

Chapter 4

"Impedance Function Comparison of Underwater Transducers in Air and in Water by Pole-Residue Method"

by

Bin Gao[1], Sau-Lon James Hu[2] and Harold T. Vincent[3]

will be submitted to *IEEE Transactions on sonics and ultrasonics*

---

[1] PhD Candidate, Department of Ocean Engineering, University of Rhode Island, Narragansett, RI 02882. E-mail: gaobinouc@gmail.com

[2] Professor, Department of Ocean Engineering, University of Rhode Island, Narragansett, RI 02882. E-mail: jameshu@uri.edu

[3] Research Professor, Department of Ocean Engineering, University of Rhode Island, Narragansett, RI 02882. E-mail: vincentht@uri.edu

CHAPTER 4

Manuscript 2: Impedance Function Comparison of Underwater Transducers in Air and in Water by Pole-Residue Method

4.1 Abstract

Impedance function is very essential for the transducer design. It includes many important characteristics, such as the resonant frequencies, anti-resonant frequencies, and maximum/minimum impedance values. In addition, the modal damping can also be calculated through impedance function. It is usually measured first under air loading and then under water loading. When the transducer is operated in water, some characteristics, such as resonant and anti-resonant frequencies, are changed because the acoustic medium becomes denser in water, and the added radiation mass in water is much greater than that in air. A newly developed method by pole-residue operations is applied to estimate impedance functions of acoustic transducers in this paper. With this new method, the poles of the impedance function can be used to precisely compute some characteristics of the transducer, such as modal frequencies and modal damping. Four numerical examples show the procedures to calculate impedance functions of the transducer under air and water loadings through both finite element method (FEM) and experiments. Together with their comparisons, the influence of water to the transducer, the radiating mass, has been quantified.

4.2 Introduction

Impedance function is of great importance to a transducer since it contains many essential characteristics, such as resonant/anti-resonant frequencies, capacitance, bandwidth, impedance values and damping. Accuracies of the impedance properties have significant influences on the performance of transducers.

Many studies have been carried out to estimate electrical impedance in air and in water. Multiple typical methods are introduced in textbooks, like impedance analyzer, single frequency harmonic analysis and Fourier-based analysis method using transient signals (Wilson, 1988; Sherman and Butler, 2007). A study on electrical impedance of piezoelectric ceramics under acoustic loads, with water column in and both ends covered, was performed experimentally to analyze the behavior of the resonances, anti-resonances and the effective electromechanical coupling factor of a piezoelectric ceramic ring vibrating in thickness mode (Arnold et al., 2014; Arnold et al., 2015). In addition, Sherman and Butler (2007) discuss the traditional methods on measuring the piezoelectric transducer in water and some of the quantities are discussed, such as resonant frequency, the radiation impedance, and radiation mass. In the above studies, the characteristics are usually obtained by directly reading from the impedance plot. Since impedance functions calculated by traditional methods suffers from leakage and frequency resolution problems, the characteristics, such as resonant frequencies and radiating mass, can't be accurate enough.

A recent article (Hu et al., 2016) developed an efficient pole-residue method for computing the dynamic response of the MDOF system, which showed that the poles and residues of dynamic response could be easily obtained from those of the input and system functions. Following the same theoretical principle, a new approach is used to estimate impedance functions by pole-residue operations. With this new method, some system characteristics, such as modal frequencies and damping ratios, can be accurately quantified for determining the properties of the transducer in water and the influence of fluid-structure interaction.

In this article, a tube piezoelectric transducer is simulated using finite element package Abaqus and measured experimentally both in air and in water. Four

numerical studies are provided to demonstrate the procedures of computing the impedance functions through the pole-residue operations. With the comparison of impedances in water and in air, one can obtain the influence of water loading and the change of characteristics. In addition, before the transducer is placed into water, the finite element model updating is applied to correct some coefficients of material properties based on the impedance functions obtained from FEM and experiments.

4.3 Preliminaries

This section reviews the background materials of importance to this article, including electrical impedance function, pole-residue form of a signal and radiating mass.

4.3.1 Electrical impedance function

The electrical impedance function is a function of frequency, and it is generally referred to as the total resistance generated by a device to a current flow at specific frequencies. The impedance function is defined as the ratio of voltage and current in complex form

$$Z(\omega) = \frac{V}{I} \tag{4.1}$$

Thus, the polar form conveniently captures both magnitude $|Z|$ and phase θ characteristics as

$$Z = \frac{|V|}{|I|} e^{j(\phi_V - \phi_I)} = |Z| e^{j\theta} \tag{4.2}$$

When plotted in the frequency domain, the impedance function amplitude $|Z(\omega)|$ can be used to study many characteristics of a transducer, including resonant frequencies (local minima), anti-resonant frequencies (local maxima) and damping ratio.

4.3.2 Pole-residue form of a signal

An arbitrary signal $f(t)$ can always be decomposed into a finite number of exponential components

$$f(t) = \sum_{\ell=1}^{L} \alpha_\ell \exp(\lambda_\ell t) \qquad 0 \le t < T \tag{4.3}$$

where L is the number of terms, α_ℓ and λ_ℓ are constants.

After the signal decomposition of Eq. 4.3 has been done, the Laplace transform of Eq. 4.3 yields the following pole-residue form in the Laplace-domain

$$\tilde{f}(s) = \sum_{\ell=1}^{L} \frac{\alpha_\ell}{s - \lambda_\ell} \tag{4.4}$$

where all the λ_ℓ and α_ℓ $\ell = 1, \ldots, L$ are the poles and residues of this signal. This decomposition can be done by the Prony-SS method (Hu et al., 2013; Hu et al., 2016).

4.3.3 Radiating mass

When a transducer is measured in water, one of the characteristics, resonant frequency, will be changed because of the greater radiation impedance, which adds a radiation mass M_r to the transducer. At resonance in air and in water, the frequencies can be calculated by

$$\omega_{ra} = 1/(Mc^E)^{1/2} \tag{4.5}$$

and

$$\omega_{rw} = 1/[c^E(M + M_r)]^{1/2} \tag{4.6}$$

respectively, where M represents total mass of the transducer and c^E stands for the compliance with constant electric field (Sherman and Butler, 2007).
Combining Eqs. 4.5 and 4.6, one can derive the radiation mass as

$$M_r = \frac{\omega_{ra}^2 - \omega_{rw}^2}{\omega_{rw}^2} M = \frac{f_{ra}^2 - f_{rw}^2}{f_{rw}^2} M \tag{4.7}$$

where f_{ra} and f_{rw} are the resonant frequencies (cycles per second) in air and in water.

4.4 Pole-Residue Approach of Estimating Impedance Function

4.4.1 Pole-residue method

The generalized expression for the displacement response at coordinate j to the load at k can be written by the following convolution integral

$$u_{jk}(t) = \int_0^t h_{jk}(t-\tau)\, p_k(\tau)\, d\tau \tag{4.8}$$

where $h_{jk}(t)$ is the unit impulse response function associated with coordinates j and k. Applying Laplace transform to Eq. 4.8, one can get the displacement response in the Laplace-domain

$$\tilde{u}_{jk}(s) = \tilde{h}_{jk}(s)\tilde{p}_k(s) \tag{4.9}$$

According to Eq. 4.4 and the reference (Hu et al., 2016), the external force $\tilde{p}_k(s)$ and the transfer function $\tilde{h}_{jk}(s)$ of an N-DOF system can be written as

$$\tilde{p}_k(s) = \sum_{\ell=1}^{L} \frac{\alpha_\ell}{s-\lambda_\ell} \tag{4.10}$$

and

$$\tilde{h}_{jk}(s) = \sum_{n=1}^{2N} \frac{\beta_n}{s-\mu_n} \tag{4.11}$$

where the subscripts j and k of the residues of $\tilde{p}_k(s)$ and $\tilde{h}_{jk}(s)$ are omitted for the simplification of notations.

Substituting Eqs. 4.10 and 4.11 into Eq. 4.9, it yields

$$\tilde{u}_{jk}(s) = \left(\sum_{n=1}^{2N} \frac{\beta_n}{s-\mu_n}\right)\left(\sum_{\ell=1}^{L} \frac{\alpha_\ell}{s-\lambda_\ell}\right) \tag{4.12}$$

Eq. 4.12 can be rewritten in the pole-residue form

$$\tilde{u}_{jk}(s) = \sum_{m=1}^{L+2N} \frac{\gamma_m}{s-\nu_m} \tag{4.13}$$

Comparing Eq. 4.12 and Eq. 4.13, one can notice that the total $L+2N$ response poles ν_m are originally from the L excitation poles and $2N$ system poles. Arrange the first L poles as the excitation poles, i.e., $\nu_m = \lambda_m$, $m = 1, \cdots, L$, and the last $2N$ poles as the system poles, i.e., $\nu_{m+L} = \mu_m$, $m = 1, \cdots, 2N$. For each response pole ν_m, the corresponding residue can be computed by (Hu et al., 2016)

$$\gamma_m = \lim_{s \to \nu_m} (s - \nu_m) \tilde{u}_{jk}(s) = \lim_{s \to \nu_m} (s - \nu_m) \tilde{p}_k(s) \tilde{h}_{jk}(s) \tag{4.14}$$

Thus, from Eq. 4.14, the residues corresponding to the first L response poles (at the excitation poles) are

$$\gamma_m = \lim_{s \to \nu_m} (s - \nu_m) \left(\sum_{l=1}^{L} \frac{\alpha_\ell}{s - \lambda_\ell} \right) \tilde{h}_{jk}(s) = \alpha_m \, \tilde{h}_{jk}(\lambda_m), \qquad m = 1, \cdots, L \tag{4.15}$$

and the residues corresponding to the last $2N$ response poles (at the system poles) are

$$\gamma_{m+L} = \lim_{s \to \nu_{m+L}} (s - \nu_{m+L}) \, \tilde{p}_k(s) \left(\sum_{n=1}^{2N} \frac{\beta_n}{s - \mu_n} \right) = \beta_m \, \tilde{p}_k(\mu_m), \qquad m = 1, \cdots, 2N \tag{4.16}$$

Eqs. 4.15 and 4.16 indicate that all residues of the response can be easily obtained from simple operations of the poles and residues of the excitation and system transfer function. Generally, this pole-residue method can be applied to the response calculation to arbitrary loading for a linear multi-DOF system, not only limited to compute the displacement response due to external force.

4.4.2 pole-residue operations for computing system functions

Shown in Table 4.1 are the decomposition outcomes of input and output signals by multi-signal Prony-SS method, i.e., global poles, input residues, and output residues. One can distinguish the input poles and system poles by observing the columns 1 and 2 in Table 4.1. In column 2, the input residues can be divided two groups, nonzero ones α_ℓ and zero or negligibly small ones. In column 1, the global

poles are correspondingly divided into two groups, ν_ℓ and ν_{n+L}. The input poles are the ones ν_ℓ in the group of nonzero input residues while the system poles μ_n are the remaining ones ν_{n+L} in the group of zero or negligibly small input residues (Cao et al., 2017), which can also be interpreted that the system poles are simply the output poles ν minus the input poles ν_ℓ. With the system poles, one can accurately calculate the modal frequencies and modal damping of the system by

$$\omega_n = |\nu_{n+L}|, \quad \xi_n = \frac{-\mathrm{Re}(\nu_{n+L})}{|\nu_{n+L}|} \tag{4.17}$$

Eq. 4.9 shows the relationship among input, system and output in the Laplace domain for a system initially at rest. Thus, one can simply calculate the transfer function by

$$\tilde{h}_{jk}(s) = \frac{\tilde{u}_{jk}(s)}{\tilde{p}_k(s)} \tag{4.18}$$

From Eqs. 4.10 and 4.13, one obtains

$$\tilde{p}_k(s) = \sum_{\ell=1}^{L} \frac{\alpha_\ell}{s - \nu_\ell} \tag{4.19}$$

$$\tilde{u}_{jk}(s) = \sum_{m=1}^{2N+L} \frac{\gamma_m}{s - \nu_m} \tag{4.20}$$

Notice that $\tilde{p}_k(s)$ and $\tilde{u}_{jk}(s)$ can be expressed by the global poles ν, input residues α and output residues γ.

Combining Eqs. 4.18 to 4.20, it yields the transfer function

$$\tilde{h}_{jk}(s) = \left(\sum_{m=1}^{2N+L} \frac{\gamma_m}{s - \nu_m} \right) / \left(\sum_{\ell=1}^{L} \frac{\alpha_\ell}{s - \nu_\ell} \right) \tag{4.21}$$

By substituting s with $i\omega$, Eq. 4.21 becomes complex FRF

$$H_{jk}(\omega) \equiv \tilde{h}_{jk}(s = i\omega) = \left(\sum_{m=1}^{2N+L} \frac{\gamma_m}{i\omega - \nu_m} \right) / \left(\sum_{\ell=1}^{L} \frac{\alpha_\ell}{i\omega - \nu_\ell} \right) \tag{4.22}$$

Table 4.1. Summary of operations for calculating the system functions $\tilde{h}_{jk}(s)$

global poles	input residues	output residues
ν_ℓ $\ell = 1, \cdots, L$	α_ℓ $\ell = 1, \cdots, L$	γ_ℓ $\ell = 1, \cdots, L$
ν_{n+L} $n = 1, \cdots, 2N$	0	γ_{n+L} $n = 1, \cdots, 2N$

4.5 Impedance Functions Calculation and Their Comparisons

Impedance function of a cylindrical piezoelectric transducer is studied in this article. The transducer is simulated using Abaqus under two conditions – with and without water. Furthermore, the transducer is also tested experimentally in air and in water to obtain impedance function and verify FE models. Additionally, to make the simulation accurate, finite element model updating is carried out before the transducer is placed into water.

4.5.1 Impedance function in air from FEM

Shown in Fig. 4.1, the tube transducer used in this study is radially polarized and made of piezoelectric material PZT4 with dimensions $13mm \times 26mm \times 22mm$ ($L \times OD \times ID$). When studying the mechanical properties, the transducer in air is treated as in vacuum because the influence of air is negligible. The piezoelectric transducer is electroded on both the inner and outer surfaces. Since compliance coefficients are not allowed for elasticity in Abaqus, together with the manufacturer specification sheet (STEMiNC, 2018), the e-form property matrices in a cylindrical system are calculated:

Elasticity (stiffness) matrix $\mathbf{c}^E$:

$$\begin{bmatrix} 132.64 & 76.92 & 76.92 & 0 & 0 & 0 \\ 76.92 & 134.68 & 63.76 & 0 & 0 & 0 \\ 76.92 & 63.76 & 134.68 & 0 & 0 & 0 \\ 0 & 0 & 0 & 25.64 & 0 & 0 \\ 0 & 0 & 0 & 0 & 25.64 & 0 \\ 0 & 0 & 0 & 0 & 0 & 35.46 \end{bmatrix} \text{GPa}$$

Piezoelectric coupling matrix (stress coefficients $\mathbf{e}$):

$$\begin{bmatrix} 20.9048 & -3.1669 & -3.1669 & 0 & 0 & 0 \\ 0 & 0 & 0 & 12.7179 & 0 & 0 \\ 0 & 0 & 0 & 0 & 12.7191 & 0 \end{bmatrix} \text{C/m}^2$$

Dielectric matrix with constant strain $\boldsymbol{\varepsilon}^{\boldsymbol{S}}$:

$$\begin{bmatrix} 4.819 & 0 & 0 \\ 0 & 6.752 & 0 \\ 0 & 0 & 6.752 \end{bmatrix} \times 10^{-9} \text{ F/m}$$

The 1-, 2- and 3-direction are radial, tangential, and axial, respectively. In this model, the poling direction is radially outwards from the axis of symmetry. The mass density is 7900 kg/m^3. A light Rayleigh damping model is assumed for the piezoelectric material with coefficients $\alpha = 700$, $\beta = 1.3 \times 10^{-9}$. As Fig. 4.1 shows, the transducer is modeled by a piece of cross section of the cylinder tube structure with 8-node axisymmetric piezoelectric elements (CAX8E).

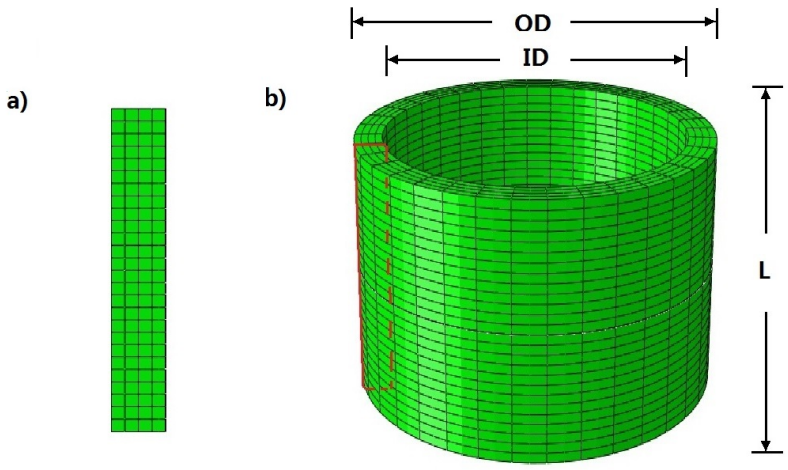

Figure 4.1. The geometry and finite element model of the transducer in air: a) 2D axisymmetric model, b) 3D model

Fig. 4.2 shows the modal analysis results of the transducer under short-circuit condition, whose resonant frequencies under 200 kHz are 43.790 kHz, 60.189 kHz and 129.924 kHz. Likewise, the modal frequencies under open-circuit condition, corresponding to the anti-resonance of the transducer, are 46.744 kHz, 60.203 kHz, and 145.962 kHz. Based on values of α and β, the corresponding theoretical modal damping are 0.1451%, 0.1171%, and 0.0959%.

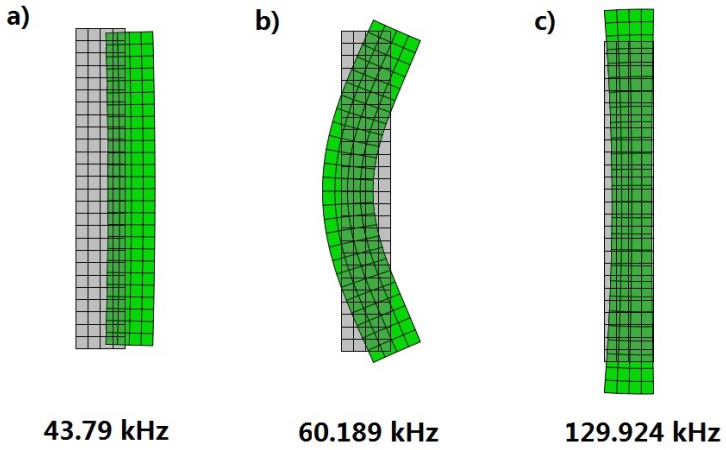

Figure 4.2. Modal analysis results of the transducer under short-circuit condition (grey for original shape, green for deformed one): a) radial (breathing) mode, b) bending mode and c) longitudinal mode

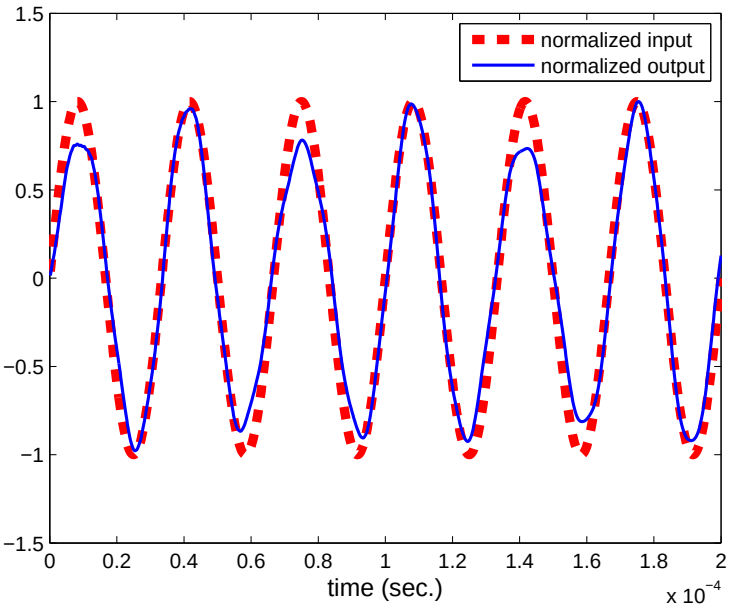

Figure 4.3. Normalized FEM input voltage and output nodal charge for the transducer in air: voltage scale 1 V, charge scale 7.8253×10^{-9} C

To calculate impedance function, one carries out the dynamic analysis. The

excitation of a sinusoidal electrical potential $v(t)$ with the amplitude 1 V and the frequency 30 kHz is applied through electrical boundary condition, while the reactive electrical charge $q(t)$ is computed. Both signals are shown in Fig. 4.3. The time increment and total time duration are 0.2 μs and 200 μs, respectively.

Applying Prony-SS method to decompose $v(t)$ and $q(t)$ simultaneously, the corresponding global poles ν and residues λ and γ are shown in columns 1 through 3 of Table 4.2. The corresponding modal frequencies and modal damping are also calculated by $\omega = |\nu|$ and $\xi = -\text{real}(\nu)/|\nu|$ listed in columns 4 and 5 of Table 4.2. The modal frequencies and modal damping match the results of modal analysis very well, with relative errors of the three modes as $\{0.02\%, 0.06\%, 0.022\%\}$ and $\{0.05\%, 6.35\%, 0.46\%\}$, respectively. Unlike traditional method, the dominant mode, longitudinal mode (129.924 kHz), can be determined by the largest value in Column 6 of Table 4.2 before calculating impedance function. By pole-residue operation in Eq. 4.22, one can calculate the frequency response function $H_{QV}(\omega)$. Since the electrical current $i(t) = \dot{q}(t)$, the impedance function will be obtained using

$$Z(\omega) = \frac{V(\omega)}{i\omega Q(\omega)} = \frac{1}{i\omega H_{QV}(\omega)} \tag{4.23}$$

Shown in Fig. 4.4 is the impedance plot and all resonant and anti-resonant frequencies match pretty well with modal analysis results. The accuracy and efficiency has been stated in references (Su, 2016; Hu et al., 2017).

Table 4.2. FEM signal decomposition results of the transducer in air

poles ν $\times 10^5$ (1)	input residues λ (2)	output residues γ $\times 10^{-8}$ (3)	modal frequencies kHz (4)	modal damping (5)	$\lvert\gamma/\tilde{V}(\nu)\rvert$ $\times 10^{-3}$ (6)
$0.0000 + 1.8850i$	$0.0188 - 0.4996i$	$0.0125 - 0.3391i$	30.0000	$--$	$--$
$0.0000 - 1.8850i$	$0.0188 + 0.4996i$	$0.0125 + 0.3391i$	30.0000	$--$	$--$
$-0.0040 + 2.7507i$	$0.0000 - 0.0000i$	$-0.0024 + 0.0491i$	43.7792	0.1450%	0.1046
$-0.0040 - 2.7507i$	$0.0000 + 0.0000i$	$-0.0024 - 0.0491i$	43.7792	0.1450%	0.1046
$-0.0041 + 3.7793i$	$-0.0000 - 0.0000i$	$-0.0000 + 0.0001i$	60.1494	0.1097%	0.0004
$-0.0041 - 3.7793i$	$-0.0000 + 0.0000i$	$-0.0000 - 0.0001i$	60.1494	0.1097%	0.0004
$-0.0078 + 8.1453i$	$0.0000 - 0.0000i$	$-0.0021 + 0.0132i$	129.6361	0.0955%	0.4391
$-0.0078 - 8.1453i$	$0.0000 + 0.0000i$	$-0.0021 - 0.0132i$	129.6361	0.0955%	0.4391

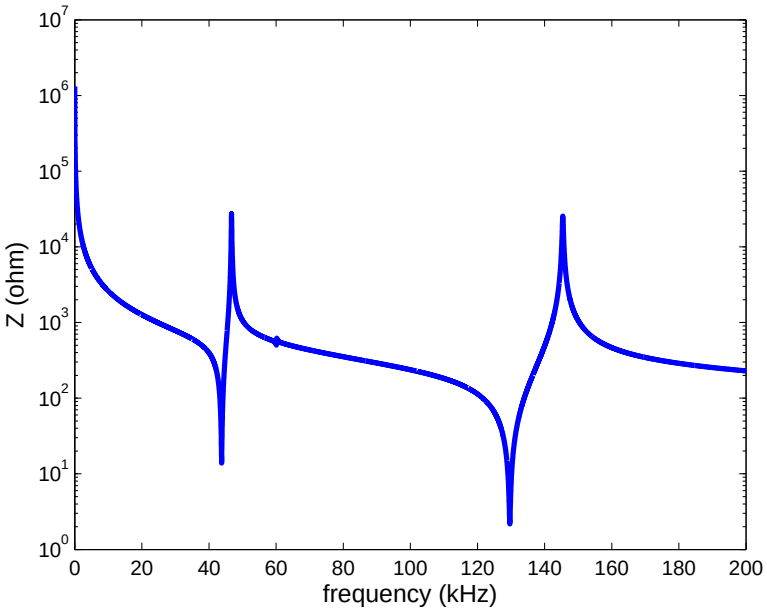

Figure 4.4. Impedance plot in air from FEM

4.5.2 Impedance function in air from experiment

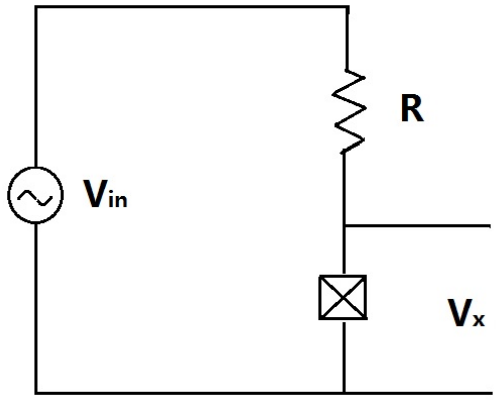

Figure 4.5. Experiment setup circuit in air

The circuit diagram of the experiment is shown in Fig. 4.5, where the resistance $R = 324$ ohm. The input voltage, $V_{in} = \exp(-10000t)$ volt, is generated by the function generator (Tektronix) with time increment 0.2 μs and time duration 100 μs, and V_x is the response voltage across the piezoelectric transducer (shown

in Fig. 4.6).

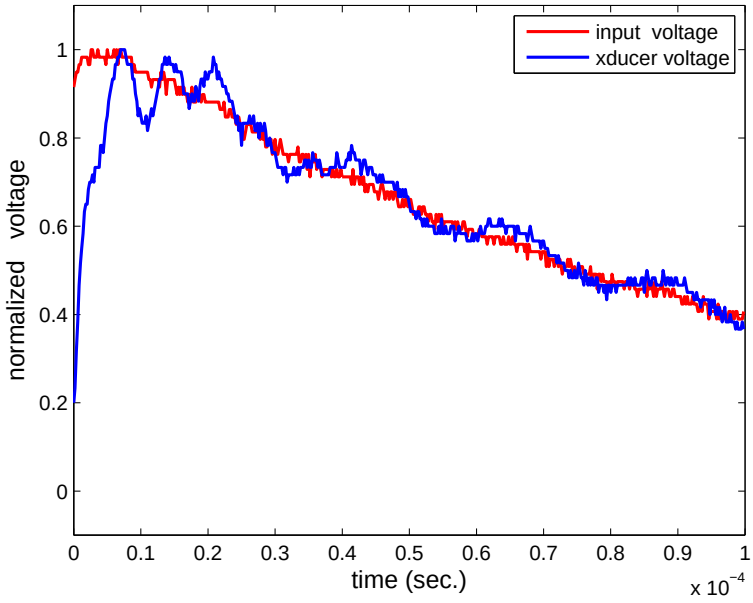

Figure 4.6. Normalized experimental input voltage and voltage across the transducer (xducer voltage) in air: input voltage scale 4.7200 V, xducer voltage scale 4.8000 V

Similarly, Table 4.3 shows the decomposition results of V_{in} and V_x and the corresponding modal frequencies and modal damping using the Prony-SS method. The second row of Table 4.3 shows a real pole, which is neither input pole nor system poles. This component is caused by the sudden increase from 0 V to 1 V when the function generator outputs an exponential decay function. The decay time of this component is about 2 μs and will negatively die out very quickly. As shown in Table 4.3, the bending mode doesn't participate since it is very hard to be excited experimentally. The impedance function can be calculated through

$$Z(\omega) = \frac{V_x}{V_R/R} = \frac{V_x}{V_{in} - V_x} R = \frac{H(\omega)}{1 - H(\omega)} R \tag{4.24}$$

where $H(\omega)$, the FRF from input voltage to response voltage across the transducer, can be calculated by the pole-residue operations in Eq. 4.22. Plotted in Fig. 4.7

is the comparison of impedance function between FEM and experiment results. There are some discrepancies at both resonant and anti-resonant frequencies. In addition, the modal damping of FE model is much smaller than the real transducer. Therefore, material parameters from the manufacturer used in FEM are inaccurate and need to be updated before the model is used for further studies.

Table 4.3. Experimental signal decomposition results of the transducer in air

poles (ν) $\times 10^5$ (1)	input residues (2)	output residues (3)	modal frequencies $\lvert\nu\rvert/2\pi$ (kHz) (4)	damping $-\text{real}(\nu)/\lvert\nu\rvert$ (5)
$-0.0991 + 0.0000i$	$5.0153 - 0.0000i$	$5.1581 + 0.0000i$	$--$	$--$
$-4.6614 + 0.0000i$	$-0.7886 + 0.0000i$	$-5.2702 + 0.0000i$	$--$	$--$
$-0.0875 + 2.7682i$	$0.0210 + 0.0111i$	$0.1269 + 0.0695i$	44.0795	0.0316
$-0.0875 - 2.7682i$	$0.0210 - 0.0111i$	$0.1269 - 0.0695i$	44.0795	0.0316
$-0.5408 + 9.0705i$	$0.0334 - 0.0163i$	$0.2764 - 0.1057i$	144.6186	0.0595
$-0.5408 - 9.0705i$	$0.0334 + 0.0163i$	$0.2764 + 0.1057i$	144.6186	0.0595

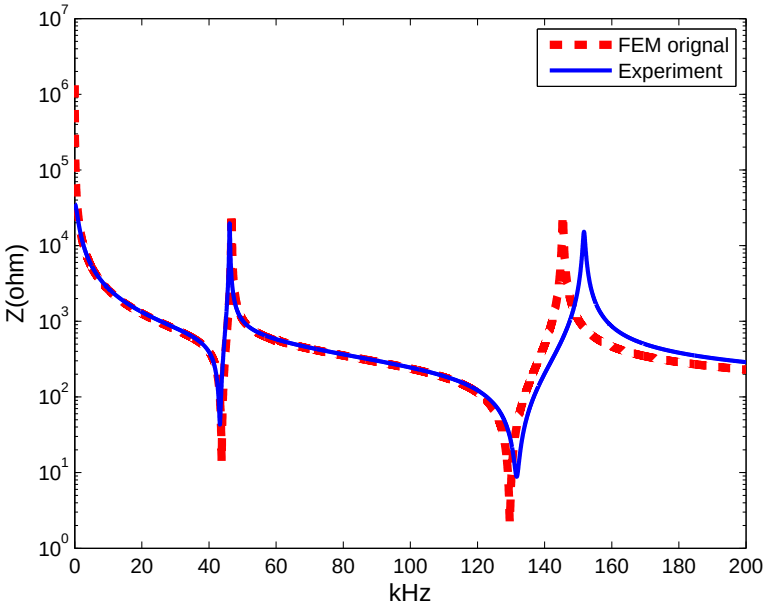

Figure 4.7. Impedance function comparison of the transducer in air: original FEM v.s. experiment

4.5.3 Model updating

The model updating method employed in this study is the cross-model cross-mode (CMCM) method. Only four major coefficients, i.e. elastic property s_{11}/c_{11},

s_{12}/c_{12}, electrical permittivity $\varepsilon_{33}^{T}/\varepsilon_{33}^{S}$ and piezoelectric coupling d_{31}/e_{31}, of the piezoelectric material are updated instead of all 10 parameters (Su, 2016).

With the two modal frequencies of the target short-circuit model: 43.26 kHz and 131.7 kHz, those of the target open-circuit model: 46.18 kHz and 151.7 kHz, and the impedance values from the impedance function

$$Z_0 = \{12860\ 5442\ 3902\ 2728\ 2267\ 1802\ 1580\ 1327\ 1195\ 1031\}\ \Omega$$

at the corresponding frequencies

$$f_0 = \{2\ 5\ 7\ 10\ 12\ 15\ 17\ 20\ 22\ 25\}\ \text{kHz},$$

one can apply the extended CMCM method to perform the finite element model updating and obtain the corrected properties of piezoelectric material. In addition, a thin polyurethane layer with density 1012 kg/m^3 is coated on the surfaces of this transducer to isolate water in further study. Since this layer is only 0.5 mm thick and changes the electrical and mechanical system very slightly, to simplify the simulation, this polyurethane material is considered to be linearly isotropic elastic material in current study. To follow similar procedures, together with the modal frequencies of the target short-circuit model: 41.9 kHz and 126.1 kHz, one can update the Young's modulus and Poison's ratio of the 'linear' polyurethane material (more details shown in Appendix C).

Shown in Table 4.4 is the comparison of properties between original and updated ones. After the model updating, the outcomes of finite element model have very good agreement with those of experiments, which are shown in Figs. 4.8 and 4.9.

Table 4.4. The comparison of properties between original and updated models

material parameters			unit	original	updated	relative error
PZT manufacturer form	Young's modulus	Y_{11}	GPa	86	84.390	-1.91%
	Poison's ratio	ν_{12}	—	0.2126	0.2844	25.25%
	coupling	d_{31}	pm/V	-140	-141.98	1.40%
	permittivity	$\varepsilon_{33}^T/\varepsilon_0$	—	1400	1376.4	-1.71%
PZT damping	mass term	α	—	700	2446.4	—
	stiffness term	β	$\times 10^{-9}$	1.3	3.6782	—
polyurethane elastic	Young's modulus	E_{poly}	GPa	1	1.4706	—
	Poison's ratio	ν_{poly}	—	0.3	0.3076	—
polyurethane damping	mass term	α_{poly}	—	—	18320	—
	stiffness term	β_{poly}	$\times 10^{-6}$	—	2.2427	—

Table 4.5. Updated FEM signal decomposition results of the transducer in air (with polyurethane layer)

poles ν $\times 10^5$ (1)	input residues λ (2)	output residues γ $\times 10^{-8}$ (3)	modal frequencies kHz (4)	damping (5)	$\lvert\gamma/\tilde{V}(\nu)\rvert$ $\times 10^{-3}$ (6)
$-0.0000 + 1.8850i$	$0.0188 - 0.4996i$	$0.0050 - 0.1702i$	30.0000	$--$	$--$
$-0.0000 - 1.8850i$	$0.0188 + 0.4996i$	$0.0050 + 0.1702i$	30.0000	$--$	$--$
$-0.0279 + 2.6306i$	$0.0000 + 0.0000i$	$-0.0002 + 0.0279i$	41.8696	0.0106	0.0499
$-0.0279 - 2.6306i$	$0.0000 - 0.0000i$	$-0.0002 - 0.0279i$	41.8696	0.0106	0.0499
$-0.0602 + 3.6074i$	$0.0000 + 0.0000i$	$-0.0000 + 0.0001i$	57.4214	0.0167	0.0003
$-0.0602 - 3.6074i$	$0.0000 - 0.0000i$	$-0.0000 - 0.0001i$	57.4214	0.0167	0.0003
$-0.1049 + 7.9338i$	$0.0000 + 0.0000i$	$-0.0011 + 0.0079i$	126.2812	0.0132	0.2480
$-0.1049 - 7.9338i$	$0.0000 - 0.0000i$	$-0.0011 - 0.0079i$	126.2812	0.0132	0.2480

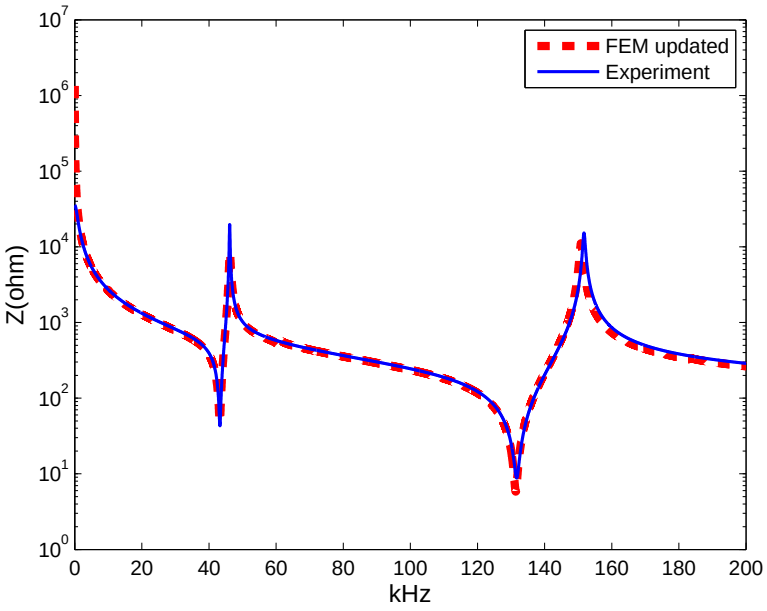

Figure 4.8. Impedance function comparison of the transducer in air: updated FEM v.s. experiment (before adding polyurethane layer)

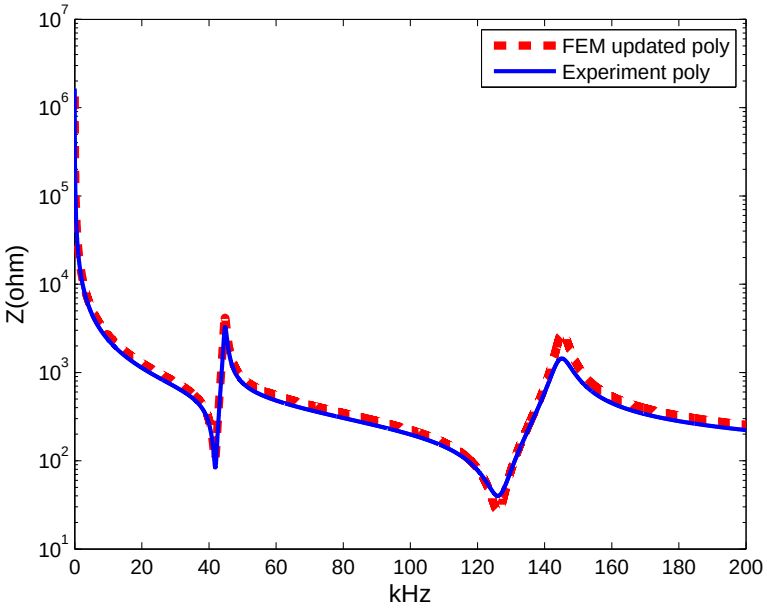

Figure 4.9. Impedance function comparison of the transducer in air: updated FEM v.s. experiment (after adding polyurethane layer)

4.5.4 Impedance function in water from FEM

After studies in air, the acoustic water will be added to FE model. The water domain is spherical with radius of 20 cm and shown in Fig. 4.10 is only one quarter cross-section of the sphere. The acoustic water is simulated by axisymmetric acoustic elements ACAX4 with two properties of density 1000 kg/m^3 and bulk modulus 2.1404 GPa. The fluid-structural interaction is defined by a tie constraint, which automatically computes the region of influence for each internally generated acoustic-structural interface element. To simulate an infinite domain, the nonreflective boundary is applied to the water domain to absorb the acoustic waves.

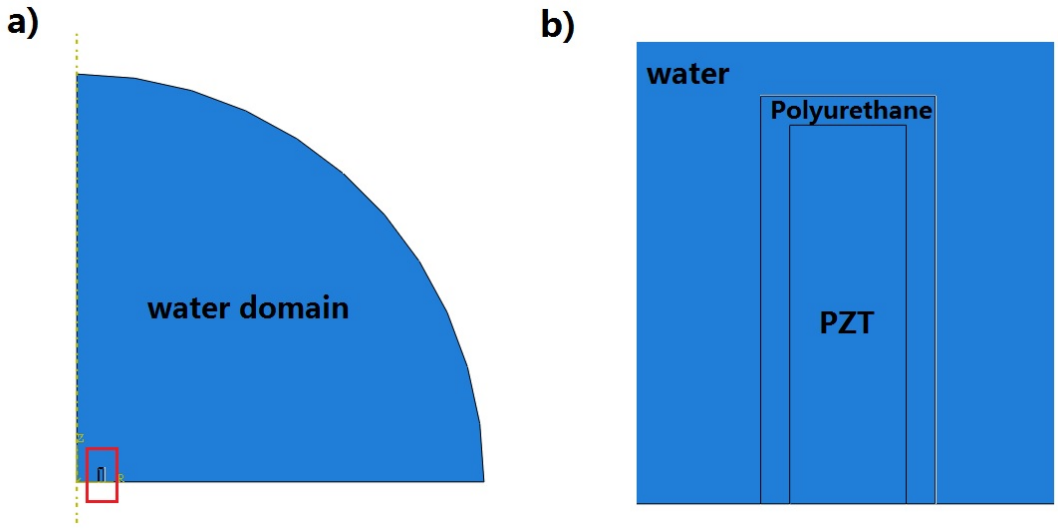

Figure 4.10. FEM set-up of the transducer in water: a) water domain and the transducer (left bottom corner), b) the transducer with polyurethane layer

A continuous sinusoidal electrical potential $v(t)$ with the amplitude 1 volt and the frequency 30 kHz is applied to the transducer as an electrical boundary condition on inside surface and the reaction charge $q(t)$ is collected. Total time duration is 200 μs with time increment 0.2 μs. Shown in Fig. 4.11 are the normalized input and output signals.

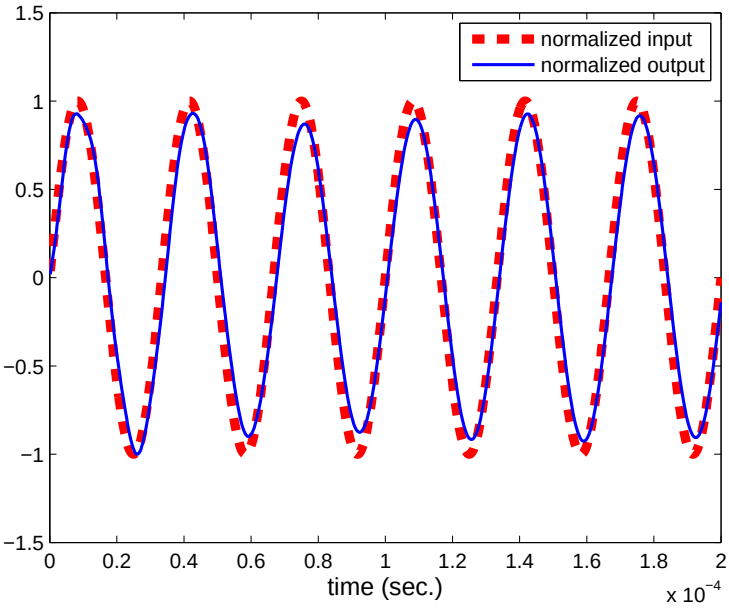

Figure 4.11. Normalized input voltage and output charge for the transducer in water: input scale 1 V, output scale 3.0925×10^{-9} C

The decomposition results of $v(t)$ and $q(t)$ are shown in Table 4.6, and the impedance function comparison of the transducer between in air and in water from FEM is plotted in Fig. 4.12.

Table 4.6. FEM signal decomposition results of the transducer in water

poles ν $\times 10^5$ (1)	input residues λ (2)	output residues γ $\times 10^{-8}$ (3)	modal frequencies kHz (4)	damping (5)	$\lvert\gamma/\tilde{V}(\nu)\rvert$ $\times 10^{-3}$ (6)
$0.0000 + 1.8850i$	$0.0188 - 0.4995i$	$-0.0148 - 0.1398i$	30.0000	$--$	$--$
$0.0000 - 1.8850i$	$0.0188 + 0.4995i$	$-0.0148 + 0.1398i$	30.0000	$--$	$--$
$-0.1037 + 1.4171i$	$0.0000 - 0.0000i$	$0.0096 - 0.0102i$	22.6140	0.0730	0.0118
$-0.1037 - 1.4171i$	$0.0000 + 0.0000i$	$0.0096 + 0.0102i$	22.6140	0.0730	0.0118
$-0.5122 + 2.7760i$	$-0.0001 - 0.0000i$	$0.0078 + 0.0067i$	44.9279	0.1814	0.0266
$-0.5122 - 2.7760i$	$-0.0001 + 0.0000i$	$0.0078 - 0.0067i$	44.9279	0.1814	0.0266
$-0.1921 + 3.2798i$	$0.0000 - 0.0000i$	$0.0009 + 0.0003i$	52.2894	0.0585	0.0037
$-0.1921 - 3.2798i$	$0.0000 + 0.0000i$	$0.0009 - 0.0003i$	52.2894	0.0585	0.0037
$-0.3411 + 7.8002i$	$0.0000 - 0.0000i$	$-0.0002 + 0.0081i$	124.2621	0.0437	0.2467
$-0.3411 - 7.8002i$	$0.0000 + 0.0000i$	$-0.0002 - 0.0081i$	124.2621	0.0437	0.2467

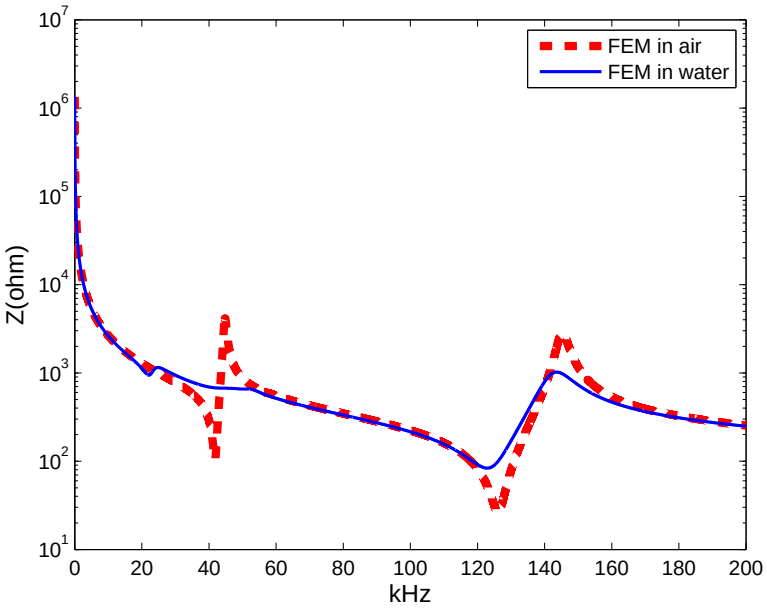

Figure 4.12. Impedance function comparison of the transducer: in air (FEM) v.s. in water (FEM)

For this transducer, water is surrounding not only outside the transducer but also inside the tube, which is called free flooded ring transducer. In order to figure out the influence of two parts of water to the transducer, one additional FE model is carried out, in which the water inside the tube is replaced by air. The model setup is the same with shown in Fig. 4.10 except that the water at the left bottom corner (inside the cylinder) is changed to air with density 1.11 kg/m^3 and bulk modulus 0.134 MPa. Shown in Table 4.7 are the signal decomposition outcomes of input voltage and output charge signals. With the modal frequencies of the transducer in water $f_{rw} = \{36.1098,\ 54.3060,\ 122.5889\}$ kHz (in column 4 of Table 4.7) and in air $f_{ra} = \{41.8696,\ 57.4214,\ 126.2812\}$ kHz (in column 4 of Table 4.5), the radiation mass can be calculated by Eq. 4.7 as $M_r = \{0.0058,\ 0.0020,\ 0.0010\}$ kg, where $M = \rho_{pzt}\pi(D_o^2 - D_i^2)L/4 + \rho_{poly}V_{poly} = 0.0167$ kg. As expected, the outcomes shows that the water adds more radiation mass on radial mode than the other two because of the larger interaction area with the fluid.

Notice that there are one additional pair of poles extracted besides those three structure modes in column 4 of Table 4.6. This is the so-called Helmholtz frequency caused by the resonance of water column flooded in the tube. The comparison between the modal frequencies in columns 4 of Table 4.6 and Table 4.7 indicates that the inside water column is equivalent to adding stiffness to the system, while the comparison with modal frequencies of the transducer in air yield that the outside water is to add mass to the transducer. According to reference (McMahon, 1964), the Helmholtz frequency of a cylinder with water column inside can be calculated as 31.133 kHz. After adding mass to the transducer by the outside water, this frequency will be reduced. The additional mode, 22.6140 kHz, in Table 4.6 should be the Helmholtz mode. In addition, column 5 of Table 4.6 shows that there is extra damping in water, which is also caused by the fluid-structure interaction but beyond the scope of this article.

Observing Table 4.6 and Fig. 4.12, one can notice that the radial mode, 44.9279 kHz mode, is very hard to be read from impedance plot using traditional method because the damping of this mode is too large to generate obvious valley and peak in the plot. But, this mode can be effectively extracted by the pole-residue method and the modal frequency can exactly calculated from the system poles.

Table 4.7. FEM signal decomposition results of the transducer in water (with air filled in the tube)

poles ν $\times 10^5$ (1)	input residues λ (2)	output residues γ $\times 10^{-8}$ (3)	modal frequencies kHz (4)	damping (5)	$\lvert\gamma/\tilde{V}(\nu)\rvert$ $\times 10^{-3}$ (6)
$0.0000 + 1.8849i$	$0.0189 - 0.4995i$	$-0.0191 - 0.1812i$	29.9999	$--$	$--$
$0.0000 - 1.8849i$	$0.0189 + 0.4995i$	$-0.0191 + 0.1812i$	29.9999	$--$	$--$
$-0.3211 + 2.2460i$	$-0.0001 - 0.0001i$	$0.0246 + 0.0408i$	36.1098	0.1415	0.0509
$-0.3211 - 2.2460i$	$-0.0001 + 0.0001i$	$0.0246 - 0.0408i$	36.1098	0.1415	0.0509
$-0.0054 + 3.4121i$	$-0.0000 - 0.0000i$	$0.0000 + 0.0001i$	54.3060	0.0016	0.0004
$-0.0054 - 3.4121i$	$-0.0000 + 0.0000i$	$0.0000 - 0.0001i$	54.3060	0.0016	0.0004
$-0.2884 + 7.6971i$	$0.0000 - 0.0000i$	$-0.0012 + 0.0086i$	122.5889	0.0374	0.2559
$-0.2884 - 7.6971i$	$0.0000 + 0.0000i$	$-0.0012 - 0.0086i$	122.5889	0.0374	0.2559

4.5.5 Impedance function in water from experiment

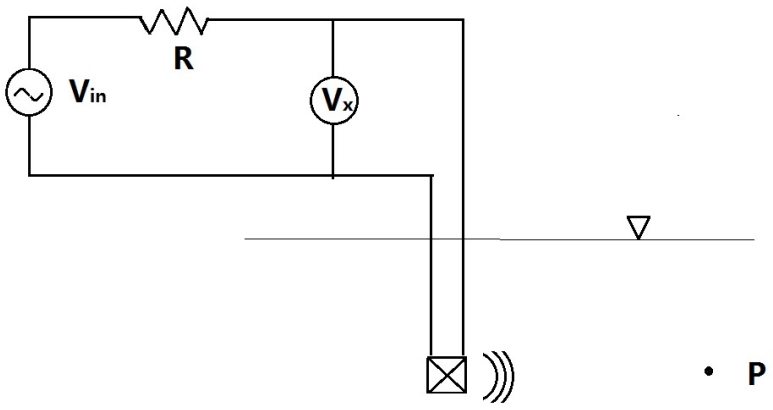

Figure 4.13. Experiment setup circuit in water

The setup of measuring the transducer in water is shown in Fig. 4.13, in which the same resistor and input signal $V_{in} = 10\exp(-10000t)$ as in air are used. V_x is the response voltage across the piezoelectric transducer (shown in Fig. 4.14). The total time duration is 100 μs long with time increment 0.1 μs.

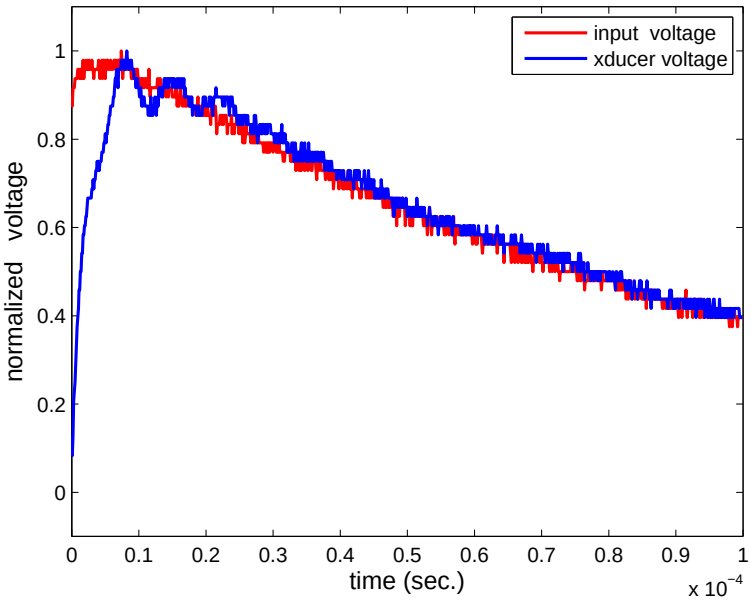

Figure 4.14. Normalized experimental input voltage and voltage across the transducer (xducer voltage) in water: input voltage scale 9.6000 V, xducer voltage scale 9.6000 V

Shown in Table 4.8 are the decomposition outcomes of V_{in} and V_x, and Fig. 4.15 displays the impedance function comparison between FEM and experiment when the transducer is operated in water. The impedance functions obtained from FE model and experiment match very well with each other except some small discrepancy at the longitudinal mode, and the FE model has well captured the characteristics of the transducer.

Table 4.8. Experimental signal decomposition results of the transducer in water

poles $\times 10^7$ (1)	input residues (2)	output residues (3)	modal frequencies kHz (4)
$-0.0998 + 0.0000i$	$10.1092 - 0.0000i$	$10.3675 - 0.0000i$	$--$
$-3.7963 + 0.0000i$	$-1.7357 + 0.0000i$	$-10.8814 + 0.0000i$	$--$
$-0.1541 + 1.5892i$	$0.0164 + 0.0178i$	$0.0296 + 0.0840i$	25.4123
$-0.1541 - 1.5892i$	$0.0164 - 0.0178i$	$0.0296 - 0.0840i$	25.4123
$-0.5247 + 2.9250i$	$0.0435 + 0.0152i$	$0.1618 - 0.0685i$	47.2957
$-0.5247 - 2.9250i$	$0.0435 - 0.0152i$	$0.1618 + 0.0685i$	47.2957
$-0.7462 + 8.6881i$	$0.0675 - 0.0511i$	$0.3599 - 0.3300i$	138.7844
$-0.7462 - 8.6881i$	$0.0675 + 0.0511i$	$0.3599 + 0.3300i$	138.7844

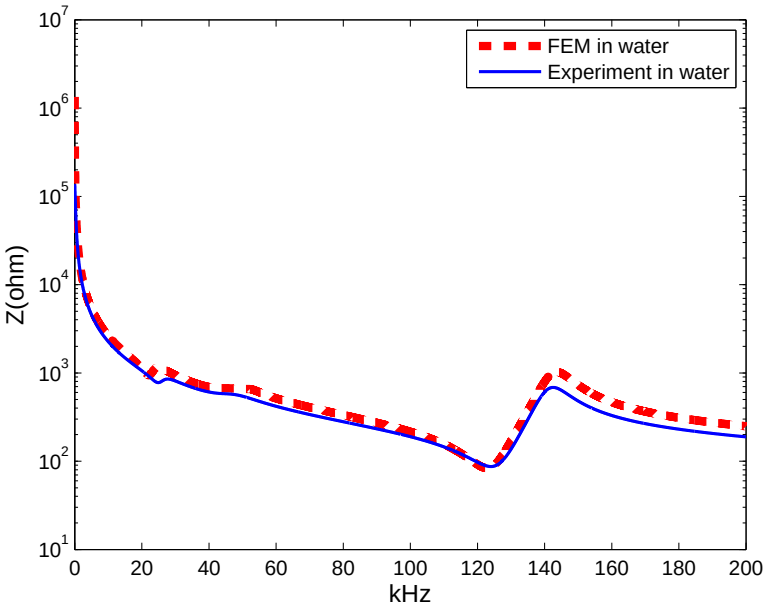

Figure 4.15. Impedance function comparison of the transducer in water: FEM v.s. experiment

4.6 Concluding Remarks

Impedance functions of a piezoelectric transducer are used to study the influence of surrounding water to the system. In this study, the pole-residue method are employed to estimate the impedance functions, by which the modal frequencies and modal damping can be exactly computed from the system poles. It shows that the ambient water adds both radiating mass and additional damping to the transducer. The radiation mass of each mode can be obtained by the resonant frequencies of the transducer in air and in water. For the free flooded transducer, the inner water column is equivalent to add stiffness to the system while the outside water is to add mass to the transducer. In addition, pole-residue method is more efficient for measuring the characteristics of the transducers. For the tube transducer in this study, the radial mode is hard to be read on the impedance plot in traditional way while it can be exactly extracted by the pole-residue method.

Chapter 5

"Impedance Function Comparison of Acoustic Transducers in Air and in Water by Pole-Residue Operations"

by

Bin Gao[1], Sau-Lon James Hu[2] and Harold T. Vincent[3]

will be submitted to *Journal of the Acoustical Society of America*

---

[1] PhD Candidate, Department of Ocean Engineering, University of Rhode Island, Narragansett, RI 02882. E-mail: gaobinouc@gmail.com

[2] Professor, Department of Ocean Engineering, University of Rhode Island, Narragansett, RI 02882. E-mail: jameshu@uri.edu

[3] Research Professor, Department of Ocean Engineering, University of Rhode Island, Narragansett, RI 02882. E-mail: vincentht@uri.edu

CHAPTER 5

Manuscript 3: Estimating TVR and Beam Pattern of Underwater Transducers by Pole-Residue Operations

5.1 Abstract

Transmitting voltage response (TVR) and beam pattern (BP) are two of the most important measures of a transducer's ability to perform the functions of radiating sound. Traditionally, there are two kinds of methods for measuring TVR and BP, namely, single-frequency harmonic analysis method and Fourier-based analysis method. But, both methods have drawbacks. The former one is too time-consuming while the latter one suffers from the leakage and frequency resolution problems. Additionally, both of them are usually influenced by the reflecting waves from boundaries, such as water surface and acoustic tank walls. In this article, a new approach by pole-residue operations is developed to estimate TVR and BP, which overcomes the above drawbacks. Unlike the traditional methods, continuous characteristic functions in the frequency domain can be obtained by one-time measurement with the new method. Since very short signal is needed in this approach, the calculation of characteristic functions can be finished before the sound waves travel back from the boundaries. Two numerical examples are provided to show the procedures to compute TVR and BP of an underwater transducer. The effectiveness is verified by the harmonic analysis method. The accuracy and the efficiency are also demonstrated by the comparisons with traditional methods.

5.2 Introduction

An electroacoustic transducer is usually used to transmit sound into a medium or to detect sound from the medium. The transmitting response and radiating beam pattern are measures of a transducer's ability to perform these functions.

TVR is the far field pressure produced on its maximum response axis and BP is the spacing transmitting pattern operated at one fixed frequency. Accurately and efficiently estimating these characteristics becomes significant for applications of acoustic transducers.

Measurements of these functions are usually carried out at one single frequency or over a range of frequencies of interest in the frequency domain. Generally, there are two types of traditional methods for measuring the above characteristic functions, i.e., single-frequency harmonic analysis method and Fourier-based analysis method. The single-frequency harmonic analysis is to repeatedly apply a harmonic input signal to get the corresponding steady state response of the given frequency, and is generally considered to be an accurate way to obtain frequency response function (FRF). The Fourier method computes characteristic functions through the application of the fast Fourier transform (FFT) of both input and output signals, and is considered to be an efficient way on estimating FRF. Both methods have drawbacks though. The single-frequency harmonic analysis method is time costly especially when very high frequency resolution is required; and the Fourier-based analysis method is always affected by the periodic assumption and time interval resolution for signals, and suffers from the leakage problem and frequency resolution issue. In addition, the pressure signals are usually contaminated by the reflected waves from boundaries when measured in acoustic tank with traditional methods.

A new approach for estimating characteristic functions of underwater transducers, such as TVR and BP, by pole-residue operations is developed in this article. Unlike the traditional methods, this new method can calculate the system functions as a continuous function without periodic assumption. With the advantages of the new method, one can efficiently obtain the TVR and BP by a one-time

measurement instead of repeating many times.

This paper will provide two numerical examples to verify the correctness and demonstrate the effectiveness of the newly developed method by pole-residue operations. To illustrate the procedures of the new approach, the first study shows how to implement it to compute TVR numerically. The second one presents the calculation of multiple beam patterns using only one single input at a time with the new method.

5.3 Preliminaries

This section reviews the mathematics of importance to this article, including signal decomposition using Prony-SS method, the governing differential equation of underwater projectors, the transmitting voltage response function, and beam pattern.

5.3.1 Pole-residue form of a signal

An arbitrary signal $f(t)$ can always be decomposed into a finite number of exponential components

$$f(t) = \sum_{\ell=1}^{L} \alpha_\ell \exp(\lambda_\ell t) \qquad 0 \leq t < T \tag{5.1}$$

where L is the number of terms, α_ℓ and λ_ℓ are constants.

After the signal decomposition of Eq. 4.3 has been done, the Laplace transform of Eq. 4.3 yields the following pole-residue form in the Laplace-domain

$$\tilde{f}(s) = \sum_{\ell=1}^{L} \frac{\alpha_\ell}{s - \lambda_\ell} \tag{5.2}$$

where all the λ_ℓ and α_ℓ $\ell = 1, \ldots, L$ are the poles and residues of this signal. This decomposition can be done by the Prony-SS method (Hu et al., 2013; Hu et al., 2016).

5.3.2 Acoustic pressure field

The key of acoustic problems is to solve the acoustic field that generated by a vibration surface. The acoustic pressure, $p(\vec{x}, t)$, is a scalar quantity and usually defined as the variation pressure from the static pressure. The governing differential equation for the acoustic pressure is

$$\nabla^2 p - \frac{1}{c^2}\frac{\partial^2 p}{\partial t^2} = 0 \tag{5.3}$$

where ∇^2 is the Laplace operator and c is the speed of sound.

5.3.3 TVR of underwater projectors

The transmitting voltage response is one of the most important measurements for the acoustic performance of a projector. Oftentimes it is measured in the direction of the maximum response axis at a radial distance in the far field. It is usually defined as the pressure per unit electrical excitation referenced to 1 meter and a pressure of $p_0 = 1$ μPa in underwater applications as (Sherman and Butler, 2007)

$$\text{TVR} = 20\log_{10}|p/p_0| \qquad \text{re 1 volt @ 1 m} \tag{5.4}$$

where p is the pressure at 1 m generated by 1 volt input signal. Thus, if the transducer is excited by a voltage v_0 and the pressure p_r collected at distance r, Eq. 5.4 becomes

$$\text{TVR} = 20\log_{10}\left|\frac{p_r/(1/r)}{v_0 p_0}\right| = 20\log_{10}|r p_r/v_0| + 120 \quad \text{dB//}\mu\text{Pa @ 1m/V} \tag{5.5}$$

5.3.4 BP of underwater projectors

Acoustic pressure field is a scalar field with respect to the distance r and the angle θ. Therefore, one can separate the far field pressure amplitude $p(r, \theta)$ into two parts, one only associated with r and another one only with the direction θ. The acoustic pressure amplitude in the far field can be written as (Kinsler et al., 2000)

$$p(r, \theta) = p_{ax}(r)g(\theta) \tag{5.6}$$

where p_{ax} and $g(\theta)$ are far field axial pressure and directional factor, respectively. The axial pressure is proportional to $1/r$ in the far field. The variation of sound pressure level with angle is the beam pattern

$$BP(\theta) = 20 \log_{10} g(\theta) \tag{5.7}$$

which usually refers to some specific frequency.

Traditionally, beam patterns can be measured by rotating the directional hydrophone under test in the time domain (Sherman and Butler, 2007). At fixed frequency f_0, the transducer is driven by a sinusoidal voltage with amplitude V_0 and one can obtain the pressure amplitude $p(\theta)$ or scaled one $g(\theta)$ when it reaches steady state. By rotating the transducer to all desired angles and repeating the above procedures, the total directional factor $g(\theta)$ could be acquired. Finally, substituting normalizing $g(\theta)$ into Eq. 5.7, the beam pattern can be plotted in a polar coordinate.

5.4 Pole-Residue Operations of Estimating TVR Function and BP

5.4.1 Pole-residue method

The generalized expression for the displacement response at coordinate j to the load at k can be written by the following convolution integral

$$u_{jk}(t) = \int_0^t h_{jk}(t-\tau)\, p_k(\tau)\, d\tau \tag{5.8}$$

where $h_{jk}(t)$ is the unit impulse response function associated with coordinates j and k. Applying Laplace transform to Eq. 5.8, one can get the displacement response in the Laplace-domain

$$\tilde{u}_{jk}(s) = \tilde{h}_{jk}(s)\tilde{p}_k(s) \tag{5.9}$$

According to Eq. 4.4 and the reference (Hu et al., 2016), the external force $\tilde{p}_k(s)$ and the transfer function (TF) $\tilde{h}_{jk}(s)$ of an N-DOF system can be written

as

$$\tilde{p}_k(s) = \sum_{\ell=1}^{L} \frac{\alpha_\ell}{s - \lambda_\ell} \tag{5.10}$$

and

$$\tilde{h}_{jk}(s) = \sum_{n=1}^{2N} \frac{\beta_n}{s - \mu_n} \tag{5.11}$$

where the subscripts j and k of the residues of $\tilde{p}_k(s)$ and $\tilde{h}_{jk}(s)$ are omitted for the simplification of notations.

Substituting Eqs. 5.10 and 5.11 into Eq. 5.9, it yields

$$\tilde{u}_{jk}(s) = \left(\sum_{n=1}^{2N} \frac{\beta_n}{s - \mu_n} \right) \left(\sum_{\ell=1}^{L} \frac{\alpha_\ell}{s - \lambda_\ell} \right) \tag{5.12}$$

Eq. 5.12 can be rewritten in the pole-residue form

$$\tilde{u}_{jk}(s) = \sum_{m=1}^{L+2N} \frac{\gamma_m}{s - \nu_m} \tag{5.13}$$

Comparing Eq. 5.12 and Eq. 5.13, one can notice that the total $L + 2N$ response poles ν_m are originally from the L excitation poles and $2N$ system poles. Arrange the first L poles as the excitation poles, i.e., $\nu_m = \lambda_m$, $m = 1, \cdots, L$, and the last $2N$ poles as the system poles, i.e., $\nu_{m+L} = \mu_m$, $m = 1, \cdots, 2N$. For each response pole ν_m, the corresponding residue can be computed by (Hu et al., 2016)

$$\gamma_m = \lim_{s \to \nu_m} (s - \nu_m) \tilde{u}_{jk}(s) = \lim_{s \to \nu_m} (s - \nu_m) \tilde{p}_k(s) \tilde{h}_{jk}(s) \tag{5.14}$$

Thus, from Eq. 5.14, the residues corresponding to the first L response poles (at the excitation poles) are

$$\gamma_m = \lim_{s \to \nu_m} (s - \nu_m) \left(\sum_{l=1}^{L} \frac{\alpha_\ell}{s - \lambda_\ell} \right) \tilde{h}_{jk}(s) = \alpha_m \, \tilde{h}_{jk}(\lambda_m), \qquad m = 1, \cdots, L \tag{5.15}$$

and the residues corresponding to the last $2N$ response poles (at the system poles) are

$$\gamma_{m+L} = \lim_{s \to \nu_{m+L}} (s - \nu_{m+L}) \, \tilde{p}_k(s) \left(\sum_{n=1}^{2N} \frac{\beta_n}{s - \mu_n} \right) = \beta_m \, \tilde{p}_k(\mu_m), \qquad m = 1, \cdots, 2N \tag{5.16}$$

Eqs. 5.15 and 5.16 indicate that all residues of the response can be easily obtained from simple operations of the poles and residues of the excitation and system transfer function. Generally, this pole-residue method can be applied to the response calculation to arbitrary loading for a linear multi-DOF system, not only limited to compute the displacement response due to external force.

5.4.2 pole-residue operations for computing system functions

Shown in Table 5.1 are the decomposition outcomes of input and output signals by multi-signal Prony-SS method, i.e., global poles, input residues, and output residues. One can distinguish the input poles and system poles by observing the columns 1 and 2 in Table 5.1. In column 2, the input residues can be divided two groups, nonzero ones α_ℓ and zero or negligibly small ones. In column 1, the global poles are correspondingly divided into two groups, ν_ℓ and ν_{n+L}. The input poles are the ones ν_ℓ in the group of nonzero input residues while the system poles μ_n are the remaining ones ν_{n+L} in the group of zero or negligibly small input residues (Cao et al., 2017), which can also be interpreted that the system poles are simply the output poles ν minus the input poles ν_ℓ. With the system poles, one can accurately calculate the modal frequencies and modal damping of the system by

$$\omega_n = |\nu_{n+L}|, \quad \xi_n = \frac{-\mathrm{Re}(\nu_{n+L})}{|\nu_{n+L}|} \tag{5.17}$$

Eq. 5.9 shows the relationship among input, system and output in the Laplace domain for a system initially at rest. Thus, one can simply calculate the transfer function by

$$\tilde{h}_{jk}(s) = \frac{\tilde{u}_{jk}(s)}{\tilde{p}_k(s)} \tag{5.18}$$

From Eqs. 5.10 and 5.13, one obtains

$$\tilde{p}_k(s) = \sum_{\ell=1}^{L} \frac{\alpha_\ell}{s - \nu_\ell} \tag{5.19}$$

$$\tilde{u}_{jk}(s) = \sum_{m=1}^{2N+L} \frac{\gamma_m}{s - \nu_m} \tag{5.20}$$

Notice that $\tilde{p}_k(s)$ and $\tilde{u}_{jk}(s)$ can be expressed by the global poles ν, input residues α and output residues γ.

Combining Eqs. 5.18 to 5.20, it yields the transfer function

$$\tilde{h}_{jk}(s) = \left(\sum_{m=1}^{2N+L} \frac{\gamma_m}{s - \nu_m} \right) / \left(\sum_{\ell=1}^{L} \frac{\alpha_\ell}{s - \nu_\ell} \right) \tag{5.21}$$

Table 5.1. Summary of operations for calculating the system functions $\tilde{h}_{jk}(s)$

global poles	input residues	output residues
ν_ℓ $\ell = 1, \cdots, L$	α_ℓ $\ell = 1, \cdots, L$	γ_ℓ $\ell = 1, \cdots, L$
ν_{n+L} $n = 1, \cdots, 2N$	0	γ_{n+L} $n = 1, \cdots, 2N$

5.4.3 Estimating TVR by pole-residue operations

Start from the input voltage signal $v(t)$ to a transducer and the measured acoustic pressure signal $p_r(t)$ at some distance r away from it along some direction, say radial direction. Applying Prony-SS method to process these two signals simultaneously, one can obtain $\tilde{v}(s)$ and $\tilde{p}_r(s)$ in the pole-residue form. With the proposed method, the transfer function $\tilde{h}_{pv}(s)$ from voltage to pressure can be computed by pole-residue operations. Thus, TVR can be calculated through Eq. 5.5

$$TVR(s) = 20 \log_{10} \left| \frac{\tilde{p}_r(s)}{(1/r)\tilde{v}(s)p_0} \right| = 20 \log_{10} |r\tilde{h}_{pv}(s)| + 120 \tag{5.22}$$

Substituting s by $i\omega$, TVR in Eq. 5.22 becomes a continuous function in the frequency domain. Furthermore, this function could be reflection-free because

the Prony-SS method only needs very short signal and the decomposition is done before reflective waves travel back.

5.4.4 Estimating BP by pole-residue operations

Let $v(t)$ be the input voltage and $p_r(t, \theta_i)$ the pressure field at distance r, where θ_i $(i = 1, \ldots, N)$ is the angle position in the polar coordinate. Multi-signal Prony-SS method yields the signal decompositions $\tilde{v}(s)$ and $\tilde{p}_r(s, \theta_i)$, and the transfer functions $\tilde{h}_i(s)$ can be computed by the operations of those poles and residues respectively. To have the BP, let $\theta_1 = 0$ and $\theta_N = 2\pi$. Therefore, one can obtain the transfer function matrix $\tilde{\mathbf{h}}(s) = [\tilde{h}_1(s), \ldots, \tilde{h}_N(s)]$. Substituting s by $i\omega$, one has

$$\mathbf{H}(\omega) = [H_1(\omega), \ldots, H_N(\omega)] \tag{5.23}$$

Every transfer function in Eq. 5.23 is a continuous function in frequency domain. Therefore, one can compute the BP at any frequency f_0 by the follow expression

$$BP(f_0) = [|H_1(f_0)|, \ldots, |H_N(f_0)|] \tag{5.24}$$

The resolution along the direction of θ depends on the available data of acoustic field $p_r(t, \theta_i)$.

5.5 Numerical Studies

Two numerical studies are carried out to show the procedures of proposed method to compute TVR and BP. All calculation are based on the pressures field data from FE model. The system considered here consists of a piezoelectric transducer and the surrounding water domain. In the FE model, the cylindrical transducer is placed in the center of a spherical water domain in Abaqus. Shown in Fig. 5.1 is one quarter cross section of the sphere. To focus on the method development and simplify the problem, the thin waterproof layer is omitted at this time.

The transducer used in this article is radially polarized and made of a piezoelectric material PZT4 (STEMiNC) with dimensions $13mm \times 26mm \times 22mm$ ($L \times OD \times ID$). The piezoelectric transducer is electroded on both the inner and outer surfaces. The material properties for PZT4 in a cylindrical system are:

Elasticity (stiffness) matrix $\mathbf{c}^E$:

$$\begin{bmatrix} 132.64 & 76.92 & 76.92 & 0 & 0 & 0 \\ 76.92 & 134.68 & 63.76 & 0 & 0 & 0 \\ 76.92 & 63.76 & 134.68 & 0 & 0 & 0 \\ 0 & 0 & 0 & 25.64 & 0 & 0 \\ 0 & 0 & 0 & 0 & 25.64 & 0 \\ 0 & 0 & 0 & 0 & 0 & 35.46 \end{bmatrix} \text{GPa}$$

Piezoelectric coupling matrix (stress coefficients $\mathbf{e}$):

$$\begin{bmatrix} 20.9048 & -3.1669 & -3.1669 & 0 & 0 & 0 \\ 0 & 0 & 0 & 12.7179 & 0 & 0 \\ 0 & 0 & 0 & 0 & 12.7191 & 0 \end{bmatrix} \text{coulomb/m}^2$$

Dielectric matrix with constant strain $\boldsymbol{\varepsilon}^{\boldsymbol{S}}$

$$\begin{bmatrix} 4.819 & 0 & 0 \\ 0 & 6.752 & 0 \\ 0 & 0 & 6.752 \end{bmatrix} \times 10^{-9}\text{F/m}$$

The 1-, 2- and 3-direction are radial, tangential, and axial, respectively. The poling direction is radially outwards from the axis of symmetry. The mass density is 7900 kg/m^3. The transducer is modeled as an axisymmetric structure utilizing 8-node axisymmetric elements (CAX8E) in Abaqus.

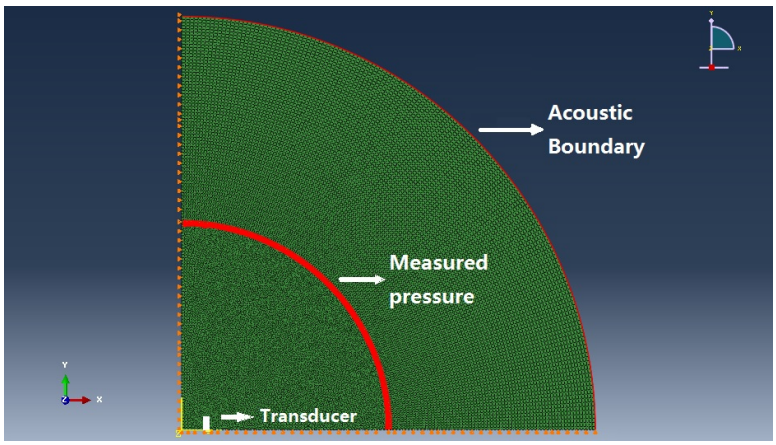

Figure 5.1. The sketch of FEM setup for the transducer in water

Linear 4-node axisymmetric acoustic elements (ACAX4) are used to simulate the spherical water domain with radius 0.2 m and mesh size 1.5×10^{-3} m. The acoustic water are defined by density 1000 kg/m^3 and bulk modulus 2.1404 GPa. The surface-based tie constraint is used to couple the structure with the surrounding water. Surfaces are defined at the outside of the transducer and at the free surface of the water. To consider the symmetric property, all points of the bottom and the left boundary for both water and the transducer are constrained no move along longitudinal and radial directions, respectively. A nonreflecting boundary condition is applied at the water boundary to absorb the acoustic waves (shown in Fig. 5.1).

A sinusoidal electrical potential signal of 10 volts with the frequency 30 kHz is applied using an electrical boundary condition. The pressure response of the system is calculated by implicit dynamic analysis. The acoustic pressure signals is collected at the distance of 0.1 m away from the center of the transducer.

Fig. 5.2 shows the input voltage and the output acoustic pressure signals. The total time duration of the simulation is 600 μs with time increment 0.5 μs. Since the pressure is collected at 0.1 m away from the center, time of arrival for acoustic waves will be $(0.1 - 0.013)/1463 \approx 60$ μs. Given the water boundary located at 0.2 m, first reflection waves travel back in $(0.1 - 0.013 + 0.2)/1463 \approx 196$ μs if any.

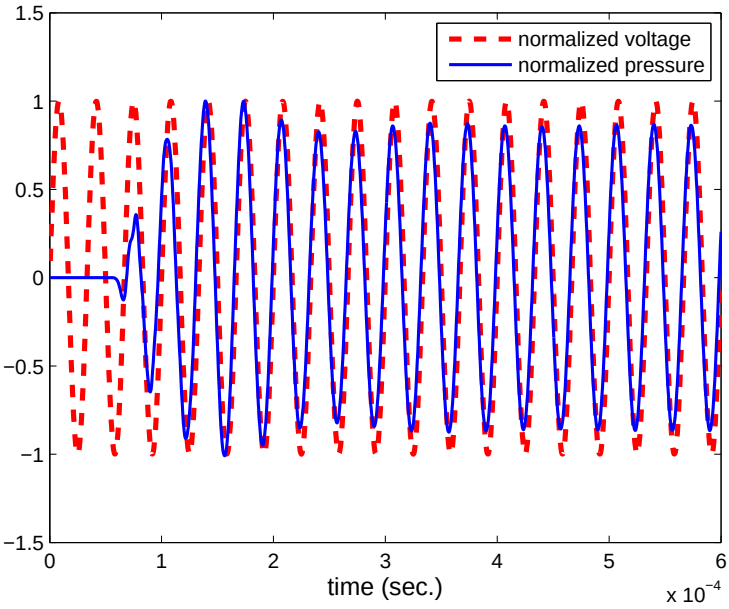

Figure 5.2. Normalized input voltage and output pressure (radial direction at 0.1 m) signals: input voltage scale 10 V, output pressure scale 708.0390 Pa

5.5.1 Estimating TVR

Shown in Table 5.2, the voltage and pressure signals with time duration 180 μs are decomposed into pole-residue form using multi-signal Prony-SS method. Column 1 through 3 of Table 5.2 are the global poles, voltage (input) residues, and pressure (output) residues, respectively. By observing the values of Column 2, one can figure out the first two poles are input poles because all other values are negligibly small, saying less than 0.1% of the first two. Thus, the others in Column 1 are system poles. Column 4 shows the modal frequencies of the components under 150 kHz obtained from the absolute value of system poles. Note that poles and residues of input and output signals are available, together with Eqs. 5.21 and 5.22, one can obtain the TVR function numerically with any frequency resolution.

Table 5.2. Signal decomposition for input voltage and output acoustic pressure

poles $\times 10^5$	voltage residues	pressure residues $\times 10^2$ Pa	frequency kHz	normalized $\lvert\gamma/\tilde{V}(\mu)\rvert$
$-0.0000 + 1.8849i$	$0.4713 - 4.9791i$	$-2.5631 - 1.8515i$	29.9998	$--$
$-0.0000 - 1.8849i$	$0.4713 + 4.9791i$	$-2.5631 + 1.8515i$	29.9998	$--$
$-0.1184 + 1.5549i$	$-0.0011 - 0.0002i$	$0.9063 + 1.6341i$	24.8188	0.2421
$-0.1184 - 1.5549i$	$-0.0011 + 0.0002i$	$0.9063 - 1.6341i$	24.8188	0.2421
$-1.9708 + 0.0000i$	$-0.0060 + 0.0000i$	$-0.5964 + 0.0000i$	$--$	0.5270
$-0.5625 + 2.8882i$	$0.0013 - 0.0007i$	$1.6523 - 0.1606i$	46.8301	1.0000
$-0.5625 - 2.8882i$	$0.0013 + 0.0007i$	$1.6523 + 0.1606i$	46.8301	1.0000
$-0.0010 + 3.4736i$	$-0.0000 + 0.0001i$	$-0.0100 - 0.0072i$	55.2840	0.0111
$-0.0010 - 3.4736i$	$-0.0000 - 0.0001i$	$-0.0100 + 0.0072i$	55.2840	0.0111
$-0.2892 + 5.6168i$	$-0.0000 - 0.0002i$	$0.0690 - 0.0209i$	89.5126	0.2117
$-0.2892 - 5.6168i$	$-0.0000 + 0.0002i$	$0.0690 + 0.0209i$	89.5126	0.2117
$-0.7445 + 6.8566i$	$0.0001 - 0.0006i$	$0.0716 - 0.0788i$	109.7673	0.4918
$-0.7445 - 6.8566i$	$0.0001 + 0.0006i$	$0.0716 + 0.0788i$	109.7673	0.4918
$-0.0439 + 7.5168i$	$0.0000 - 0.0000i$	$0.0013 - 0.0011i$	119.6364	0.0089
$-0.0439 - 7.5168i$	$0.0000 + 0.0000i$	$0.0013 + 0.0011i$	119.6364	0.0089
$-0.1183 + 7.9534i$	$0.0001 - 0.0000i$	$0.0467 - 0.1381i$	126.5961	0.8704
$-0.1183 - 7.9534i$	$0.0001 + 0.0000i$	$0.0467 + 0.1381i$	126.5961	0.8704
$-0.1664 + 9.1139i$	$-0.0001 - 0.0000i$	$0.0307 - 0.0638i$	145.0767	0.5520
$-0.1664 - 9.1139i$	$-0.0001 + 0.0000i$	$0.0307 + 0.0638i$	145.0767	0.5520

Plotted in Fig. 5.3 is the TVR function on radial axis. The peaks in the plot are corresponding to the resonant frequencies of the whole system. Some of them are from the resonance of the transducer while others are caused by the water column inside the tube. According to the former study, the components with frequencies 46.8301 kHz, 55.2840 kHz and 126.5961 kHz are the radial, bending and longitudinal modes of the transducer, respectively. Values in column 6 of Table 5.2 represent the relative amplitudes of the corresponding components in forming the system functions. Therefore, the radial mode (largest value in column 6) and the longitudinal mode (second largest value) are two dominant transmitting modes of the transducer. In addition, Helmholtz mode, the first mode of water column (24.8188 kHz), is also concerned in this study.

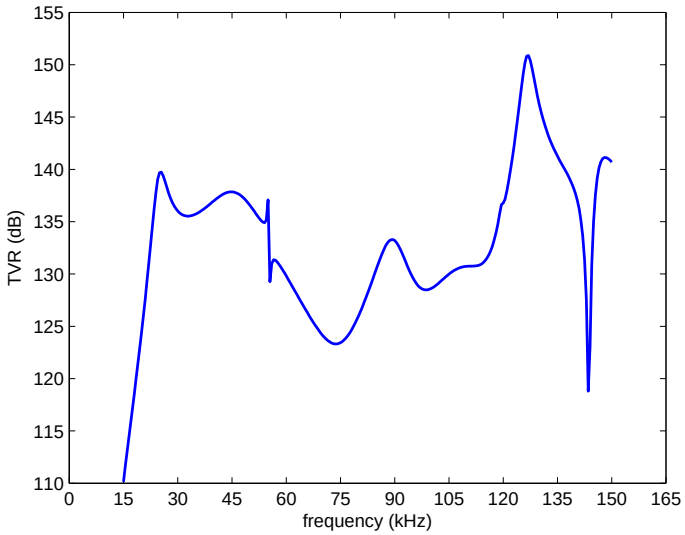

Figure 5.3. TVR on radial axis computed by pole-residue operations

Fig. 5.4 is the TVR comparison between the proposed method and traditional single-frequency harmonic analysis method, which is usually considered to be accurate. As illustrated, there is no noticeable difference between the proposed method and the single-frequency method at the measured frequencies. In addition, one can hardly have as many points as possible on the TVR function with single-frequency method because the process of performing the repeated measurements is very time consuming. In contrast, the proposed method can obtain the function by a one-time measurement of the input voltage and output pressure signals. From this point of view, the proposed method is much more efficient than the single-frequency method.

Fig. 5.6 shows the TVR comparison between the proposed method and Fourier-based method. As shown in Fig. 5.5, a chirp signal, with duration 5 ms and time increment 1 μs, is used to excite the transducer when applying Fourier based method. After calculating the FRF $H_{pv}(\omega)$ by taking FFT of the input voltage and output pressure signals, together with Eq. 5.22, one can calculate the

TVR in the frequency domain. Shown in Fig. 5.6 indicates that the TVR from Fourier method is aliased after 75 kHz. Besides leakage and frequency resolution problems, it also suffers from the reflection waves because FFT requires long signal to guarantee the accuracy, during which the reflective waves travel back and forth for several times. In contrast, the proposed method uses only 180 μs before the reflective waves are back. In addition, only about 300 data points are used to calculate poles and residues, which makes it a computationally efficient way.

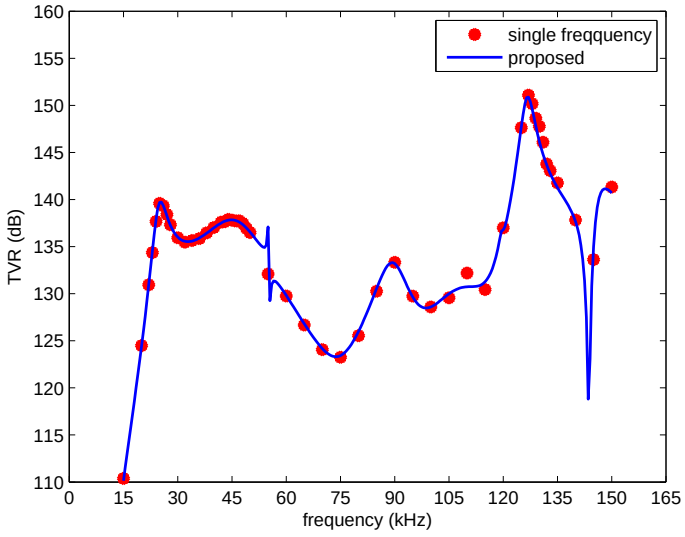

Figure 5.4. TVR comparison between traditional single-frequency harmonic analysis method and proposed method

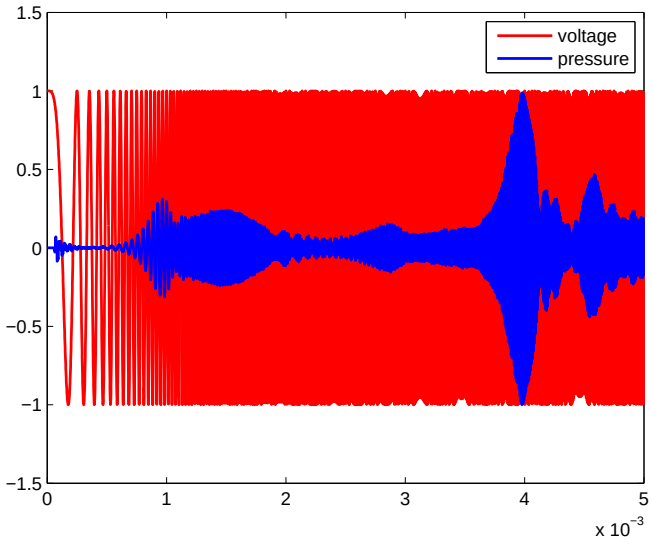

Figure 5.5. Normalized input voltage (chirp signal) and output pressure (radial direction at 0.1 m) signals: input voltage scale 10 V, output pressure scale 3.2453×10^3 Pa

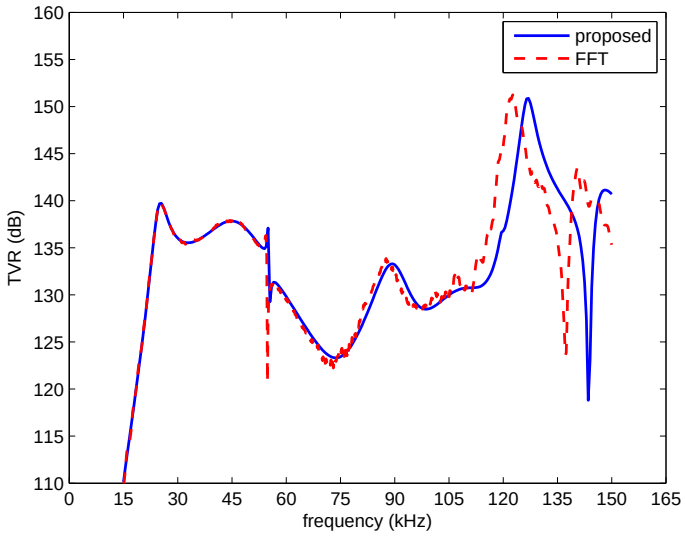

Figure 5.6. TVR comparison between proposed method and Fourier based method

5.5.2 Estimating BP

To obtain beam pattern, one needs to measure the pressure field $p(t, \theta)$ around the transducer. In this study, there are 158 points used to collect pressure data

along a 0.1 m arc from x-axis to y-axis (shown in Fig. 5.1). Thus, the angle θ distribution is from 0° to 90° with degree interval 0.5732°. Eq. 5.24 indicates that the remaining task is to compute the transfer functions at each angle θ.

By pole-residue operations, one can obtain the transfer functions for all angles. In fact, TVR is only one specific type of TF, which will be used to calculate the BP in the following presentation. Fig. 5.7 are some representative TVRs at four different angles. It shows that the three major modes, Helmholtz mode (25 kHz), radial mode (46 kHz) and longitudinal mode (127 kHz), always dominate the transmitting of acoustic pressure waves but their 'weights' are different at different angles. As illustrated in Fig. 5.7, the beam pattern can be treated as the collection of all the TVRs along a vertical line (one specific frequency) if they are plotted at all angles. Since there has been one quarter of the field, together with the symmetric geometry, one can have the BP for all surrounding angles. In this study, the BP are plotted in dB based on normalized TVRs/TFs.

Figs. 5.8, 5.9 and 5.10 are comparisons of beam patterns between traditional 'single-angle' harmonic analysis method, which is considered accurate, and proposed method at 25 kHz (Helmholtz), 46kHz (radial) and 127kHz (longitudinal), respectively. As expected, they all agree with each other pretty well. The Helmholtz mode and radial mode mainly transmit acoustic energy along radial direction while the longitudinal mode does that along axial direction. As far as the computational time is concerned, the proposed method is much more efficient than traditional method because one can obtain all beam patterns at any frequency from one single input other than repeating it many times with harmonic analysis method.

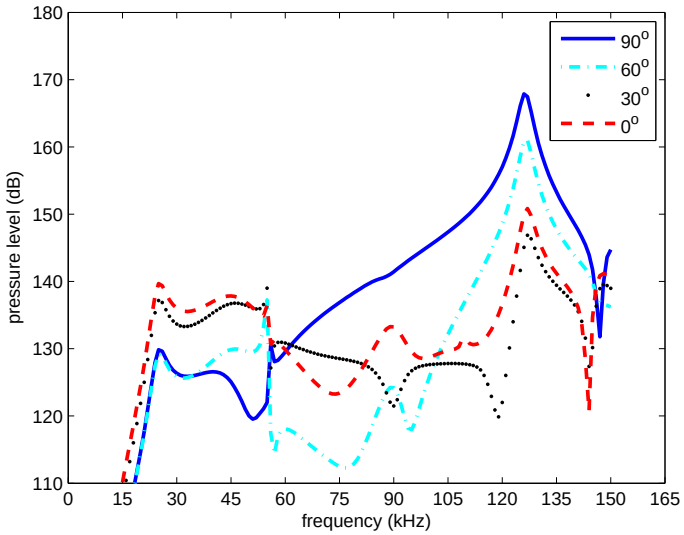

Figure 5.7. Transfer functions (TVRs) at four different angles around the transducer: 0° (x-axis), 30°, 60°, 90° (y-axis)

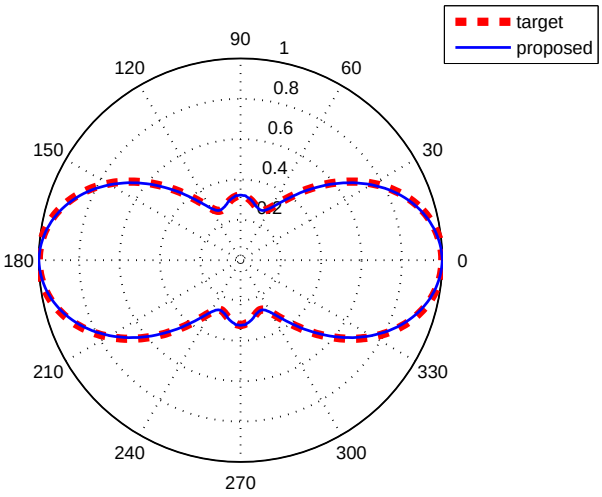

Figure 5.8. BP comparison between harmonic analysis method and proposed method at 25 kHz

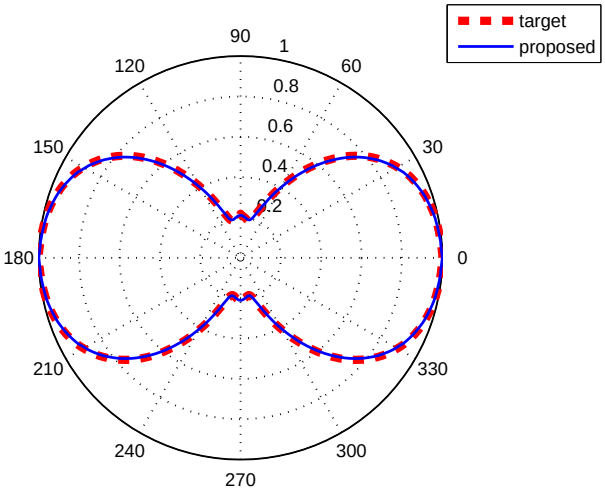

Figure 5.9. BP comparison between harmonic analysis method and proposed method at 46 kHz

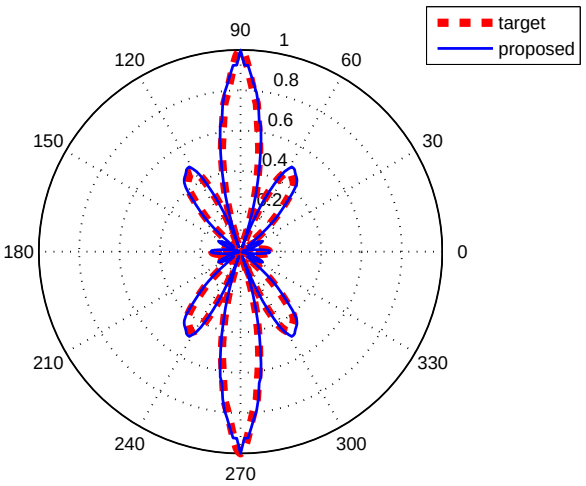

Figure 5.10. BP comparison between harmonic analysis method and proposed method at 127 kHz

5.6 Concluding Remarks

An efficient method to estimate characteristic functions of underwater transducers by pole-residue operations has been developed in this paper. The correctness of the new method has been verified by using a 'single-angle' harmonic analysis

method. In this article, a key development is on how to manipulate the poles and residues of input voltage and output pressure signals to calculate TVR and beam pattern. With the pole-residue method, TVR and BP can be computed by a one-time measurement as a continuous function in the frequency domain. The new method is proved to be much more efficient than the traditional single-frequency (for TVR) and single-angle (for BP) harmonic analysis method. Furthermore, it is also demonstrated in this paper that the new method can eliminate the influence of reflective waves by using a very short signal.

CHAPTER 6

Concluding Remarks

Characteristic functions, such as impedance function, TVR and beam pattern, are of great importance for acoustic transducers. To estimate them accurately and efficiently, a new approach by pole-residue operations is developed and implemented in this dissertation. In the proposed method, the global poles and corresponding residues associated with the input and output signals are first extracted with the multi-signal Prony-SS method. Therefore, one can calculate the transfer function by manipulating those poles and residues. In addition, by using this multi-signal method to process the input and output signals simultaneously, one can easily pick the system poles from the outcomes of signal decomposition, by which one can precisely calculate the modal frequencies and modal damping. Both computer simulations and lab experiments have been conducted to verify the correctness and accuracy of the proposed method on above characteristics of the underwater transducer.

Major findings and contributions are summarized as follows:

Frequency domain method for total response Deriving a closed-form solution for the transient and total responses of SDOF/MDOF systems to arbitrary periodic excitations is an analytical contribution of this article. It showed that the transient response could be obtained in a similar fashion as the steady-state response, but the roles of the system and excitation were reversed. Together with the FFT algorithm, a very efficient numerical method has been developed to compute the total response for MDOF systems, suitable for both damped and undamped systems. The paper demonstrated that the computational time needed for getting the transient response could

be much less than that for the steady state response. The correctness of the proposed method has been verified through three numerical examples by comparing the total responses obtained from the proposed method to those obtained from using a time domain method.

Improved method for impedance function Impedance functions of a piezoelectric transducer are used to study the influence of surrounding water to the system. In this study, the pole-residue method are employed to estimate the impedance functions, by which the modal frequencies and modal damping can be exactly computed from the system poles. It shows that the ambient water adds both radiating mass and additional damping to the transducer. The radiation mass of each mode can be obtained by the resonant frequencies of the transducer in air and in water. For the free flooded transducer, the inner water column is equivalent to add stiffness to the system while the outside water is to add mass to the transducer. In addition, pole-residue method is more efficient for measuring the characteristics of the transducers. For the tube transducer in this study, the radial mode is hard to be read on the impedance plot in traditional way while it can be exactly extracted by the pole-residue method.

Improved method for TVR and BP An efficient method to estimate characteristic functions of underwater transducers by pole-residue operations has been developed in this paper. The correctness of the new method has been verified by using a 'single-angle' harmonic analysis method. In this article, a key development is on how to manipulate the poles and residues of input voltage and output pressure signals to calculate TVR and beam pattern. With the pole-residue method, TVR and BP can be computed by a one-time measurement as a continuous function in the frequency domain. The

new method is proved to be much more efficient than the traditional single-frequency (for TVR) and single-angle (for BP) harmonic analysis method. Furthermore, it is also demonstrated in this paper that the new method can eliminate the influence of reflective waves by using a very short signal.

APPENDIX A

Fundamentals of Underwater Transducers

A transducer is a device that converts energy from one form to another. The transducer used in this study is an electroacoustic transducer, which converts electrical energy to acoustical energy, or vice versa. This kind of transducer can be operated in either transmitting or receiving mode. A transmitter can generate acoustic wave by applied electrical signal, which is called loudspeaker in air or projector in water. A receiver can generate electrical signal by incident acoustic wave, which is called microphone in air or hydrophone in water. The transducer used here is a projector.

The projector has the shape of a cylindrical tube and is made of piezoelectric material. The typical feature of this material is the piezoelectric effect, which is stated that a voltage will be generated over the piezoelectric material when mechanical stress is applied to it. Conversely, a mechanical strain will be caused by applying a voltage on the material, which is called inverse piezoelectric effect. One of the most popular piezoelectric material is lead zirconate titanate (PZT) and it usually displays a linear relationship between mechanical stress/strain and electric displacement/field by the strong piezoelectric effect.

Constitutive equations demonstrate the linear effect of piezoelectric material. The so-called e-form equations are stated as

$$\mathbf{T} = \mathbf{c}^E\mathbf{S} - \mathbf{e}^t\mathbf{E} \tag{A.1}$$

$$\mathbf{D} = \mathbf{e}\mathbf{S} + \boldsymbol{\varepsilon}^S\mathbf{E} \tag{A.2}$$

where $\mathbf{T}$, $\mathbf{S}$, $\mathbf{E}$ and $\mathbf{D}$ are variable vectors of stress, strain, electric field and electric displacement vectors, respectively; $\mathbf{c}^E$, $\mathbf{e}$ and $\boldsymbol{\varepsilon}^S$ are the coefficients matrices of elastic stiffness, stress piezoelectric coupling and permittivity, respectively; superscript

t represents the transpose. The superscript E/S indicates that the variable is measured when the electric field/stress is held constant(Sherman and Butler, 2007).

Combined Eqs. A.1 and A.2, one can obtain

$$\left\{ \begin{array}{c} \mathbf{T} \\ \mathbf{D} \end{array} \right\} = \left[\begin{array}{cc} \mathbf{c}^E & -\mathbf{e}^t \\ \mathbf{e} & \boldsymbol{\varepsilon}^S \end{array} \right] \left\{ \begin{array}{c} \mathbf{S} \\ \mathbf{E} \end{array} \right\}$$

in which the symmetric 9×9 coefficient matrix usually contains 45 independent coefficients for a general material. However, because of the permanent polarization of PZT material, many of them are zeros or related. Eventually only 10 independent coefficients are remaining and the explicit expression is as follows

$$\left\{ \begin{array}{c} T_1 \\ T_2 \\ T_3 \\ T_4 \\ T_5 \\ T_6 \\ D_1 \\ D_2 \\ D_3 \end{array} \right\} = \left[\begin{array}{ccccccccc} c_{11}^E & c_{12}^E & c_{13}^E & 0 & 0 & 0 & 0 & 0 & -e_{31} \\ c_{12}^E & c_{11}^E & c_{13}^E & 0 & 0 & 0 & 0 & 0 & -e_{31} \\ c_{13}^E & c_{13}^E & c_{33}^E & 0 & 0 & 0 & 0 & 0 & -e_{33} \\ 0 & 0 & 0 & c_{44}^E & 0 & 0 & 0 & -e_{15} & 0 \\ 0 & 0 & 0 & 0 & c_{44}^E & 0 & -e_{15} & 0 & 0 \\ 0 & 0 & 0 & 0 & 0 & c_{66}^E & 0 & 0 & 0 \\ 0 & 0 & 0 & 0 & e_{15} & 0 & \varepsilon_{11}^S & 0 & 0 \\ 0 & 0 & 0 & e_{15} & 0 & 0 & 0 & \varepsilon_{11}^S & 0 \\ e_{31} & e_{31} & e_{33} & 0 & 0 & 0 & 0 & 0 & \varepsilon_{33}^S \end{array} \right] \left\{ \begin{array}{c} S_1 \\ S_2 \\ S_3 \\ S_4 \\ S_5 \\ S_6 \\ E_1 \\ E_2 \\ E_3 \end{array} \right\} \quad \text{(A.3)}$$

where $c_{66}^E = (c_{11}^E - c_{12}^E)/2$ and the subscripts follow IEEE convention standard: 3 is the poling direction, 1 and 2 the directions perpendicular to poling direction, and 4, 5 and 6 the shear directions 23, 13 and 12. It is worth mentioning that Abaqus uses a different convention for shear directions, i.e., $12 \rightarrow 4$, $13 \rightarrow 5$, and $23 \rightarrow 6$. An example of material properties will be shown in Section B.2.1.

Another pair of constitutive equations in d-form are also used (Sherman and Butler, 2007)

$$\mathbf{S} = \mathbf{s}^E \, \mathbf{T} + \mathbf{d}^t \, \mathbf{E} \quad \text{(A.4)}$$

$$\mathbf{D} = \mathbf{d} \, \mathbf{T} + \boldsymbol{\varepsilon}^T \, \mathbf{E} \quad \text{(A.5)}$$

where $\mathbf{s}^E$, $\mathbf{d}$ and $\boldsymbol{\varepsilon}^T$ are the matrices of elastic compliance, strain piezoelectric coupling and permittivity with constant stress.

With the d-form and e-form equations, one can derive the relationships among the coefficient matrices:

$$\mathbf{c}^E = (\mathbf{s}^E)^{-1} \tag{A.6}$$

$$\mathbf{e} = \mathbf{d}\,(\mathbf{s}^E)^{-1} \tag{A.7}$$

$$\boldsymbol{\varepsilon}^S = \boldsymbol{\varepsilon}^T - \mathbf{e}\mathbf{d}^t \tag{A.8}$$

Substituting Eqs. A.6 and A.7 into Eq. A.8, one can have other expressions of $\boldsymbol{\varepsilon}^S$ as

$$\boldsymbol{\varepsilon}^S = \boldsymbol{\varepsilon}^T - \mathbf{d}\mathbf{c}^E\mathbf{d}^t \tag{A.9}$$

or

$$\boldsymbol{\varepsilon}^S = \boldsymbol{\varepsilon}^T - \mathbf{e}\mathbf{s}^E\mathbf{e}^t \tag{A.10}$$

Besides the above introduction of piezoelectric material, some fundamentals of underwater acoustic transducers are introduced in the following sections.

A.1 Acoustic medium

The acoustic medium is very important for acoustic transducers, which is commonly a fluid, such as air and water. The properties of acoustic medium can be characterized by some parameters, including fluid density ρ, bulk modulus B and speed of sound c. Since they are related by $c = \sqrt{B/\rho}$, any two of them can fully describe the acoustic property of a fluid. For example, Abaqus, a finite-element-analysis package, uses the density ρ and bulk modulus B to define acoustic medium. Sometimes the pair of density and speed of sound are very convenient for transducer analysis. The product of them, ρc, is the specific acoustic impedance, which defines the opposition of a system to the acoustic flow. Since the acoustic impedance of water (1.5×10^6 kg/m^{2}s) is much greater than that of air (420 kg/m^{2}s), the fluid-structure interaction takes more effect when the transducer is operated in water

than in air (Sherman and Butler, 2007). The influence of water to the transducer is one of the focuses of this study, which is discussed in Chapter 4.

When dealing with problems of underwater acoustic transducers, the acoustic pressure is a principle parameter. The acoustic pressure field is caused by vibrating surfaces of a transducer, which is a time- and space- dependent scalar field. The acoustic pressure p is the variation from static pressure p_0 in the fluid, i.e., $p = p_t - p_0$, where p_t represents the total pressure. The acoustic pressure filed can be calculated by acoustic wave equation, which is derived from the following governing equations (Sherman and Butler, 2007; Wikipedia Acoustic Wave, 2018). The linearized equation of state for the fluid is

$$p = Bs \tag{A.11}$$

where $s = \frac{\rho - \rho_0}{\rho_0}$ is the condensation of the fluid, and ρ_0 is the static density or ambient fluid density.

The continuity equation (conservation of mass) can be written as

$$\frac{\partial s}{\partial t} + \nabla \cdot \vec{u} = 0 \tag{A.12}$$

where ∇ is the gradient operator and $\vec{u}$ stands for the particle velocity.

The equation of motion (conservation of momentum) is given as

$$\rho_0 \frac{\partial \vec{u}}{\partial t} = -\nabla p \tag{A.13}$$

Combining the time derivative of Eq. A.12 and the space derivative of Eq. A.13, together with substituting the equation state to eliminate s, one can obtain the acoustic wave equation for the acoustic pressure as

$$\nabla^2 p - \frac{1}{c^2} \frac{\partial^2 p}{\partial t^2} = 0 \tag{A.14}$$

where ∇^2 is the Laplace operator.

Given the solved acoustic pressure $p = p(x, y, z, t)$, one can compute other charac-

teristics of the acoustic field. For example, with Eq. A.13, the particle velocity $\vec{u}$ can be calculated.

A.2 Free flooded ring transducers

Free flooded ring (FFR) transducers refer to cylindrical tube transducers with water free-flooded interior. The inner surface of the transducer can excite the interior water column, which is proved to add radial stiffness that increases the resonant frequency and reduces the effective coupling coefficient (Sherman and Butler, 2007). FFR transducers are widely used for underwater applications because of these special features. Due to the open body design, they provide the balancing mechanism of hydrostatic pressure. Compared with other common transducers, this mechanism makes it theoretically possible to operate FFR transducer at any depth. Additionally, the low mechanical quality factor offers reasonably flat transmit response and a broad band for transmitting and receiving (Kuntsal, 2003).

Compared with most transducers, it is more difficult to calculate the acoustic pressure field because the inner, the top and the bottom surfaces are vibrating and generating sound signals. As the ring expands, the outer surface is compressing the surrounding outer water while the inner tube space is sucking water inward. The opposite effects on the transducer cause out-of-phase pressures and partial cancellation along the axis of the ring. In addition, the resonance of the interior water column can also be generated by the vibrating inner surface, which are cavity modes. The squirting resonance of first cavity mode is typically at or below ring resonance (Sherman and Butler, 2007). These cavity modes will be introduced in the next section.

A.3 Helmholtz frequency

Radial motion of the cylinder walls can excite the symmetrical cavity modes in the enclosed water column. The frequencies of these modes are given by (McMahon, 1964)

$$\omega_c^{(n)} = \frac{(2n-1)\pi c}{h + 2\alpha a} \qquad n = 1, 2, \cdots \tag{A.15}$$

where c is the speed of sound in the water column, h the length of the cylinder, a the inside radius, and α the end correction coefficient.

Now only consider $n = 1$. $\omega_c^{(1)}$ is the fundamental resonant frequency of the enclosed water column, which is called Helmholtz frequency ω_h. For dimensionless quantity $\Omega = \omega_h a/c$ from 0.33 to 3.3, the theoretical curve of the end correction parameter can be expressed as

$$\alpha = 0.633 - 0.106\Omega \tag{A.16}$$

Combining Eqs. A.15 and A.16, one have the equation

$$\Omega(h/2a + 0.633) - 0.106\Omega^2 = \pi/2 \tag{A.17}$$

Given the length $h = 0.013$ m and the inside radius $a = 0.011$ m of the transducer, together with Eq. A.17, one can compute $\Omega = 1.4708$. Therefore, Eqs. A.16 and A.15 yield $\alpha = 0.4771$ and $f_h = \omega_h/(2\pi) = 31.133$ kHz, which is the Helmholtz frequency of the tube transducer used in this study.

Before using the above theoretical value for further study, four FE tests are done to discuss the influence of surrounding water to the resonant frequencies of the transducer:

- Water is surrounding the transducer both inside and outside the tube, which is named $IWOW$ shown in Fig. A.1 (a).
- The transducer is placed in water but it is filled by air inside the tube ($IAOW$) shown in Fig. A.1 (b).

- The transducer is placed in air but there is a water column inside the tube ($IWOA$) shown in Fig. A.1 (c).
- The transducer is modeled in air and no water is involved ($IAOA$) shown in Fig. A.1 (d).

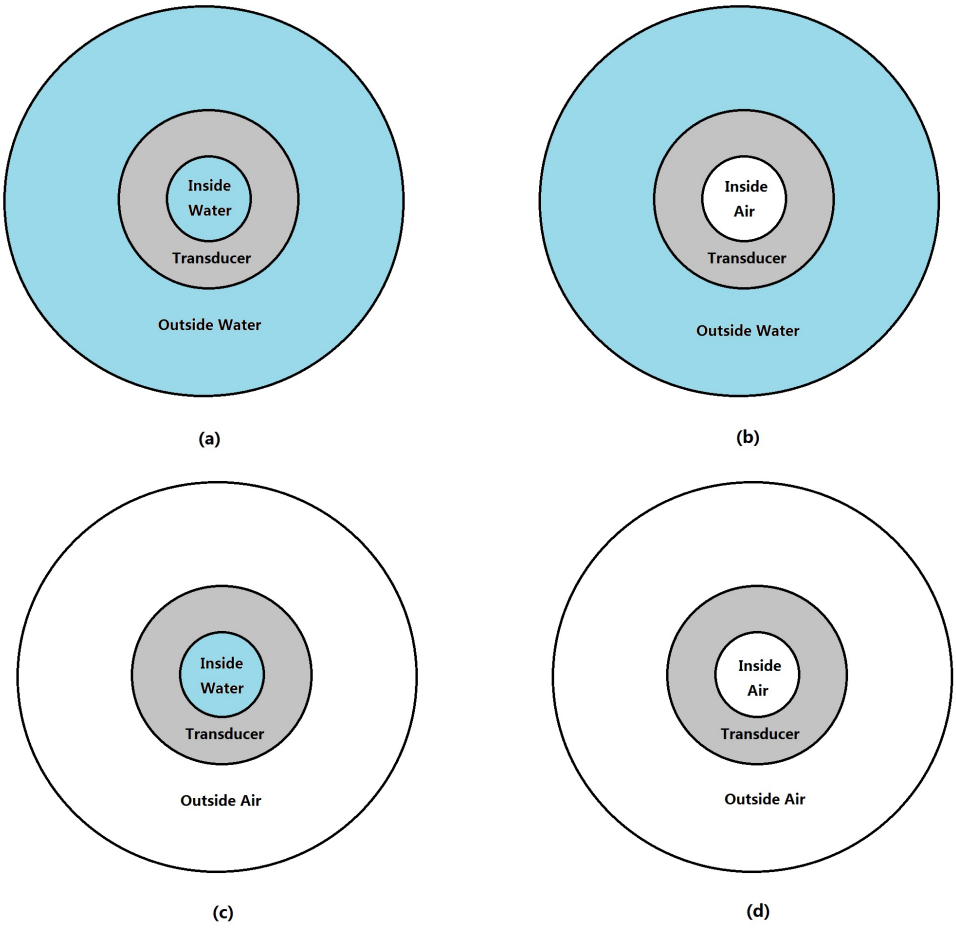

Figure A.1. The sketch of models for testing the influence of surrounding water to the resonant frequencies (top view): (a) $IWOW$; (b) $IAOW$; (c) $IWOA$; (d) $IAOA$. Colors of blue, grey and white indicate the water, the transducer and the air, respectively.

According to the definition of resonant frequency, adding stiffness means higher frequency while adding mass means lower frequency. Table A.1 shows the resonant frequencies of those four cases, calculated from impedance function by pole-

residue operation. If focusing on the radial mode in Column 2, the comparison between $IAOA$ and $IAOW$ ($37.6722 < 43.1021$) or between $IWOA$ and $IWOW$ ($45.8825 < 48.0953$) indicates that the outside water is equivalent to adding mass effect to the system. The above theoretical solution only considers the inside water column and the transducer, which is very similar to the senario $IWOA$. According to the above conclusion that outside water adds mass effect to the system, the Helmholtz frequency of $IWOW$ would be lower than theoretical value, which matches the results in Column 1 of Table A.1.

Table A.1. Resonant frequencies (kHz) for different models of water column influence

scenarios	Helmholtz	radial mode	bending mode	longitudinal mode
IWOW	24.8125	45.8825	55.0218	126.5384
IWOA	33.1923	48.0953	57.1127	127.7400
IAOW	$--$	37.6722	57.5884	127.1357
IAOA	$--$	43.1021	60.0112	129.5881

APPENDIX B

Finite Element Model

The finite element method (FEM) is one of the most important and useful tools for engineers and researchers. It is a numerical method to solve the differential equations of mathematical models of engineering systems, which are usually hard to obtain the theoretical solutions. Therefore, FEM has been widely applied to most fields of engineering analysis, such as structures and solids, fluid mechanics, and heat transfer. The electroacoustical transducer used in this study involves multiple disciplinary, including mechanical, electrical and acoustical domain. Since it is extremely difficult to have analytical solutions of multiphysics problems, the development of FE modeling gives people more effective and more efficient ways to solve them. Many FE software packages are capable of modeling the transducers, such as Abaqus, ANSYS, and COMSOL. In this study, all the FE models are developed in Abaqus.

B.1 Abaqus introduction

Abaqus is a popular software package for finite element analysis, which was originally developed for nonlinear problems and is now widely used in plenty of industries applications for solving routine and complicated engineering problems. For example, in the automotive industry, engineers use Abaqus to solve problems of full vehicle loads, dynamic vibration, nonlinear static analysis, thermal coupling, etc. Abaqus also has multiphysics capabilities, such as piezoelectric and coupled acoustic-structural capabilities, which are used for the simulations of underwater acoustic transducers in this study.

A complete finite-element analysis can usually be divided into 3 stages (Abaqus Release Notes, 2014; Wikipedia Abaqus, 2018):

- **Preprocessing or modeling**: In this stage, users can create a FE model of specific physical problem, including geometries, materials, mesh, etc. Two methods are available in Abaqus:
  - **Abaqus/CAE**: It is a Complete Abaqus Environment that provides an GUI window for creating, submitting, monitoring, and evaluating results from Abaqus simulations. Abaqus/CAE is divided into modules, where each module defines a logical aspect of the modeling process; for example, defining the geometry under the *Parts* module, creating and submitting analysis jobs under *Jobs* module, and interpreting results under *Visualization* module. Therefore, Abaqus/CAE can usually be used for all 3 stages. However, some specific applications/functions are only available for input file.
  - **Input file**: It is a script file using Abaqus programming language, which contains 3 types of input lines, i.e., keyword lines, data lines, and comment lines. Thus, input file can be used for both preprocessing and analysis stages.

  Besides Abaqus, the first stage can also be done by other compatible CAD software, or even a text editor, for example, ANSYS input file and AutoCAD.

- **Processing or finite element analysis**: In this stage, finite element analysis is carried out and output data are produced, which can be submitted to the solver by Abaqus/CAE and input file. There are 3 analysis products in Abaqus:
  - **Abaqus/Standard**: This general-purpose analyzer provides a wide range of static, dynamic, thermal, electrical, and piezoelectric analysis of linear and nonlinear problems using implicit time integration. The

mechanical-electrical-acoustical transducer used in this study can be modeled and simulated by this product because the elements of coupling three domain are only available in Abaqus/Standard.

  - **Abaqus/Explicit**: This analyzer specifically provides dynamic analysis of highly nonlinear systems under transient loads using explicit time integration. Its powerful contact capabilities on large models also make it highly effective for solving discontinuous nonlinear problems. This product has the capability of structural-acoustic coupling, but piezoelectric elements are not available for further coupling.

  - **Abaqus/CFD**: This analyzer provides dynamic analysis of fluids, nonlinear coupled fluid-thermal and fluid-structural problems with extensive support for modeling, analysis, and postprocessing in Abaqus/CAE.

- **Postprocessing or results visualization**: In this stage, users can visualize the results from the output file (.odb) through *Visualization* module, such as extracting modal frequencies, plotting mode shapes, generating animation and writing desired data to separate files.

To solve problems of special fields, Abaqus provides many add-on analyses for users, such as Abaqus/Aqua, Abaqus/Design and Abaqus/Foundation. In addition, Abaqus translators also provides the interfaces between other FE software packages, such as ANSYS, LS-DYNA, and NASTRAN. If interested, the readers can refer to Abaqus manuals.

The following sections show the FE models of the underwater acoustic transducer in air and in water as well as some techniques used in this study.

B.2 FE model of the transducer

In this section, major procedures of building up the models will be shown, including the properties of a piezoelectric material, mechanical and electrical boundary conditions, and modal and dynamic analyses.

B.2.1 FEM in air

Shown in Fig. B.1, the tube transducer used in this study is radially polarized and made of piezoelectric material PZT4 with dimensions $13mm \times 26mm \times 22mm$ ($L \times OD \times ID$). When studying the mechanical properties, the transducer in air is treated as in vacuum because of the negligible influence of air. The piezoelectric material is electroded on both the inner and outer surfaces. The material properties from the manufacturer specification sheet are shown in Table B.1

material properties		units	values
Young's modulus	Y_{33} $(1/s_{33}^E)$	GPa	73
	Y_{11} $(1/s_{11}^E)$	GPa	86
piezoelectric coupling	d_{33}	pm/V	320
	d_{31}	pm/V	-140
dielectric	$\varepsilon_{33}^T/\varepsilon_0$	–	1400

Table B.1. The material properties of modified PZT4 (SM111) from STEINER & MARTINS, INC. (STEMiNC, 2018)

where the manufacturers always follow IEEE convention standard and use subscript 3 for the poling direction and subscripts 1 and 2 for the perpendicular directions.

As shown in Table B.1, the manufacturer only gives 5 parameters out of 10 independent ones, which are necessary to fully describe the piezoelectric materials. Since 4 of the 5 missing ones are of negligible importance, they are just filled by the values of typical PZT4 properties from textbooks (Sherman and Butler, 2007): compliance $s_{13}^E = -5.31$ pm^2/N, compliance $s_{44}^E = 39$ pm^2/N, piezoelectric constant $d_{15} = 496$ pm/V, and permittivity $\varepsilon_{11}^T/\varepsilon_0 = 1475$. In terms of the parameters

totally provided by the manufacturer, the important compliance coefficient s_{12}^E can be calculated with the formula (Sherman and Butler, 2007)

$$s_{12}^E = \frac{2d_{31}g_{31}}{k_p^2} - s_{11}^E = -2.4721 \text{ pm}^2/\text{N}$$

where g-form piezoelectric constant $g_{31} = -11 \times 10^{-3}$ Vm/N and electromechanical coupling coefficient $k_p = 0.58$ are also from the manufacturer specification sheet (STEMiNC, 2018).

Since compliance coefficients are not allowed for elasticity in Abaqus, the e-form property matrices in a cylindrical system are used:
Stiffness matrix c_{ij}^E:

$$\begin{bmatrix} 132.64 & 76.92 & 76.92 & 0 & 0 & 0 \\ 76.92 & 134.68 & 63.76 & 0 & 0 & 0 \\ 76.92 & 63.76 & 134.68 & 0 & 0 & 0 \\ 0 & 0 & 0 & 25.64 & 0 & 0 \\ 0 & 0 & 0 & 0 & 25.64 & 0 \\ 0 & 0 & 0 & 0 & 0 & 35.46 \end{bmatrix} \text{ GPa}$$

Piezoelectric coupling matrix (stress coefficients e_{ij}):

$$\begin{bmatrix} 20.9048 & -3.1669 & -3.1669 & 0 & 0 & 0 \\ 0 & 0 & 0 & 12.7179 & 0 & 0 \\ 0 & 0 & 0 & 0 & 12.7191 & 0 \end{bmatrix} \text{ C/m}^2$$

Dielectric matrix with constant strain ε_{ij}^S:

$$\begin{bmatrix} 4.819 & 0 & 0 \\ 0 & 6.752 & 0 \\ 0 & 0 & 6.752 \end{bmatrix} \times 10^{-9} \text{ F/m}$$

The 1-, 2- and 3-direction are radial, tangential, and axial, respectively. In this model, the poling direction is radially outwards from the axis of symmetry (1-direction). The mass density is 7900 kg/m^3. A light Rayleigh damping model is assumed for the piezoelectric material with coefficients $\alpha = 700$, $\beta = 1.3 \times 10^{-9}$. As Fig. B.1 shows, the transducer is modeled by a piece of cross section of the cylinder tube structure with 8-node axisymmetric piezoelectric elements (CAX8E).

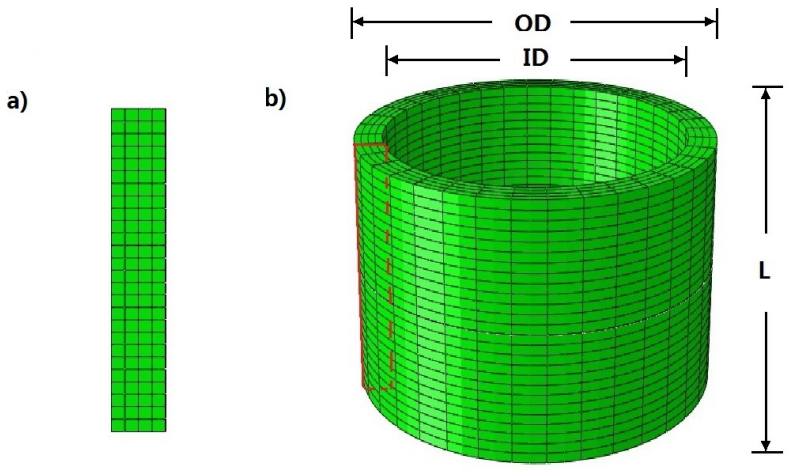

Figure B.1. The geometry and finite element model of the transducer in air: a) 2D axisymmetric model, b) 3D model

First, linear perturbation frequency analysis is performed under short-circuit condition, where the potentials on both the inside and outside surfaces are set to 0. The modal frequencies correspond to the resonance of the transducer. There are 3 x-axis symmetric modes under 200 kHz, whose resonant frequencies are 43.790 kHz, 60.189 kHz and 129.924 kHz and mode shapes are shown in Fig. B.2. Likewise, the frequency analysis is performed under open-circuit condition, where potential on one side is set to 0 and that on the other side is left unspecified. The modal frequencies, corresponding to the anti-resonance of the transducer, under 200 kHz are 46.744 kHz, 60.203 kHz, and 145.962 kHz.

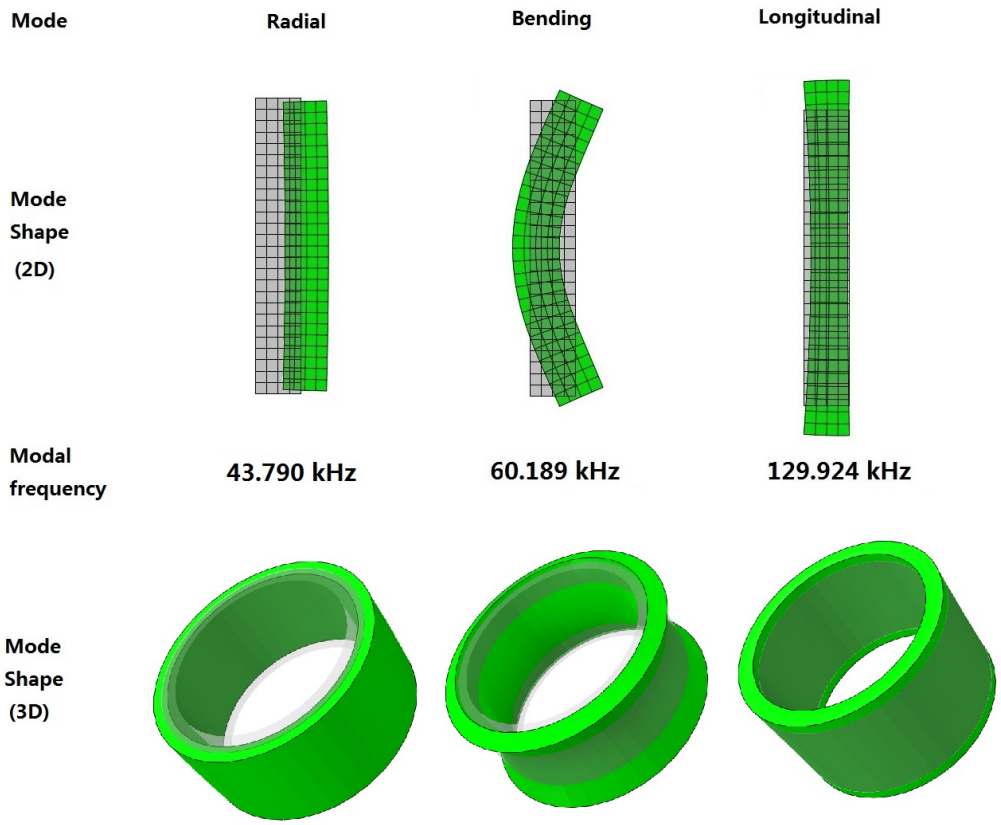

Figure B.2. Modal frequencies and corresponding mode shapes of the transducer in air under short-circuit (grey for original shape, green for deformed one) condition

Dynamic analysis is defined through *Step* module by the keyword *dynamic, implicit*. Since inner/outer surface is physically equipotential, a constraint using keyword *equation* is applied to couple the electrical degree of freedoms of all nodes on the surface. The excitation is applied through the electrical boundary condition, which is a sinusoidal electrical potential with the amplitude 1 V and the frequency 30 kHz. The time increment and total time duration are set to be 0.2 μs and 400 μs, respectively. At the same time, the reactive electrical nodal charge $q(t)$ is calculated. Shown in Fig B.3 are the input electrical potential and output reactive change.

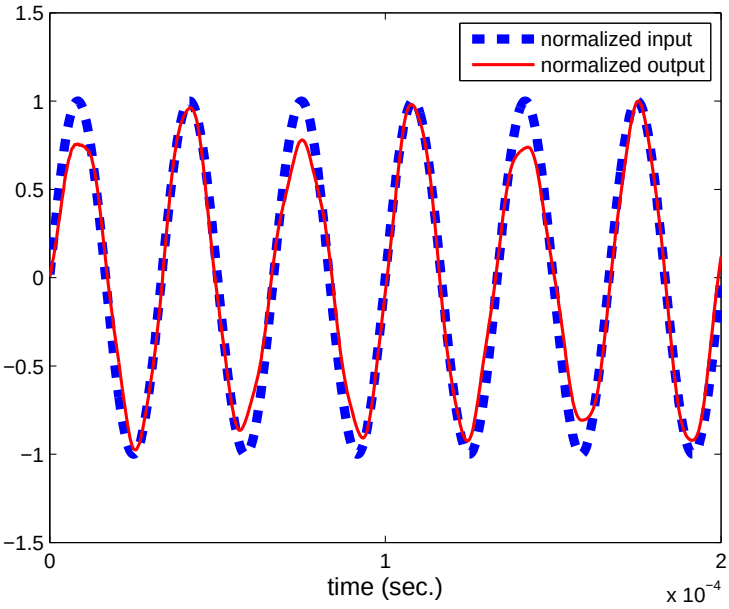

Figure B.3. Normalized input voltage and output charge for the transducer in air: voltage scale 1 V, charge scale 7.8253×10^{-9} C

B.2.2 FEM in water

The spherical water domain is modeled by 4-node linear axisymmetric acoustic elements (ACAX4) with radius 0.2 m and mesh size 1.1×10^{-3} m. The water properties are defined by density $\rho_w = 1000$ kg/m^3 and bulk modulus $B = 2.1404$ GPa.

The surface-based *tie* constraint is used to couple the transducer and the surrounding water. Surfaces are defined at the outside of the transducer and at the water free surface adjacent to the transducer. To consider the symmetric property, all points of the bottom and the left boundary for both water and the transducer are constrained no move along longitudinal and radial directions, respectively. The *Acoustic Impedance* under *Interactions* module is used to model the motions of waves out of the mesh, which is an impedance-type radiation boundary condition. The *nonreflecting* boundary condition is applied at water domain boundary (located 0.2 m away from the center), which absorbs the acoustic wave (shown in

Fig. 5.1). More details can be referred to section B.3.

Modal analysis shows that there are thousands of modes for the coupled acoustic-structure model, each of which includes both mechanical and acoustical patterns. Shown in Fig. B.5 are the acoustic radiating patterns of some typical modes for this tube transducer.

Dynamic analysis is performed through the *dynamic, implicit* under *Step* module. The input is a sinusoidal signal with the amplitude 1 V and the frequency 30 kHz. The output will be reactive nodal charge and acoustic pressure at 10 cm away from the center of water domain, which is shown in Fig. B.4.

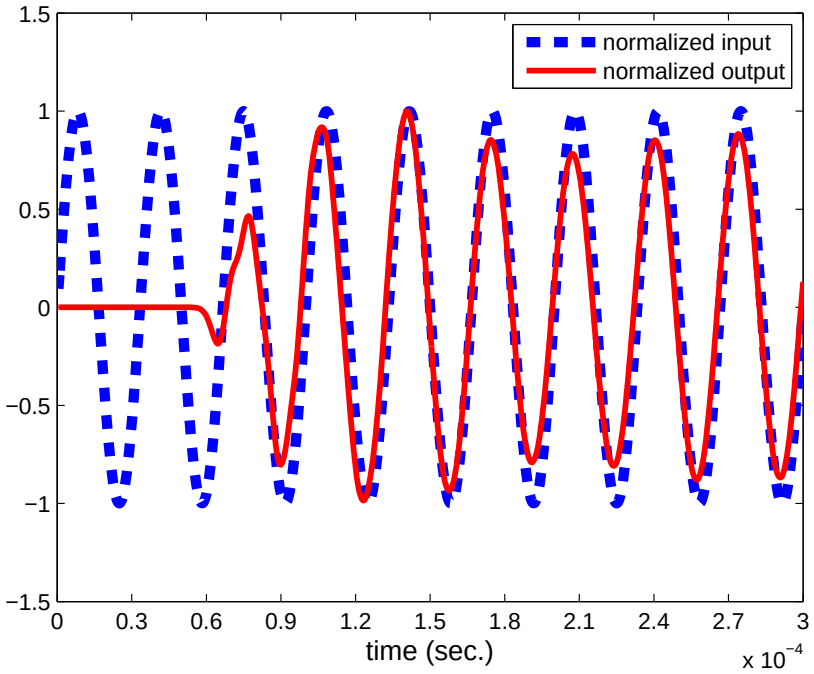

Figure B.4. Normalized input voltage and output pressure for the transducer in water: voltage scale 1 V, pressure scale 61.7224 Pa

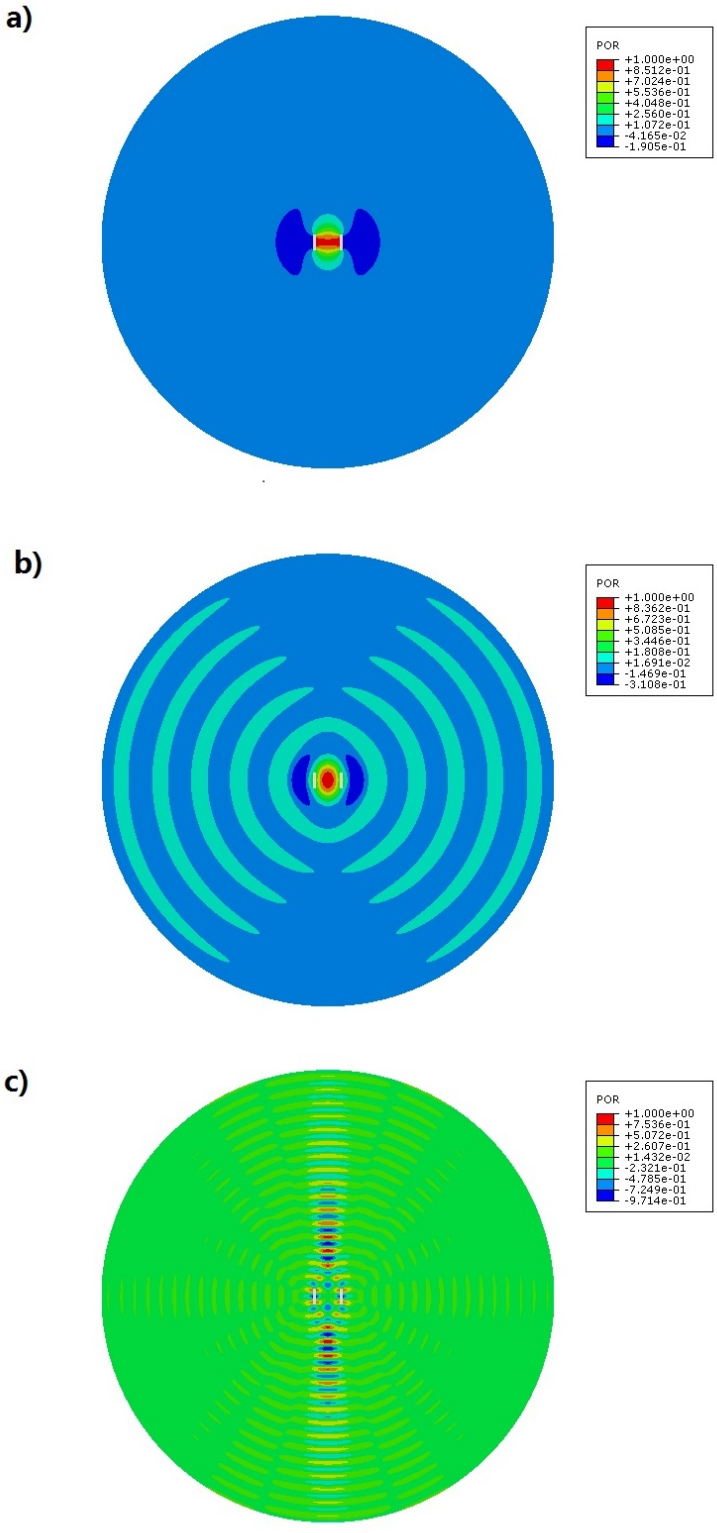

Figure B.5. Radiating patterns of three typical modes for the transducer: a) Helmholtz mode, b) radial mode, and c) longitudinal mode.

B.3 Key techniques of FEM

In this section, some key techniques used in the FE model will be demonstrated for both CAE and input-file usages, including electrical constraints, fluid-structure interaction, acoustic field boundary, and mesh refinement.

B.3.1 Electrical constraints

In this dissertation, 2D axisymmetric piezoelectric elements are used for the simulation of the tube transducer. Physically, the inner and the outer surfaces are coated by a very thin silver layer electrically. So, all the degrees of freedom in those two surfaces are constrained to be equipotential, including the amplitude and the phase angle. A linear multi-point constraint *equation* will be used to carry it out in Abaqus.

This technique requires that a linear combination of nodal variables is equal to zero (Abaqus Keywords, 2014)

$$A_1 u_i^P + A_2 u_j^Q + \ldots + A_N u_k^R = 0 \tag{B.1}$$

where u_i^P is a nodal variable at node P, degree of freedom i; and the A_N are coefficients that define the relative motion of the nodes.

To define a linear constraint equation, the coefficients in Eq. B.1 must be specified. For input file usage, the parameters are listed in the following way (Abaqus Keywords, 2014)

- First line
  - Number of terms, N_t, in the equation
- Following lines
  - Node number or node set label, P, of first nodal variable, u_i^P.
  - Degree of freedom, i, at above node for variable u_i^P.

- Value of A_1
- Node number or node set label, Q, of second nodal variable, u_j^Q.
- Degree of freedom, j, at above node for variable u_j^Q.
- Value of A_2
- Etc., up to four terms per line

For the transducer used in this dissertation, in order to define a equipotential surface, one needs to make sure that the electrical potential of each node keeps identical to that of any other one on the surface. To implement this constraint, the users need to select one reference point (P^1) and the remaining ones on the surface ($P^i,\ i = 2, \ldots, N_p$) to form a group of equations

$$P_9^1 - P_9^i = 0, \qquad i = 2, \ldots, N_p$$

in which N_p is the number of node points in one constrained surface and *9* stands for the electrical degree of freedom in Abaqus. So, the input usage for the inner surface of this transducer model will be

**Equation*

2

pzt-1.inner-others, 9, -1.

pzt-1.inner-main, 9, 1.

where the number 2 in the first line means that there are 2 terms in the equation, *pzt-1.inner-main* and *pzt-1.inner-others* in the following lines are the node set labels for the selected reference node P^1 and all remaining nodes P^i on the inner surface respectively, -1 and 1 are the corresponding coefficient values of node variables. It is worth mentioning that the first set can contain one or more points while the subsequent sets must contain only one single point. This rule applies for both input-file and CAE usages.

In Abaqus/CAE, one can set it by *Create Constraint: Equation* under the *Interaction (Constraints)* module, which is shown in Fig. B.6.

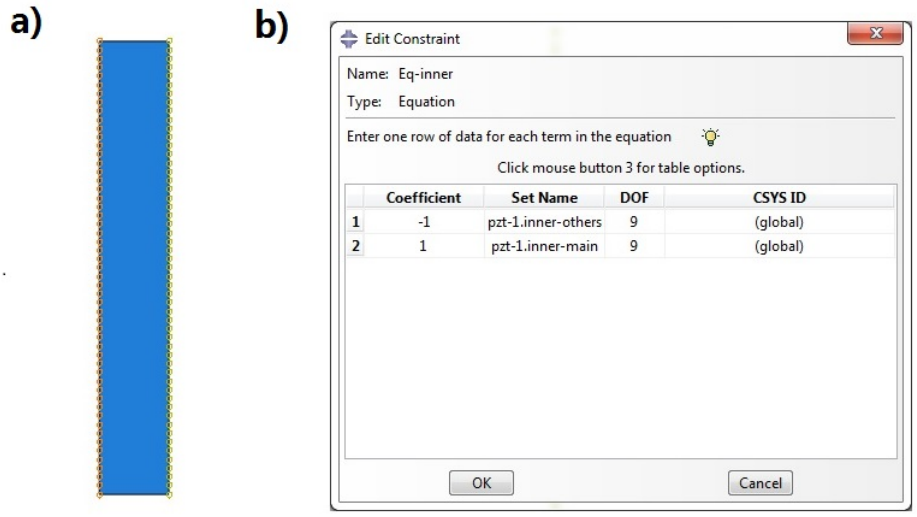

Figure B.6. Setup of electrical constraint *Equation* in Abaqus/CAE. a), constrained nodes on the inner surface; b),l setup window of the constraint *Equation*

B.3.2 Fluid-Structure Interaction (FSI)

In the FSI region, momentum and energy are transferred between the transducer and the acoustic medium (water). The interaction means that water creates a normal surface traction on the transducer and the vibrational surface of the transducer creates the natural forcing term on water.

In this study, the interaction is just simply modeled by a surface-based coupling procedure of *tie* constraint, using which users need to define two surfaces on the structural and fluid meshes as well as the interaction between the two meshes. For this *tie* constraint, Abaqus automatically computes the region of influence for each internally generated acoustic-structural interface element (Abaqus Analysis, 2014).

A *tie* constraint is defined by a set of parameters, including required (*name*),

mutually optional (*position tolerance*, *tie nset*), and optional ones (*adjust*, *constraint ratio*, etc). So, the input-file usage for the interaction will be

**Tie, name=FSI, adjust=yes*

transducer-1.FSI-transducer, water-1.FSI-water

where *FSI*, *transducer-1.FSI-transducer* and *water-1.FSI-water* are user-defined names of the interaction, coupled surface of the transducer (slave surface), and coupled surface of water (master surface), respectively. The setting *adjust=yes* is the default of optional parameter *adjust*. Since the water mesh is coarser than the transducer mesh, the water surface serves as the master surface.

In Abaqus/CAE, one can set it by *Create Constraint: Tie* under the *Interaction (Constraints)* module, which is shown in Fig. B.7.

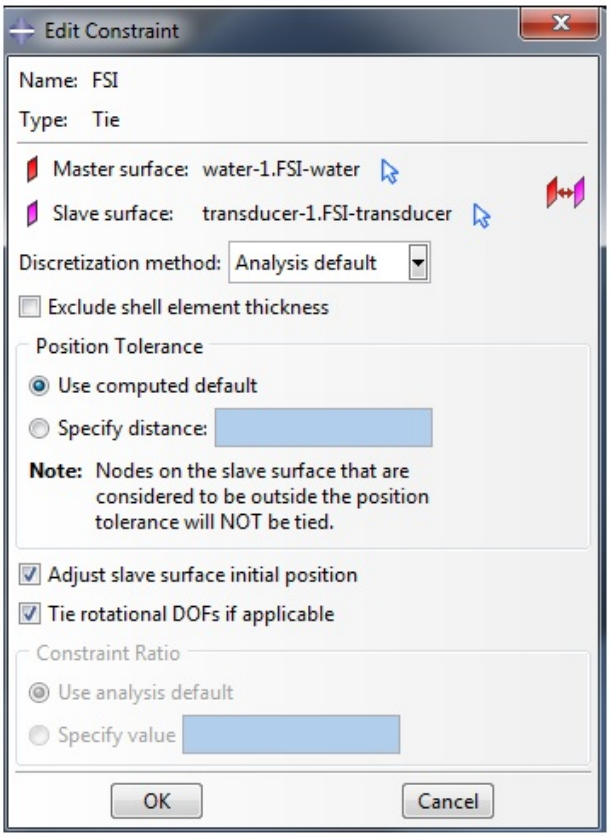

Figure B.7. Setup of fluid structural interaction *tie* in Abaqus/CAE

B.3.3 Acoustic field boundary

In Abaqus, the default boundary condition for an acoustic medium is a boundary with a stationary rigid wall or a symmetry plane. So, some technique needs to be applied to model an acoustic medium of infinite extent. Impedance-type radiation boundary condition is used to model the motions of waves out of the mesh in this study.

A boundary impedance specifies the relationship between the pressure of an acoustic medium and the normal motion at the boundary. All the points on the boundary surface is governed by (Abaqus Analysis, 2014)

$$\dot{u}_{out} = \frac{1}{k_1}\dot{p} + \frac{1}{c_1}p$$

where $\dot{u}_{out}$ is the acoustic particle velocity in the outward normal direction of the acoustic medium surface, p is the acoustic pressure, $1/k_1$ is the proportionality coefficient between the pressure and the displacement normal to the surface, and $1/c_1$ is the proportionality coefficient between the pressure and the velocity normal to the surface.

This model can be conceptualized as a spring and dashpot in series placed between the acoustic medium (water domain) and a rigid wall (boundary of the water domain). The spring and dashpot parameters are k_1 and c_1, respectively. When the coefficients k_1 and c_1 are chosen for some specific values, the boundary will be energy absorbing. In order to specify this boundary condition, users can define the impedance condition on a surface. The impedance is applied to element edges in two dimensions and to element faces in three dimensions.

For input-file usage, the keyword *simpedance* is used to provide surface impedance information or nonreflecting boundaries for the acoustic analysis, in which parameters, including *property*, *nonreflecting* and *op (optioanl)*, need to be specified. Available options for *nonreflecting* includes planner, circular, ellipti-

cal, etc. In this study, the transducer is simulated by 2D axisymmetric elements so that the boundary is circular as shown in Fig. B.8. The input-file usage for impedance-type boundary will be

**Simpedance, nonreflecting=circular*

WaterBoundary, 0.2

where *WaterBoundary* is the surface name and *0.2* is the specified radius (in meter) of the circle, which defines the absorbing boundary surface.

In Abaqus/CAE, one can set the boundary condition by *Acoustic impedance* under the *Interaction* module, which is shown in Fig. B.8).

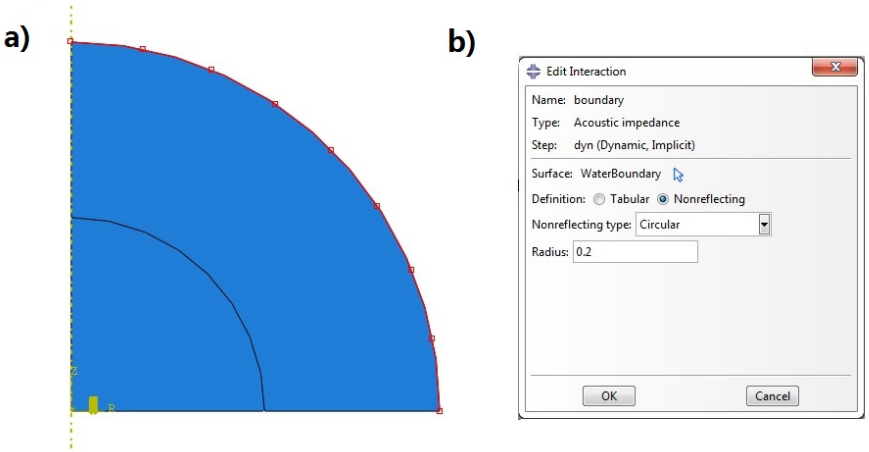

Figure B.8. Setup of acoustical field boundary in Abaqus/CAE. a), the boundary surface in the model; b), setup details of the boundary condition

In order to verify the effectiveness of the boundary condition, two experiments are designed: 1) the transducer is placed in a water domain with radius 0.2 m, and 2) the transducer is placed in a water domain with radius 0.3 m. Impedance-type boundary conditions are applied at the boundaries of water domain. Fig. B.9 shows the comparison of acoustic pressure history, which are measured at the location $(0.1, 0)$. Since there are some noticeable differences only after $t_r = 196$ μs, it indicates that the boundary can't perfectly absorb the incident waves. But,

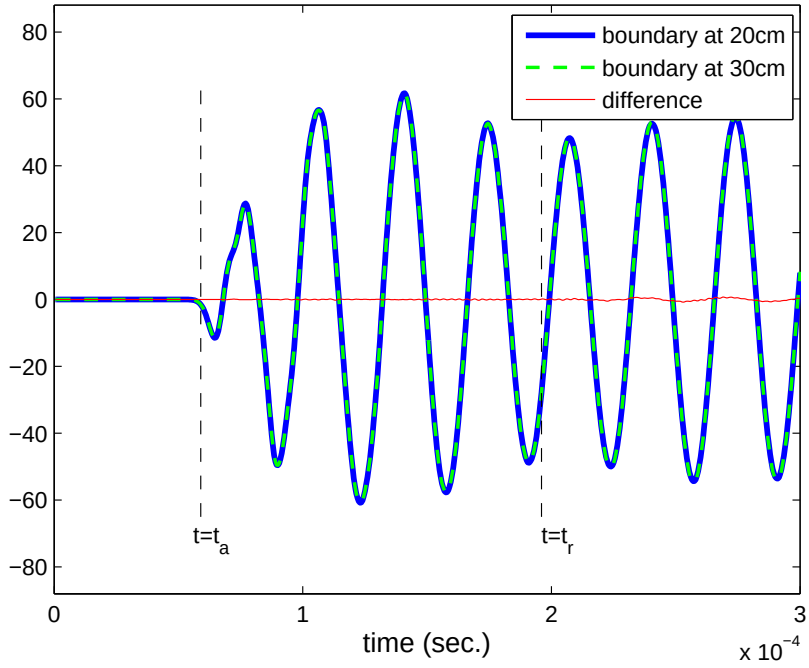

Figure B.9. The comparison of acoustic pressures (at 0.1 m away from the center of the transducer) from two models with different size of water domain: radius 0.2 m and radius 0.3 m. t_a and t_r represent the arrival time of acoustic waves, 59 μs, and the travel time of possible reflective waves, 196 μs, respectively.

the difference, up to 1.17% of maximum pressure, shows that the impedance-type boundary condition is good enough to model the acoustic medium to infinite extent.

B.3.4 Mesh refinement

In acoustic and vibration analysis, users usually need to judge whether the mesh of the model is fine enough, which is a common trade-off between accuracy and efficiency. For reasonable accuracy, at least six internodal intervals of the acoustic mesh per shortest acoustic wavelength are necessary. An internodal interval means the distance between a node and its nearest neighbor in an element, which is the element size for a linear element or half of the element size for a quadratic element. Any finite element discretization of a domain in which waves

propagate introduces a certain amount of error per wavelength. In larger meshes, the accumulated per-wavelength error may be present if the mesh refinement is inadequate (Abaqus Analysis, 2014).

Therefore, the requirement of mesh size can be expressed as

$$n_{min} L_{max} \leqslant \lambda_{min} \tag{B.2}$$

where n_{min}, L_{max}, and λ_{min} represent the minimum number of internodal intervals per acoustic wavelength, the maximum internodal interval of an element, and the minimum acoustic wave length of interest, respectively. Since the frequency of acoustic wave is concerned, Eq. B.2 can be rewritten as

$$L_{max} \leqslant \frac{c}{n_{min} f_{max}} \tag{B.3}$$

in which f_{max} is the maximum acoustic frequency of interest, and c the speed of sound in the medium.

Eq. B.3 can be used to estimate the maximum allowable element length if the maximum frequency of interest is given. For the underwater transducer used in this study, the parameters used are speed of sound in water $c = \sqrt{B/\rho_w} = 1463$ m/s, $n_{min} = 8$, and maximum acoustic wave frequency of interest $f_{max} = 160$ kHz. Thus, the maximum element length can be computed by Eq. B.3 as $L_{max} = 1.1$ mm.

APPENDIX C

Model Updating of Piezoelectric Transducers

C.1 Introduction

The values of piezoelectric material properties from the manufacture's specification sheets are often inaccurate, the tolerance of which could be up to 20%. However, some of them are essential to the performance of the transducer, which significantly affect the accuracy of finite element (FE) model. As Fig. C.1 shows, the discrepancy between FE model and experimental results indicates the necessity of model updating.

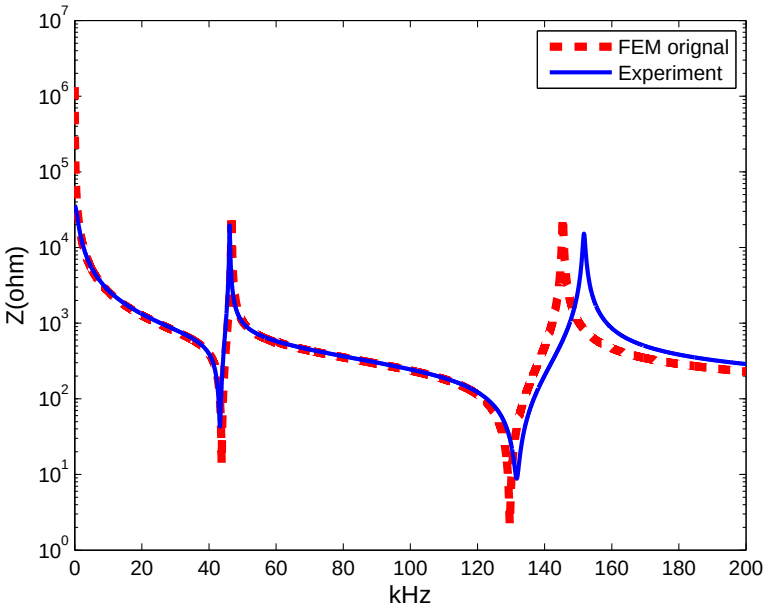

Figure C.1. Impedance function comparison of the transducer in air: original FE model v.s. experiment

Traditionally, there are mainly two types of model-updating techniques: direct methods using modal data and iterative methods using modal data (Friswell and Mottershead, 1995). The direct methods are capable of reproducing the measured data exactly, which are based on the calculation of direct changes

to the mass and stiffness matrices. But, those updated matrices in this way are lack of physical meaning and very hard to be interpreted in the original FE model. Therefore, the direct methods are usually called "represential". The iterative methods aims at improving the correlation between the measured data and the FE model, which have more physical meaning. Generally, the correlation is determined by a nonlinear penalty function, which involves the eigenvalues and mode shapes data. Therefore, the convergence of updated parameters needs to be proved after the iterative procedures. Although there are some problems for implementing the method, such as pairing the same mode and damping related issue, it has been successfully applied to update the parameters of ultrasound transducers (Piranda et al., 1998; Piranda et al., 2001).

The model-updating method used in this study is the cross-model cross-mode (CMCM) method, which combines the advantages of both direct methods and iterative methods (Hu et al., 2007). Based on the modal frequencies obtained from the impedance function, one can update the parameters of a piezoelectric transducer, even when the measured mode shapes are incomplete (extended CMCM method, Su, 2016). Details will be shown in the following sections.

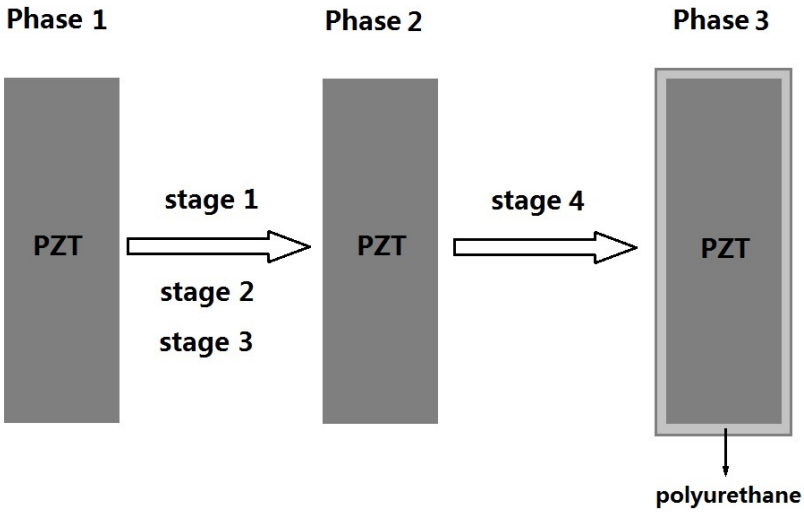

Figure C.2. Model updating procedures of a tube piezoelectric transducer

As shown in Fig. C.2, there are 3 phases of the transducer (cross sections of the tube) and 4 stages to update the material properties of FE model to match the experimental data before it is ready into water. Phase 1, 2 and 3 are FE models with original piezoelectric parameters from manufacturer, updated piezoelectric parameters, and updated piezoelectric transducer with a polyurethane layer, respectively. To update the piezoelectric material from phase 1 to phase 2, one needs to carry out 3 stages, including the model-updating of elastic, dielectric and piezoelectric coupling parameters. Since the transducer needs to be prevented from short-circuited by water, a thin polyurethane coating layer is added to the surface of the transducer in phase 3. Stage 4 demonstrates the updating of polyurethane material coefficients. Since it is very thin and its key contribution to the system is mass effect instead of stiffness, this material is simply considered to be linear elastic material in this study. This chapter shows the key theories and procedures of model updating of the above transducer.

C.2 Methodology

As shown in Eq. A.3, the piezoelectric material can be fully defined by 10 independent parameters, namely, 5 elastic, 2 dielectric and 3 piezoelectric coefficients. According to the sensitivity study in the reference (Su, 2016), there are 6 insensitive parameters s_{13}^E, s_{33}^E, s_{44}^E, ε_{11}^T, d_{33} and d_{15} for a thin-wall tube transducer, which can theoretically be arbitrary values and will be simplified in the following way

$$s_{13}^E = s_{12}^E,\ s_{33}^E = s_{11}^E,\ s_{44}^E = s_{66}^E \tag{C.1}$$

and

$$\varepsilon_{11}^T = 0, \quad d_{33} = d_{15} = 0 \tag{C.2}$$

The 4 remaining parameters are 2 elastic (s_{11}/c_{11}, s_{12}/c_{12}), 1 dielectric ($\varepsilon_{33}^T/\varepsilon_{33}^S$) and 1 piezoelectric ($d_{31}/e_{31}$).

When updating the transducer model from Phase 1 to Phase 2, the system equations for the piezoelectric transducer can be written as

$$\begin{bmatrix} \mathbf{M} & \mathbf{0} \\ \mathbf{0} & \mathbf{0} \end{bmatrix} \begin{Bmatrix} \ddot{\mathbf{U}} \\ \ddot{\mathbf{\Phi}} \end{Bmatrix} + \begin{bmatrix} \mathbf{K}_{UU} & \mathbf{K}_{U\Phi} \\ \mathbf{K}_{\Phi U} & \mathbf{K}_{\Phi\Phi} \end{bmatrix} \begin{Bmatrix} \mathbf{U} \\ \mathbf{\Phi} \end{Bmatrix} = \begin{Bmatrix} \mathbf{F} \\ \mathbf{Q} \end{Bmatrix} \tag{C.3}$$

where $\mathbf{M}$, $\mathbf{K}_{UU}$, $\mathbf{K}_{U\Phi}/\mathbf{K}_{\Phi U}$, and $\mathbf{K}_{\Phi\Phi}$ are the matrices of mass, displacement stiffness, piezoelectric coupling stiffness, and dielectric 'stiffness', respectively; $\mathbf{U}$ and $\mathbf{\Phi}$ are the coupled variables of displacements and electrical potentials; $\mathbf{F}$ and $\mathbf{Q}$ stand for the external forces and the electrical charges.

If the electric potential $\mathbf{\Phi}$ is controlled, the first equation in C.3 becomes

$$\mathbf{M}\ddot{\mathbf{U}} + \mathbf{K}_{UU}\mathbf{U} = \mathbf{F} - \mathbf{K}_{U\Phi}\mathbf{\Phi} \tag{C.4}$$

where the right hand side is the total loads, i.e. external forces and equivalent electrical loads. Assuming a short-circuit condition ($\mathbf{\Phi} = \mathbf{0}$), one can get the eigenvalue problem as

$$(\mathbf{K}_{UU} - \omega_r^2\mathbf{M})\mathbf{U} = \mathbf{0} \tag{C.5}$$

in which ω_r represents the modal frequencies of the short-circuit model.

Likewise, if the system is open-circuited ($\mathbf{Q} = \mathbf{0}$), the second equation of C.3 can be rewritten as

$$\mathbf{\Phi} = -(\mathbf{K}_{\Phi\Phi}^{-1}\mathbf{K}_{\Phi U})\mathbf{U} \tag{C.6}$$

Combining Eq. C.6 and Eq. C.4, one obtains

$$\mathbf{M}\ddot{\mathbf{U}} + (\mathbf{K}_{UU} - \mathbf{K}_{U\Phi}\mathbf{K}_{\Phi\Phi}^{-1}\mathbf{K}_{\Phi U})\mathbf{U} = \mathbf{F} \tag{C.7}$$

Denoting the condensed eletro-elastic stiffness matrix

$$\tilde{\mathbf{K}}_{UU} = \mathbf{K}_{UU} - \mathbf{K}_{U\Phi}\mathbf{K}_{\Phi\Phi}^{-1}\mathbf{K}_{\Phi U} \tag{C.8}$$

one can get the eigenvalue problem under open-circuit condition as

$$(\tilde{\mathbf{K}}_{UU} - \omega_a^2\mathbf{M})\mathbf{U} = \mathbf{0} \tag{C.9}$$

where ω_a represents the modal frequencies of the open-circuit model.

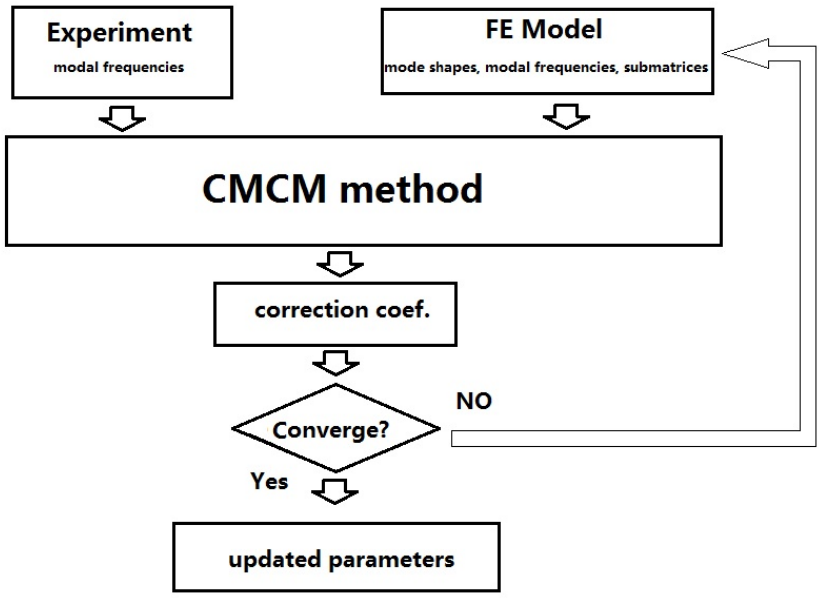

Figure C.3. Flowchart of the extended CMCM method to update the parameters of piezoelectric material

The CMCM method employed in this study is intended to update the mass and stiffness matrices by some measured modal frequencies (ω_r and ω_a) and corresponding mode shapes. As shown in Fig. C.3, to implement this method, one needs to iteratively compute the physically meaningful correction coefficients until they converge to constant values. The calculation is to solve a set of linear equations simultaneously, each of which is formulated based on two modes related to the finite element and experimental models. Assume that the stiffness matrix $\mathbf{K}^*$ and mass matrix $\mathbf{M}^*$ of the experimental model are modifications of $\mathbf{K}$ and $\mathbf{M}$ of FE model by the following linear relationships

$$\mathbf{K}^* = \mathbf{K} + \sum_{n=1}^{N_e} \alpha_n \mathbf{K}_n \tag{C.10}$$

and

$$\mathbf{M}^* = \mathbf{M} + \sum_{n=1}^{N_e} \beta_n \mathbf{M}_n \tag{C.11}$$

in which $\mathbf{K}_n/\mathbf{M}_n$ is the stiffness/mass matrix corresponding to the nth element; α_n and β_n are the desired correction coefficients of the CMCM method (Hu et al., 2007).

C.3 Model updating procedures

For this tube piezoelectric transducer, the measured data are totally from the electrical impedance functions, which are modal frequencies of short-circuit model, those of open-circuit model, and impedance amplitude values at low frequency region. Since mode shapes are very difficult to obtain experimentally and they don't change significantly during the updating, the measured ones will be replaced by those of updated FE model in each iterative step. With above data, one can update the three groups of parameters, i.e., elastic, dielectric and piezoelectric ones. The elastic (stiffness) parameters are only determined by the resonant frequencies, which are the modal frequencies under short-circuit condition; dielectric parameter

(permittivity with constant stress) can be calculated by free capacitance of the transducer; and all parameters can affect the anti-resonant frequencies, which are the modal frequencies under open-circuit condition. After piezoelectric properties are all updated, the polyurethane layer will be added to the model. The Young's modulus E and Poisson's ratio ξ of this material can be updated in a similar way of updating elastic properties of piezoelectric material. The detailed procedures to implement this method are as follows (Su, 2016):

stage 1 *According to the measured resonant frequencies ω_r (corresponding to local minimum impedance amplitude) of the impedance function, one can update the stiffness parameters (c_{11} and c_{12}) based on a short-circuit FE model.*

For this linear material, assuming that each element of the model has the same properties determined by the stiffness coefficients c_{11}^E, c_{12}^E, c_{13}^E, c_{33}^E and c_{44}^E, the global displacement stiffness matrix can be written as

$$\mathbf{K}_{UU} = c_{11}^E \, \mathbf{K}_{c_{11}^E} + c_{12}^E \, \mathbf{K}_{c_{12}^E} + c_{13}^E \, \mathbf{K}_{c_{13}^E} + c_{33}^E \, \mathbf{K}_{c_{33}^E} + c_{44}^E \, \mathbf{K}_{c_{44}^E} \tag{C.12}$$

where $\mathbf{K}_{c_{ij}^E}$ is the change of $\mathbf{K}_{UU}$ due to the unit change of c_{ij}^E, which is called unit "submatrix" of c_{ij}^E. Combining Eqs. A.6 and C.1, the physical simplification yields:

$$c_{44}^E = (c_{11}^E - c_{12}^E)/2, \quad c_{33}^E = c_{11}^E, \quad c_{13}^E = c_{12}^E \tag{C.13}$$

Therefore, Eq. C.12 can be rewritten as

$$\mathbf{K}_{UU} = c_{11}^E \widehat{\mathbf{K}}_{c_{11}^E} + c_{12}^E \widehat{\mathbf{K}}_{c_{12}^E} \tag{C.14}$$

where

$$\widehat{\mathbf{K}}_{c_{11}^E} = \mathbf{K}_{c_{11}^E} + \mathbf{K}_{c_{33}^E} + \frac{1}{2}\mathbf{K}_{c_{44}^E} \tag{C.15}$$

and

$$\widehat{\mathbf{K}}_{c_{12}^E} = \mathbf{K}_{c_{12}^E} + \mathbf{K}_{c_{13}^E} - \frac{1}{2}\mathbf{K}_{c_{44}^E} \tag{C.16}$$

According to Eqs. C.10 and C.14, the updated displacement stiffness matrix $\mathbf{K}_{UU}^{*}$ can be written as

$$\mathbf{K}_{UU}^{*} = (1+\alpha_1)c_{11}^{E}\widehat{\mathbf{K}}_{c_{11}^{E}} + (1+\alpha_2)c_{12}^{E}\widehat{\mathbf{K}}_{c_{12}^{E}} = \mathbf{K}_{UU} + \sum_{i=1}^{2}\alpha_i\widehat{\mathbf{K}}_i \tag{C.17}$$

where α_1 and α_2 are the correction coefficients of c_{11}^{E} and c_{12}^{E} respectively, which can be obtained by applying the extended CMCM method.

stage 2 *According to the measured impedance value Z_0 at the low frequency region f_0, one can update the permittivity with constant stress ε_{33}^{T} in the poling direction.*

A tube piezoelectric transducer can be treated as a capacitor when it is excited at a low frequency f_0. Therefore, the impedance amplitude Z_0 can be calculated by

$$Z_0 = \frac{1}{2\pi f_0 C_f} \tag{C.18}$$

where $C_f = 2\pi\varepsilon_{33}^{T}\ell/\ln(D_o/D_i)$ is the free capacitance of the tube transducer; D_i, D_o, and ℓ represent the inner diameter, the outer diameter, and the axial length of the transducer, respectively. Therefore, ε_{33}^{T} can be updated by

$$\varepsilon_{33}^{T\,*} = \frac{\ln(D_o/D_i)}{4\pi^2\ell f_0 Z_0} \tag{C.19}$$

stage 3 *According to the measured anti-resonant frequencies ω_a (corresponding to local maximum impedance amplitude) of the impedance function, one can update the piezoelectric parameters (e_{31}) based on a open-circuit FE model.*

The linear operations on the piezoelectric coupling stiffness matrix $\mathbf{K}_{U\Phi}$ can be written as

$$\mathbf{K}_{U\Phi} = \mathbf{K}_{\Phi U}^{t} = e_{31}\mathbf{K}_{e_{31}} + e_{33}\mathbf{K}_{e_{33}} + e_{15}\mathbf{K}_{e_{15}} \tag{C.20}$$

where $\mathbf{K}_{e_{31}}$, $\mathbf{K}_{e_{33}}$ and $\mathbf{K}_{e_{15}}$ are the unit submatrices of e_{31}, e_{33} and e_{15}, respectively. According to Eqs. A.6, A.7 and C.2, one can obtain

$$e_{15} = 0, \qquad e_{33} = \frac{2c_{12}^{E}}{c_{11}^{E} + c_{12}^{E}}\, e_{31} \tag{C.21}$$

Therefore, Eq. C.20 becomes

$$\mathbf{K}_{U\Phi} = e_{31}\widehat{\mathbf{K}}_{e_{31}} \tag{C.22}$$

where

$$\widehat{\mathbf{K}}_{e_{31}} = \mathbf{K}_{e_{31}} + \left(\frac{2c_{12}^{E}}{c_{11}^{E} + c_{12}^{E}}\right)\mathbf{K}_{e_{33}} \tag{C.23}$$

Similarly, one can obtain the linear operations on the dielectric stiffness matrix $\mathbf{K}_{\Phi\Phi}$ as

$$\mathbf{K}_{\Phi\Phi} = \varepsilon_{11}^{S}\mathbf{K}_{\varepsilon_{11}^{S}} + \varepsilon_{33}^{S}\mathbf{K}_{\varepsilon_{33}^{S}} \tag{C.24}$$

where $\mathbf{K}_{\varepsilon_{11}^{S}}$ and $\mathbf{K}_{\varepsilon_{33}^{S}}$ are the unit submatrices of ε_{11}^{S} and ε_{33}^{S}, respectively. Combining Eqs. A.9 and C.2, one can have $\varepsilon_{11}^{S} = 0$. Thus, Eq. C.24 becomes

$$\mathbf{K}_{\Phi\Phi} = \varepsilon_{33}^{S}\,\mathbf{K}_{\varepsilon_{33}^{S}} \tag{C.25}$$

Substituting Eqs. C.22 and C.25 into Eq. C.8, one obtains

$$\tilde{\mathbf{K}}_{UU} = \mathbf{K}_{UU} + \mathbf{K}_{3} \tag{C.26}$$

where

$$\mathbf{K}_{3} = -a\widehat{\mathbf{K}}_{e_{31}}(\mathbf{K}_{\varepsilon_{33}^{S}})^{-1}\widehat{\mathbf{K}}_{e_{31}}^{t} \tag{C.27}$$

in which

$$a = \frac{(e_{31})^2}{\varepsilon_{33}^{S}} \tag{C.28}$$

Since $\mathbf{K}_{UU}^{*}$ has been updated in stage 1, the updated condensed eletro-elastic stiffness matrix $\tilde{\mathbf{K}}_{UU}^{*}$ can be formulated as

$$\tilde{\mathbf{K}}_{UU}^{*} = \mathbf{K}_{UU}^{*} + (1+\alpha_3)\mathbf{K}_{3} \tag{C.29}$$

where α_3 is the correction coefficient of a, which can be calculated by applying the extended CMCM method. Therefore,

$$a^{*} = (1+\alpha_3)a \tag{C.30}$$

According to Eqs. A.6 - A.8, one can derive the permittivity with constant strain ε_{33}^{S} as

$$\varepsilon_{33}^{S} = \varepsilon_{33}^{T} - \frac{2(e_{31})^2}{c_{11}^{E} + c_{12}^{E}} \tag{C.31}$$

Combining Eqs. C.28 and C.31, one can obtain

$$\varepsilon_{33}^{S\,*} = \frac{(c_{11}^{E\,*} + c_{12}^{E\,*})\varepsilon_{33}^{T\,*}}{c_{11}^{E\,*} + c_{12}^{E\,*} + 2a^*} \tag{C.32}$$

and

$$e_{31}^{*} = -\sqrt{a^* \, \varepsilon_{33}^{S\,*}} \tag{C.33}$$

stage 4 *According to the measured resonant frequencies $\omega_{r,poly}$ (corresponding to local minimum impedance amplitude) of impedance function for the transducer with polyurethane layer, one can update the elastic parameters (E and ξ) based on a short-circuit FE model.*

The linear operations on the global total stiffness matrix K_{poly} can be expressed as

$$K_{poly} = EK_E + \xi K_\xi \tag{C.34}$$

and the updated global total stiffness can be formulated as

$$K_{poly}^{*} = (1+\alpha_4)EK_E + (1+\alpha_5)\xi K_\xi = K_{poly} + \sum_{i=4}^{5} \alpha_i K_i \tag{C.35}$$

where α_4 and α_5 are the correction coefficient of E and ξ, respectively, which can be computed by applying CMCM method.

C.4 Results of updating a tube transducer

The Abaqus FE models in this example use the 3D solid piezoelectric element C3D20E. The material properties from manufacturer are Young's modulus $Y_{11} = 86$ GPa, Poisson's ratio $\nu_{12} = 0.2126$, piezoelectric coupling coefficient $d_{31} = -140$ pC/N and permittivity with constant stress $\varepsilon_{33}^{T} = 1400\ \varepsilon_0$, where

$\varepsilon_0 = 8.854 \times 10^{-12}$ F/m is the vacuum permittivity. The calculated e-form parameters are stiffness $c_{11} = 97.154$ GPa, $c_{12} = 26.233$ GPa and $c_{44} = 32.461$ GPa, piezoelectric coupling $e_{31} = -17.2740$ C/m^2 and $e_{33} = -7.3449$ C/m^2, and permittivity with constant strain $\varepsilon_{33}^S = 853.7258\ \varepsilon_0$.

With the two modal frequencies of the target short-circuit model: 43.26 kHz and 131.7 kHz, and those of the target open-circuit model: 46.18 kHz and 151.7 kHz, one applies the extended CMCM method to update the material properties of the piezoelectric tube transducer model. To implement this updating method, one still needs to obtain those submatrices in addition to the measured modal frequencies. Take $\mathbf{K}_{c_{11}^E}$, unit submatrix of c_{11}^E, as an example to show one numerical method for the calculation:

$$\mathbf{K}_{c_{11}^E} = \frac{\mathbf{K}_{UU}^{(n)} - \mathbf{K}_{UU}^{(m)}}{(n-m)c_{11}^E} \tag{C.36}$$

where $\mathbf{K}_{UU}^{(n)}$ and $\mathbf{K}_{UU}^{(m)}$ are the displacement stiffness matrices obtained from FE model with mc_{11}^E and nc_{11}^E, respectively. Considering the physical meaningfulness of FE model, the multiples' coefficients should be set close to 1, for example, $m = 0.5$ and $n = 1$. One can follow a similar way to calculate the submatrices of other properties, such as dielectric property (ε_{33}^S) and piezoelectric coupling properties (e_{31} and e_{33}).

First, one can update the elastic parameters (c_{11} and c_{12}) with the two measured resonant frequencies: 43.26 kHz and 131.7 kHz, and two submatrices: $\widehat{\mathbf{K}}_{c_{11}^E}$ and $\widehat{\mathbf{K}}_{c_{12}^E}$. The correction coefficients of c_{11}^E and c_{12}^E, α_1 and α_2 respectively, can be calculated by the extended CMCM method.

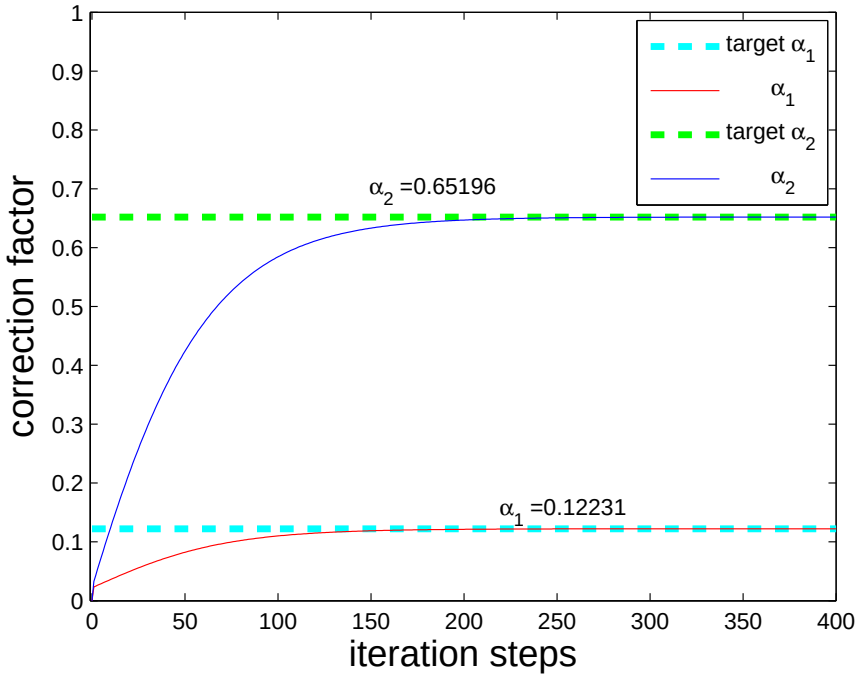

Figure C.4. Iteration results of α_1 and α_2

Shown in Fig. C.4 is the iteration sequences of α_1 and α_2, which converge to 0.1223 and 0.6520, respectively. And, the modal results of updated FE short-circuit model agree very well with the experimental data. The updated $c_{11}^{E\,*}$ and $c_{12}^{E\,*}$ can be calculated as

$$c_{11}^{E\,*} = (1+\alpha_1)c_{11}^{E} = 109.04 \text{ GPa}$$

and

$$c_{12}^{E\,*} = (1+\alpha_2)c_{12}^{E} = 43.336 \text{ GPa}$$

$f_0\ (kHz)$	2	5	7	10	12	15	17	20	22	25
$Z_0\ (\Omega)$	12860	5442	3902	2728	2267	1802	1580	1327	1195	1031

Table C.1. The measured impedance values and corresponding frequencies from the impedance function

According to Eq. C.19, together with the measured impedance values at corresponding frequencies from the impedance function in Table. C.1, one can calculate

the average permittivity at constant stress

$$\overline{\varepsilon}_{33}^{T\,*} = \frac{\overline{\ln(D_o/D_i)}}{4\pi^2 \ell Z_L f_L} = 1376.4\ \varepsilon_0$$

After updating c_{11}^*, c_{12}^* and $\varepsilon_{33}^{T\,*}$, the remaining is to update the piezoelectric parameter e_{31}. With the original piezoelectric constant $d_{31} = -140 \times 10^{-12}$ C/N and updated ones above, one can compute the e-form parameters by Eqs. A.6 and A.7

$$\begin{aligned} e_{31} &= (c_{11}^{E\,*} + c_{12}^{E\,*}) d_{31} = -21.3326 \text{ N/V·m} \\ e_{33} &= 2c_{12}^{E\,*} d_{31} = -12.1341 \text{ N/V·m} \\ \varepsilon_{33}^{S} &= \varepsilon_{33}^{T\,*} - 2d_{31}^2 (c_{11}^{E\,*} + c_{12}^{E\,*}) = 701.8007\ \varepsilon_0 \end{aligned}$$

and the original linear variable for $\mathbf{K_3}$

$$a = \frac{(e_{31})^2}{\varepsilon_{33}^S} = 0.6484/\varepsilon_0$$

The submatrices $\mathbf{K}_{e_{31}}$ ($\mathbf{K}_{e_{33}}$) and $\mathbf{K}_{\varepsilon_{33}^S}$ can be obtained in a similar way with Eq. C.36 as

$$\mathbf{K}_{e_{31}} = \frac{\mathbf{K}_{U\Phi}^{(2)} - \mathbf{K}_{U\Phi}^{(1)}}{e_{31}} \tag{C.37}$$

and

$$\mathbf{K}_{\varepsilon_{33}^S} = \frac{\mathbf{K}_{\Phi\Phi}^{(2)} - \mathbf{K}_{\Phi\Phi}^{(1)}}{\varepsilon_{33}^S} \tag{C.38}$$

Following Eq. C.23, one can calculate the submatrix $\widehat{\mathbf{K}}_{e_{31}}$.

With the two anti-resonant frequencies: 46.18 and 151.7 kHz, and two submatrices: $\widehat{\mathbf{K}}_{e_{31}}$ and $\mathbf{K}_{\varepsilon_{33}^S}$, one can apply the extended CMCM method to update the correction coefficient α_3.

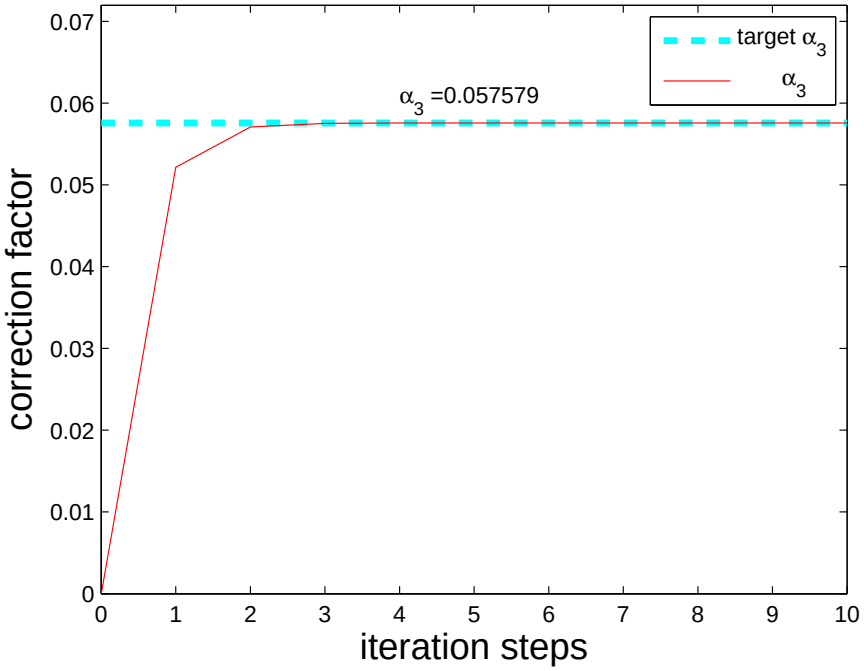

Figure C.5. Iteration results of α_3

Shown in Fig. C.5 is the iteration sequences of α_3. Within 4 steps, the correction coefficient quickly converges to 0.0576. The updated parameter a^* is

$$a^* = (1+\alpha_3)a = 0.6858/\varepsilon_0$$

According to Eqs. C.32 and C.33, one can calculate the updated $\varepsilon_{33}^{S\,*}$ and e_{31}^*

$$\begin{aligned} \varepsilon_{33}^{S\,*} &= \frac{(c_{11}^{E\,*}+c_{12}^{E\,*})\varepsilon_{33}^{T\,*}}{c_{11}^{E\,*}+c_{12}^{E\,*}+2a^*} = 682.5254\ \varepsilon_0 \\ e_{31}^* &= -\sqrt{a^*\,\varepsilon_{33}^{S\,*}} = -21.6348\ \text{N/V·m} \end{aligned}$$

Therefore, the updated parameters in 'manufacturer' form, which are originally from the manufacturer specification sheet, can be calculated

$$\begin{aligned} d_{31}^* &= \frac{e_{31}^*}{c_{11}^{E\,*}+c_{12}^{E\,*}} = -141.98\ \text{pC/N} \\ \nu_{12}^* &= \frac{c_{12}^{E\,*}}{c_{11}^{E\,*}+c_{12}^{E\,*}} = 0.2844 \\ Y_{11}^{E*} &= (c_{11}^{E\,*}+c_{12}^{E\,*})(1+\nu_{12}^*)(1-2\nu_{12}^*) = 84.390\ \text{GPa} \end{aligned}$$

Fig. C.6 shows the impedance function of updated FE model and that of experimental data have a very good agreement except some negligible discrepancy.

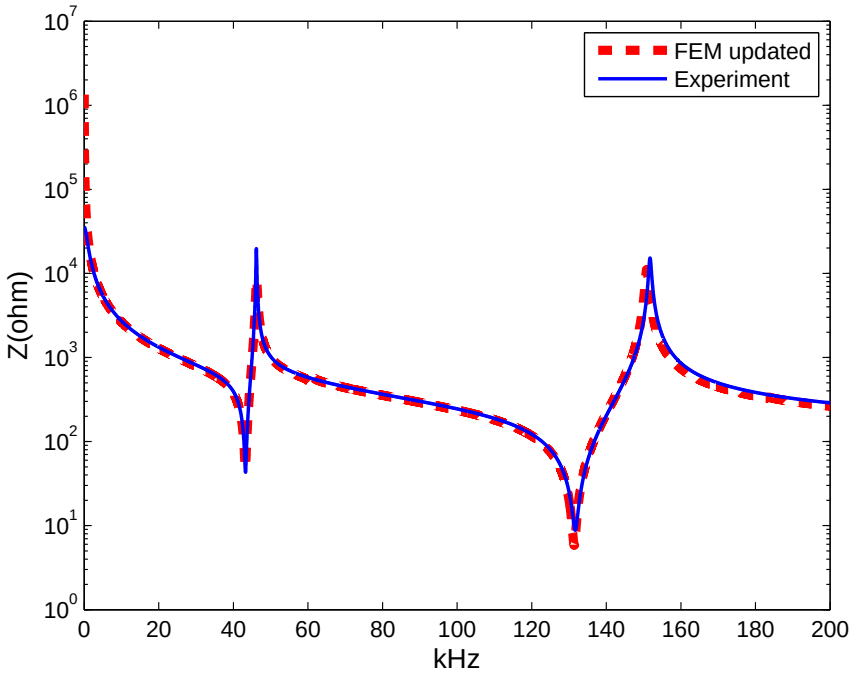

Figure C.6. Impedance comparison of piezoelectric transducer in air: updated FE model v.s. experiment (without the polyurethane layer)

Before placed into water, the transducer is coated by a 0.5mm-thick polyurethane layer and the model is shown in Fig. C.7. According to the general property of polyurethane material, the equivalent linear properties are originally set to be Young's modulus $E_{poly} = 1$ GPa and Poisson's ratio $\xi_{poly} = 0.3$. By applying the extended CMCM method in a similar way of updating elastic properties of piezoelectric material, the coefficients can be updated based on the measured resonant frequencies 41.9 kHz and 126.1 kHz. Shown in Fig. C.8, the correction factor α_4 and α_5 converge to 0.4076 and 0.0252 respectively after 3 iteration steps. The Young's modulus and Poisson's ratio are updated to 1.4706 GPa and 0.3076, respectively.

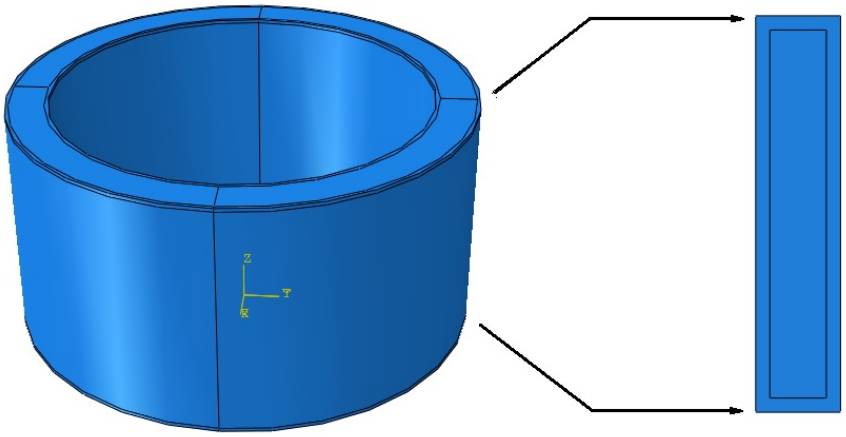

Figure C.7. Finite Element model of the piezoelectric transducer with the polyurethane layer: left panel for 3D model, right panel for a cross section

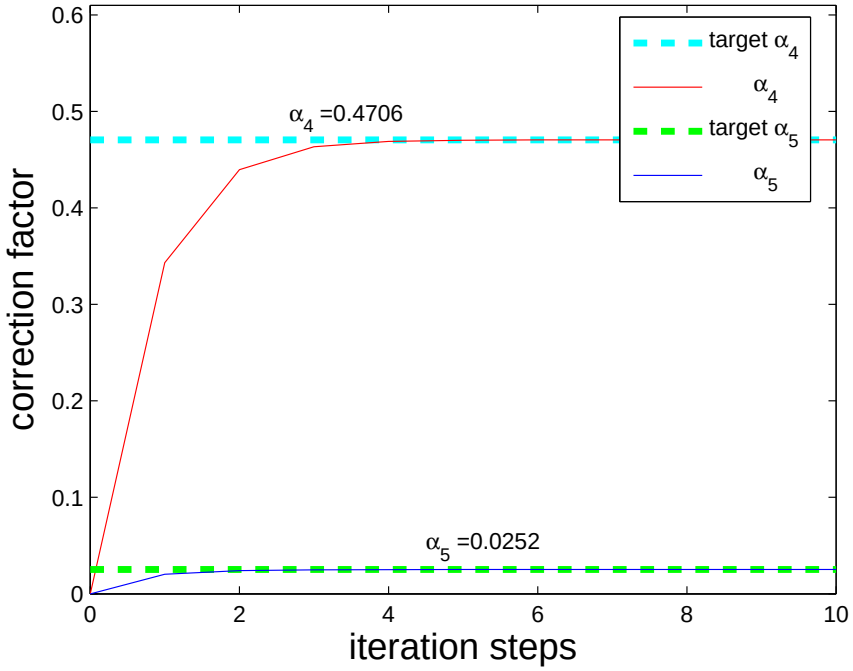

Figure C.8. Iteration results of the correction coefficients for Young's modulus and Poisson's ratio of 'linear' polyurethane material

Finally, all the properties have been updated. Table C.2 shows the comparison of material property coefficients between the original values and updated ones. The relative errors provided in last column of Table C.2 are calculated by the formula $(updated\ value\ -\ original\ value)/(updated\ value) \times\ 100\%$. The errors indicate that the manufacturer gives relatively accurate property coefficients for this transducer except the Poison's ratio, the tolerance of which is up to 25.25%. To have better impedance function, the model damping are corrected by traditional methods in this study. Since it is beyond the scope of current study, only the results are shown in Table C.2 and not discussed here. Based on all updated parameters, Fig. C.9 shows the impedance function comparison between updated FE model with polyurethane layer and experiment results. On the whole, they match each other very well. The small discrepancy might result from the linear assumption and the inaccurate damping model of polyurethane material. But, the FE model has been updated well enough for current research of characteristic functions of underwater transducers.

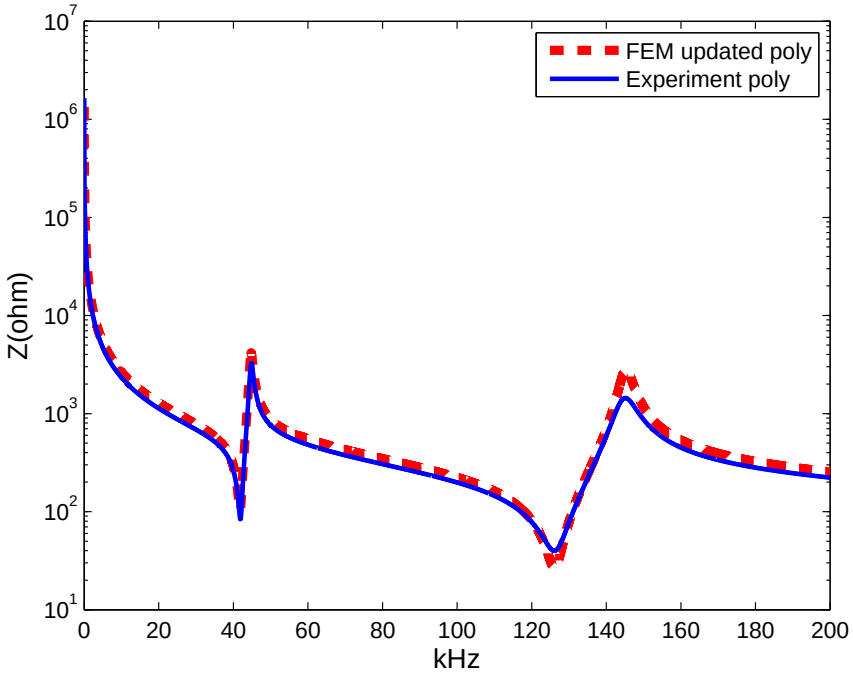

Figure C.9. Impedance function comparison of the transducer in air: updated FE model v.s. experiment(with the polyurethane layer)

material parameters			unit	original	updated	relative error
PZT e-form	stiffness	c_{11}	GPa	97.154	109.04	10.90%
	stiffness	c_{12}	GPa	26.233	43.336	39.46%
	coupling	e_{31}	C/m^2	−17.2740	−21.6348	20.16%
	permittivity	$\varepsilon_{33}^S/\varepsilon_0$	—	853.7258	682.5254	−25.08%
PZT manufacturer form	Young's modulus	Y_{11}	GPa	86	84.390	−1.91%
	Poison's ratio	ν_{12}	—	0.2126	0.2844	25.25%
	coupling	d_{31}	pm/V	−140	−141.98	1.40%
	permittivity	$\varepsilon_{33}^T/\varepsilon_0$	—	1400	1376.4	−1.71%
PZT damping	mass term	α	—	700	2446.4	—
	stiffness term	β	$\times 10^{-9}$	1.3	3.6782	—
polyurethane elastic	Young's modulus	E_{poly}	GPa	1	1.4706	—
	Poison's ratio	ν_{poly}	—	0.3	0.3076	—
polyurethane damping	mass term	α_{poly}	—	—	18320	—
	stiffness term	β_{poly}	$\times 10^{-6}$	—	2.2427	—

Table C.2. The comparison of material properties between original and updated models

LIST OF REFERENCES

Abaqus Analysis, M. (2014). Manual: Abaqus Analysis User's Guide. Dassault Systmes.

Abaqus Keywords, M. (2014). Manual: Abaqus Keywords Reference Guide. Dassault Systmes.

Abaqus Release Notes, M. (2014). Manual: Abaqus Release Notes. Dassault Systmes.

Arnold, F. J., Goncalves, M. S., Roger, L. L. B., and Muhlen, S. S. (2014). Electrical impedance of piezoelectric ceramics under acoustic loads. ECTI Transactions on Electrical Engineering, Electronics, and Communications, 12(2):48–54.

Arnold, F. J., Ximenes, R. L., Arthura, R., and Muhlen, S. S. (2015). A driver for piezoelectric transducers with control of resonance. Physics Procedia, 63:48–54.

Cao, Q., Gao, B., Li, H., and Hu, S.-L. J. (2017). A new system identification method operated in the pole domain. In International Conference on Experimental Vibration Analysis for Civil Engineering Structures (EVACES 2017), San Diego, CA.

Clough, R. W. and Penzien, J. (2003). Dynamics of Structures. Computers & Structures, Inc., 3rd edition.

Craig, R. R. and Kurdila, A. J. (2006). Fundamentals of Structural Dynamics. John Wiley & Sons, 2nd edition.

Friswell, M. and Mottershead, J. E. (1995). Finite element model updating in structural dynamics. Springer Science & Business Media.

Hu, S.-L. J. and Gao, B. (2018). Computing transient response of dynamic systems in the frequency domain. Journal of Engineering Mechanics, 144(2).

Hu, S.-L. J., Li, H., and Wang, S. (2007). Cross-model cross-mode method for model updating. Mechanical Systems and Signal Processing, 21(4):1690–1703.

Hu, S.-L. J., Liu, F.-S., Gao, B., and Li, H.-J. (2016). Pole-residue method for numerical dynamic analysis. Journal of Engineering Mechanics, 142(8):1031–1060.

Hu, S.-L. J., Su, L., and Li, H.-J. (2017). Estimating frequency response functions by pole-residue operations. In The 7th International Operational Modal Analysis Conference (IOMAC 2017), Ingolstadt, Germany.

Hu, S.-L. J., Yang, W.-L., and Li, H.-J. (2013). Signal decomposition and reconstruction using complex exponential models. Mechanical Systems and Signal Processing, 40(2):421–438.

Hu, S.-L. J., Yang, W.-L., Liu, F.-S., and Li, H.-J. (2014). Fundamental comparison of time-domain experimental modal analysis methods based on high- and first-order matrix models. Journal of Sound and Vibration, 333(25):6869–6884.

Kinsler, L. E., Frey, A. R., Coppens, A. B., and Sanders, J. V. (2000). Fundamentals of Acoustics. John Wiley & Sons, 4th edition.

Kreyszig, E. (2011). Advanced Engineering Mathematics. John Wiley & Sons, 10th edition.

Kuntsal, E. (2003). Free-flooded ring transducers: design methods and their interaction in vertical arrays. In Oceans 2003. Celebrating the Past ... Teaming Toward the Future, San Diego, CA, USA.

McMahon, G. W. (1964). Performance of open ferroelectric ceramic cylinders in underwater transducers. The Journal of the Acoustical Society of America, 36(3).

Piranda, B., Ballandras, S., Steichen, W., and Hecart, B. (2001). A model-updating procedure to simulate piezoelectric transducers accurately. IEEE Transactions on Ultrasonics, Ferroelectrics, and Frequency Control, 48(5):1321–1331.

Piranda, B., Steichen, W., and Ballandras, S. (1998). Model updating applied to ultrasound piezoelectric transducers. In 1998 IEEE Ultrasonics Symposium. Proceedings., Sendai, Japan.

Polking, J., Boggess, A., and Arnold, D. (2006). Differential Equations with Boundary Value Problems. Pearson, 2nd edition.

Sherman, C. H. and Butler, J. L. (2007). Transducers and Arrays for Underwater Sound. Springer.

STEMiNC (2018). Piezo material properties: Sm111. http://www.steminc.com/piezo/PZ_property.asp.

Su, L. (2016). Multi-phase multi-physics finite element model updating of piezoelectric transducer. PhD dissertation, University of Rhode Island.

Wikipedia Abaqus, I. (2018). Abaqus. https://en.wikipedia.org/wiki/Abaqus. Accessed on 2018-06-20.

Wikipedia Acoustic Wave, I. (2018). Acoustic wave equation. https://en.wikipedia.org/wiki/Acoustic_wave_equation. Accessed on 2018-06-21.

Wikipedia Delta Function, I. (2018). Dirac delta function. https://en.wikipedia.org/wiki/Dirac_delta_function. Accessed on 2018-06-22.

Wikipedia Electrical Impedance, I. (2018). Electrical impedance. https://en.wikipedia.org/wiki/Electrical_impedance. Accessed on 2018-06-22.

Wikipedia Radiation Pattern, I. (2018). Radiation pattern. https://en.wikipedia.org/wiki/Radiation_pattern. Accessed on 2018-06-22.

Wilson, O. B. (1988). Introduction to Theory and Design of Sonar Transducers. Peninsula Publishing.